공학박사학위논문

Robust Control and Fully-Actuated Flight Mechanism for Multirotor-Based Versatile Aerial Robotics Platform

멀티로터 기반 다목적 비행 로봇 플랫폼을 위한
강건 제어 및 완전구동 비행 매커니즘

2020년 02월

서울대학교 대학원

기계항공공학부

이 승 제

Robust Control and Fully-Actuated Flight Mechanism for Multirotor-Based Versatile Aerial Robotics Platform

A Dissertation

by

SEUNG JAE LEE

Presented to the Faculty of the Graduate School of

Seoul National University

in Partial Fulfillment

of the Requirements

for the Degree of

DOCTOR OF PHILOSOPHY

Department of Mechanical and Aerospace Engineering

Seoul National University

Supervisor : Professor H. Jin Kim

FEBUARY 2020

Always reminding myself that every challenge requires the support and guidance of my
most loved ones, I dedicate this dissertation to my beloved

Dad & Mom,
my Sister and her Family,
and
my Wife, her Family, and our Children.

Abstract

Robust Control and Fully-Actuated Flight Mechanism for Multirotor-Based Versatile Aerial Robotic Platform

Seung Jae Lee

Department of Mechanical and Aerospace Engineering

The Graduate School

Seoul National University

Recently, multi-rotor unmanned aerial vehicles (UAVs) are used for a variety of missions beyond its basic flight, including aerial manipulation, aerial payload transportation, and aerial sensor platform. Following this trend, the multirotor UAV is recognized as a versatile aerial robotics platform that can freely mount and fly the necessary mission equipment and sensors to perform missions.

However, the current multi-rotor platform has a relatively poor ability to maintain nominal flight performance against external disturbances such as wind or gust compared to other robotics platforms. Also, the multirotor suffers from maintaining a stable payload attitude, due to the fact that the attitude of the fuselage should continuously be changed for translational motion control. Particularly, unstabilized fuselage attitude can be a drawback for multirotor's mission performance in such cases as like visual odometry-based flight, since the fuselage-attached sensor should also be tilted during the flight and therefore causes poor sensor information acquisition.

To overcome the above two problems, in this dissertation, we introduce a robust multirotor control method and a novel full-actuation mechanism which widens the usability of the multirotor. The goal of the proposed control method is to bring robustness to the translational motion control against various weather conditions. And the goal of the full actuation mechanism is to allow the multi-rotor to take arbitrary payload/fuselage attitude independently of the translational motion.

For robust multirotor control, we first introduce a translational force generation technique for accurate translational motion control and then discuss the design method of disturbance observer (DOB)-based robust control algorithm. The stability of the proposed feedback controller is validated by the μ-stability analysis technique, and the results are compared to the small-gain theorem (SGT)-based stability analysis to validate the rigorousness of the analysis. Through the experiments, we validate the translational acceleration control performance of the developed controller and confirm the robustness against external disturbance forces.

For a fully-actuated multirotor platform, we propose a new mechanism called a T^3-Multirotor that can overcome the excessive weight increase and poor energy efficiency of the existing fully-actuated multirotor. The structure of the new platform is designed to be as close as possible to the existing multi-rotor and includes only two servo motors for full actuation. The dynamic characteristics of the new platform are analyzed and a six-degree-of-freedom (DOF) flight controller is designed based on the derived equations of motion. The full actuation of the proposed platform is then validated through various experiments.

As a derivative study, this paper also introduces an emergency flight technique to prepare for a single motor failure scenario of a multi-rotor using the redundancy of the T^3-Multirotor platform. The detailed introduction and implementation method of the emergency flight strategy with the analysis of the dynamic characteristics during the emergency flight is introduced, and the experimental results are provided to verify the validity of the proposed technique.

Keywords: Multi-rotor, Robust control, μ-analysis, Disturbance observer, Aerial robotics, Fully-actuated multirotor

Student Number: 2016-30189

Table of Contents

List of Tables

List of Figures

1

Introduction

1.1 Motivation

Recently, the multi-rotor unmanned aerial vehicle (hereinafter called 'multirotor') is recognized as an aerial robotics platform beyond simply as an aircraft, and is widely applied in various research and industrial fields. The popularity of multi-rotor as an aviation robotic platform stems from the fact that it has simple structure and operation principle to make the platform easy to control and attach additional equipment or transform shapes to suit the mission.

However, the multirotor has the following disadvantages. First, the platform is susceptible to wind disturbances during the flight which can easily fail to maintain nominal performance in severe gust conditions. Second, the multirotor needs to change the attitude constantly during the translational motion control due to the inherent underactuation characteristics, therefore reduces their applicability in various scenarios. A representative example of problems caused by continuous attitude change includes multirotor-based aerial photography, where controlling the position and orientation of the firmly-attached camera

cannot be performed simultaneously [2].

Therefore, to provide a higher performance of the multirotor-based robot platform, the above two problems must be overcome. For such an objective, firstly we need a robust control method against translational force disturbance that causes translational motion disturbance. And secondly, we need a new type of multirotor that has additional controllable degrees of freedom (DOFs) to perform translational and rotational motion control independently and simultaneously.

First, for robust translational motion control, a robust translational acceleration control method should be established. In terms of a translational motion controller, the fuselage can be treated as a mass point that only needs to handle the position vector and its derivatives. In this case, the attitude and thrust of the multirotor can be treated only as a means for controlling the translational motion. Here, the control of the attitude and the thrust has equal meaning as controlling the three-dimensional force vector in terms of translational motion. Also, the disturbance in the translational motion can be expressed as a three-dimensional force vector. From these facts, it is necessary to establish a robust three-dimensional acceleration controller that can apply the target acceleration command as the control input and at the same time establish a robust controller against disturbance forces, for better translational motion control performance.

Second, for a fully-actuated flight mechanism, we need a new type of system that ensures additional degrees of freedom in flight while maintaining the ease of operation resulting from the structural simplicity of conventional multirotors. Also, to improve energy efficiency from existing fully-actuated multirotor flight mechanisms, the new mechanism needs to avoid a certain design that causes unnecessary internal force cancellation among thrusters and an excessive increase in the number of servomotors/actuators.

1.2 Literature survey

1.2.1 Robust translational motion control

First, for accurate force control, the target force command must be converted to the appropriate target attitude and thrust value, because the multi-rotor generates the three-dimensional translational forces by the combination of the current attitude and the total propeller thrust [3]. Once the target attitude and the total thrust command are determined, each value passes through attitude and thrust dynamics that are quite different from each other : the process of achieving actual attitude involves feedback attitude control [4], torque generation by the combination of motor's thrust, followed by the rotation of the fuselage that has larger moment of inertia than the propellers. Due to such difference, simple kinematic conversion of the force signal without consideration of the actual attitude and thrust dynamics can cause unsynchronized realization of the attitude and the total thrust, which degrades acceleration tracking performance which is controlled by the combination of attitude and thrust.

To the best of our knowledge, however, many studies have not investigated this issue. In [3] and [5], the target thrust signal was computed without considering attitudinal dynamics while treating Z-directional translational dynamics as a separate channel to other horizontal dynamics. All three axes of translational dynamics have been simultaneously considered in [6] during the conversion process, but they also did not reflect the different characteristics of attitude and thrust dynamics. Those differences become noticeable in multi-rotors that have large moment of inertia, due to significant time delay between input and output attitude.

Second, for a satisfactory level of translational disturbance rejection, we need a controller that estimates and offsets the effect of the disturbance [7,8]. As a way to achieve this goal, we can consider constructing the Disturbance Observer (DOB)-based robust control algorithm [9]. However, although several studies applied the Disturbance Observer (DOB) robust

control technique to their controllers [10–20], most of them [10–17] aimed to maintain the nominal attitude control performance against *torque* disturbance. Therefore, this approach has a limitation in overcoming translational movement disturbances. Only a few studies exist on applying DOB to overcome the translational force disturbances including [18], [19], and [20]. In [18], however, only the estimation method of the disturbance is introduced and no specific control method for overcoming the disturbance using the estimated disturbance is proposed. In [19], inverse kinematics rather than inverse dynamics is used in the process of generating disturbance compensation signal. This approach can cause severe degradation in disturbance estimation performance as the dynamics is not negligible. In [20], which is the preliminary research of this paper, the structure of DOB to cope with translational force disturbance is proposed. However, accurate translational acceleration control is not achieved because of the error in converting the target translational force command to the target attitude and total thrust. Also, the nominal model used in DOB is based on inaccurate desired acceleration-to-desired states conversion technique.

1.2.2   Fully-actuated multirotor platform

Several multirotor structures have been proposed to implement 6-DOF motion control of multirotor [21–35], and they can be classified into two types. The first type [21–27] is to install the thrusters in various directions and control the sum of the thrust vectors to the desired direction and magnitude. The second type [28–35] is to attach multiple single-DOF servomotors to each thruster so that the direction of each thruster can be changed within a certain range.

The first type of multirotor allows full control of the translational motion while taking any attitude. However, such mechanism tends to have low energy efficiency because all the thrust vector components other than the target direction component should be internally canceled during the collective thrust generation process. Also, due to the unique shape of the platform that is different from the existing multirotor, mounting a payload such as a sensor or a cargo could become difficult. Unlike the first type, the shape of second type

Figure 1.1: Structure of the proposed translational force system with disturbance observer for precise and robust acceleration tracking performance of a multi-rotor UAV.

is similar to the conventional multirotor thus free from the heterogeneity problem. But this type requires numerous additional servomotors, which may increase weight and power consumption.

1.3 Research objectives and contributions

1.3.1 Goal #I: Robust multirotor motion control

For robust multirotor motion control, we present a new accurate three-dimensional translational acceleration tracking control that overcomes the limitations of the previous studies. The contributions of the proposed acceleration control technique are as follows. First, we introduce a new conversion method that reflects the difference between attitude dynamics and thrust dynamics when computing the target attitude and total thrust command from the translational force command (i.e., 'Converter #2' block of Fig. 1.1). Second, we model the translational force system (i.e., the shaded part of Fig. 1.1) that includes the new command conversion method, and design a DOB-based robust controller (i.e., 'Disturbance Estimator' block of Fig. 1.1) that overcomes translational force disturbance based on our new system control model. In the DOB controller design process, we perform μ-analysis to systematically take into account the complex effects of various uncertainty. By presenting simulation and experimental results, we demonstrate the target acceleration tracking per-

Figure 1.2: Demonstration of T^3-Multirotor flight. The new platform can take a fuselage attitude independently of its translational motion. This feature allows the platform to freely change the fuselage attitude in the hovering state (top) or maintain a constant attitude during the translational motion (bottom).

formance of the proposed conversion technique and the ability to overcome the external translational force disturbance of the designed DOB controller.

1.3.2   Goal #II: A new fully actuated multirotor platform

For full actuation of the multirotor, we introduce a novel fully-actuated multirotor platform named 'Tilting Thruster Type'-multirotor (or T^3-Multirotor, the platform in Fig. 1.2). The new platform is designed to have a similar shape and form factor to conventional multirotors while achieving 6-DOF motion utilizing only two additional servomotors. With its new design, the T^3-Multirotor allows six controllable DOF flight free from heterogeneity problems and the energy efficiency issues of the existing fully-actuated multirotors.

1.3.3   Goal #II-A: T^3-Multirotor-based fail-safe flight

As an extension of Goal #II, we introduce a new fail-safe flight technique that takes advantage of the redundancy of the t3 multirotor, allowing the multirotor to fly reliably even in single-copter failure scenarios on quadcopters.

1.4   Thesis organization

The remainings of the paper are organized as follows.

In chapter II, we explain the operation principle of multirotor and derive the equations of motion for better explanation of the following chapters.

Chapter III is is organized as follows. In Section II, we discuss the mathematical model of the multi-rotor used in the controller design. Section III deals with the force control of multirotor, and Section IV describes how DOB is applied to the force control. Section V provides the stability analysis to determine the range of DOB parameters that guarantee the stability of the designed system even in the presence of various uncertain elements. In Section VI, we demonstrate the empirical validity through simulations and actual experiments.

Chapter IV is is organized as follows. In section II, the brief introductions of the mechanical structure and operation principle of T^3-Multirotor are provided. Section III describes equations of motion for analyzing the dynamic system characteristics of the platform. In section IV, the controller design for 6-DOF motion control of T^3-Multirotor is discussed based on the results of section III. In section V and VI, the 6-DOF flight control performance of the proposed controller is validated through simulations and experiments. In section VII, we demonstrate the potentials of the T^3-Multirotor in various possible future applications by showing examples of flight tasks that cannot be performed with conventional multirotors.

Chapter V is organized as follows. In section II, the mechanism and equations of motion of the T^3-Multirotor are introduced. Section III introduces a fail-safe flight strategy, followed

by an introduction to the fail-safe controller in Section IV. In section V, we present the actual experimental results with a detailed analysis for validation of the theory.

2

Multi-Rotor Unmanned Aerial Vehicle: Overview

2.1 Platform overview

In this chapter, we introduce the operation principle of the multirotor flight and derive the mathematical representation of the platform's motion.

The multirotor unmanned aerial vehicle is a platform that contains numerous fixed-pitch propeller-based thrusters generating desired forces for flight. The thrusters are mostly located and fixed on the same plane, and the propulsion directions are also aligned and fixed in the same direction. For these reasons, the dynamics of the platform become highly simple, but at the same time, a structural disadvantage arises that the platform can only generate propulsion in a direction perpendicular to the fuselage. Due to this characteristic of the multirotor, a procedure for distributing the fixed-directional propulsion force in the three-dimensional space is required to control the three-dimensional translational motion. The distribution of thrust force is possible by controlling the attitude of the multirotor, in

which the multirotor is then required to generate the torque for rotational motion control.

In order to generate the torque required for attitude control, the multirotor deliberately causes an imbalance of the thrust. Fig. 2.1 shows a typical arrangement of the thrusters in a quadrotor-type multirotor. As we see in the figure, each thruster of the quadrotor UAV is located a certain distance away from the platform's center of mass (COM) and this separation acts as a moment arm, allowing each thruster to generate rotational torque as well as translational force during propulsion. The mathematical expression of the relationship between thrust force F_i and attitude control torque $\tau_{\{r,p,y\}}$ of the quadrotor UAV is as follows,

$$
\begin{bmatrix} \tau_r \\ \tau_p \\ \tau_y \end{bmatrix} = \begin{bmatrix} 0 & l & 0 & -l \\ l & 0 & -l & 0 \\ b/k & -b/k & b/k & -b/k \end{bmatrix} \begin{bmatrix} F_1 \\ F_2 \\ F_3 \\ F_4 \end{bmatrix} \tag{2.1}
$$

where $l \in \mathbb{R}$ is the length between each thruster and COM, $b/k \in \mathbb{R}$ is the ratio between the thrust force and the reaction torque that is generated by the reaction of the propeller's rotation. By being able to control the thrust force of the individual thrusters, we can now control the overall rotational torque of the platform to change the fuselage attitude as desired. And as mentioned, through attitude control, we can adjust the net thrust force direction as desired, and control the platform's three-directional thrust vector by further controlling the magnitude of the net force.

2.2 Mathematical model of multi-rotor UAV

Next, we express the aforementioned operation principle of the multirotor through mathematical expression. In the case of the rotational motion of the multirotor, the fuselage dynamics can be expressed as follows

$$
J\dot{\boldsymbol{\Omega}} = \mathbf{T}_r - \boldsymbol{\Omega} \times J\boldsymbol{\Omega}, \tag{2.2}
$$
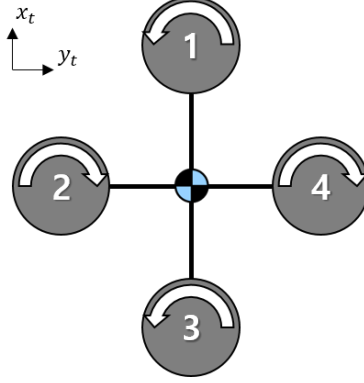
Figure 2.1: Example of thruster installation in a quadrotor platform.

where $J \in \mathbb{R}^{3 \times 3}$ is the moment of inertia (MOI) of the multi-rotor, $\mathbf{\Omega} = [p \ q \ r]^T \in \mathbb{R}^{3 \times 1}$ is an angular velocity vector defined in the body frame, and $\mathbf{T}_r = [\tau_r \ \tau_p \ \tau_y]^T \in \mathbb{R}^{3 \times 1}$ is an attitude control torque vector. The attitude control input $\mathbf{T}_r$ is generated through the thrust combination of Equation 2.1. For attitude dynamics, however, simplified dynamics of

$$J\ddot{\mathbf{q}} = \mathbf{T}_r \tag{2.3}$$

is more commonly used, taking into account the small operation range of roll and pitch angle of multi-rotor and negligible Coriolis term [3, 19, 36]. The vector $\mathbf{q} = [\phi \ \theta \ \psi]^T \in \mathbb{R}^{3 \times 1}$ is an attitude of the multi-rotor in the earth fixed frame.

In the case of the translational motion, the fuselage dynamics is given by

$$m\ddot{\mathbf{X}} = \mathbf{F} + m\mathbf{g} = R(\mathbf{q})\mathbf{T}_t + m\mathbf{g} \tag{2.4}$$

where m is the mass of the multi-rotor, $\mathbf{X} = [x \ y \ z]^T \in \mathbb{R}^{3 \times 1}$ is the position in the earth fixed frame, $\mathbf{F} = [F_x \ F_y \ F_z]^T \in \mathbb{R}^{3 \times 1}$ is the three-dimensional translational force vector generated by the multi-rotor, $R(\mathbf{q})$ is the rotation matrix from the body frame to earth fixed frame, $\mathbf{T}_t = [0 \ 0 \ -T_t]^T \in \mathbb{R}^{3 \times 1}$ is the thrust force vector in the body frame, $T_t \in \mathbb{R}$ is the magnitude of the total thrust, and $\mathbf{g} = [0 \ 0 \ g]^T \in \mathbb{R}^{3 \times 1}$ is a gravity vector. Equation 2.4 shows that the force vector $\mathbf{F}$ is generated by the combination of the fuselage pose

$\mathbf{q}$ and the thrust vector $\mathbf{T}_t$. Therefore, a total of four control inputs are required for the translational motion, and accordingly, Equation 2.1 is changed to as follows

$$\mathbf{u} = \begin{bmatrix} 0 & l & 0 & -l \\ l & 0 & -l & 0 \\ b/k & -b/k & b/k & -b/k \\ 1 & 1 & 1 & 1 \end{bmatrix} \mathbf{c}_0 = A_{quad}\mathbf{c}_0, \tag{2.5}$$

where $\mathbf{u} = [\tau_r\ \tau_p\ \tau_y\ T_t]^T \in \mathbb{R}^{4\times 1}$ is a final form of the multirotor control input for translational motion and $\mathbf{c}_0 = [F_1\ F_2\ F_3\ F_4]^T \in \mathbb{R}^{4\times 1}$ is an thruster force input vector. Since only F_i of the components of Equation 2.5 can actually be applied to the system, we need to convert $\mathbf{u}$ signals to $\mathbf{c}_0$ signals. Since A_{quad} is a full rank matrix, we can find the value of $\mathbf{c}_0$ to implement $\mathbf{u}$ simply by the following equation.

$$\mathbf{c}_0 = A_{quad}^{-1}\mathbf{u} \tag{2.6}$$

Among these control inputs, $\tau_{\{r,p,y\}}$ values are determined by a high-order feedback attitude controller, and T_t is determined by a separate high-order altitude controller.

By controlling the attitude and thrust of the platform through Equation 2.6, we can now control $\mathbf{F}$ in Equation 2.4. With this result, in the next chapter, we introduce techniques for controlling the robust translational motion of the platform.

3

Robust Translational Motion Control

This chapter is based on the following paper.

Authors	Seung Jae Lee[1]	sjlazza@snu.ac.kr
	Seung Hyun Kim[1]	kshipme@snu.ac.kr
	H. Jin Kim[1]	hjinkim@snu.ac.kr
	[1]Seoul National University	

Contribution	Problem definition	main contributor
	Literature survey	main contributor
	Method development	main contributor
	Implementation	main contributor
	Experimental validation	main contributor
	Preparation of the manuscript	main contributor

3.1 Introduction

In this chapter, we present a new accurate three-dimensional translational acceleration tracking control that overcomes the limitations of the previous studies. The contributions of the proposed acceleration control technique are as follows. First, we introduce a new conversion method that reflects the difference between attitude dynamics and thrust dynamics when computing the target attitude and total thrust command from the translational force command (i.e., 'Converter #2' block of Fig. 1.1). Second, we model the translational force system (i.e., the shaded part of Fig. 1.1) that includes the new command conversion method, and design a DOB-based robust controller (i.e., 'Disturbance Estimator' block of Fig. 1.1) that overcomes translational force disturbance based on our new model. In the DOB controller design process, we perform μ-analysis to systematically take into account the complex effects of various uncertainty. By presenting simulation and experimental 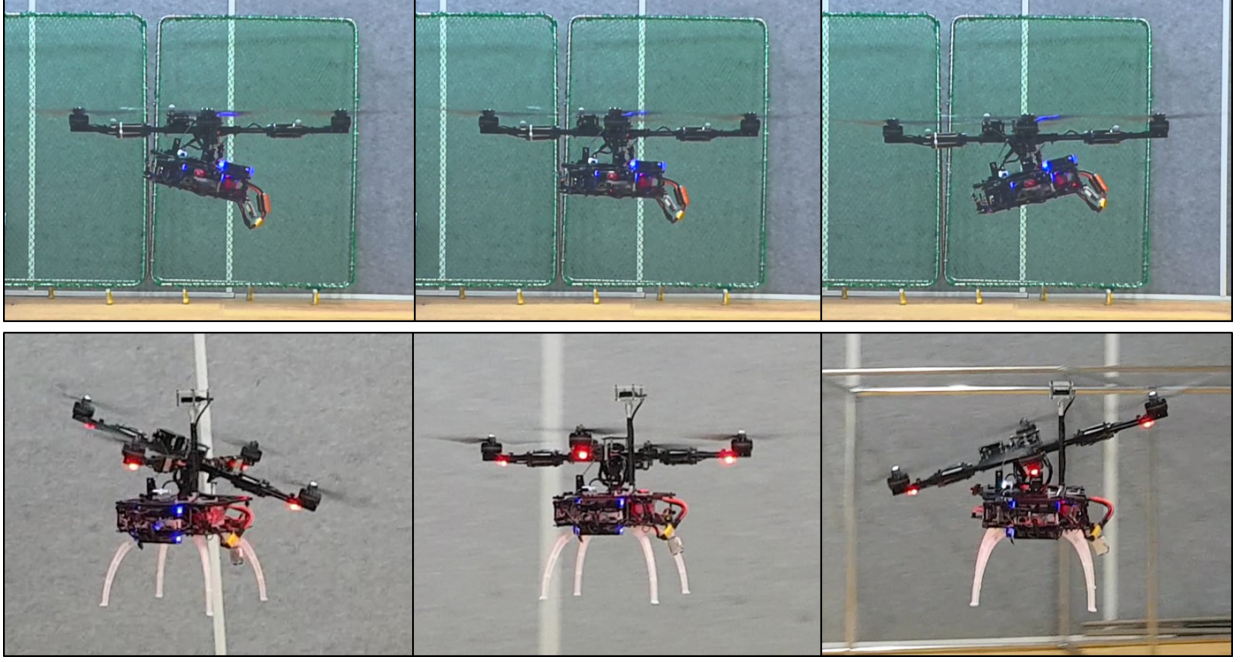results, we demonstrate the target acceleration tracking performance of the proposed conversion technique and the ability to overcome the external translational force disturbance of the designed DOB controller.

This chapter is organized as follows. Section II deals with the force control of multi-rotor, and Section III describes how DOB is applied to the force control. Section IV provides the stability analysis to determine the range of DOB parameters that guarantee the stability of the designed system even in the presence of various uncertain elements. In Section V, we demonstrate the empirical validity through simulations and actual experiments.

3.2 Translational force/acceleration control

In order to control the translational force/acceleration of the multi-rotor, we need to convert the target acceleration $\ddot{\mathbf{X}}_d$ into the target attitude $\mathbf{q}_d$ and the target thrust $T_{t,d}$. Throughout this chapter, notation $(*)_d$ denotes the desired value of the variable $*$. Also, we assume that the yaw ψ of $\mathbf{q}$ always remains zero through a well-behaved independent controller to

simplify the discussion. Now, we define $\mathbf{r} = [\theta \ \phi \ T_t]^T \in \mathbb{R}^{3\times 1}$ as a set of states that needs to be controlled for generating the desired translational acceleration of the multi-rotor.

Once we choose $\mathbf{r} = [\theta \ \phi \ T_t]^T$ as a set of state variables to control the translational force/acceleration of multi-rotor, our next task should be finding a way to convert the desired acceleration $\ddot{\mathbf{X}}_d$ to $\mathbf{r}_d$. To figure out how to convert the signal, let us first investigate the relationship between $\mathbf{r}$ and $\ddot{\mathbf{X}}$.

3.2.1 Relationship between r and $\tilde{\tilde{\mathbf{X}}}$

In Equation (2.4), we have discussed the dynamics of the translational motion of multi-rotor. Going into detail, the corresponding translational dynamics are expressed as

$$m\ddot{\mathbf{X}} = -R(\psi) \begin{bmatrix} \cos\phi\sin\theta \\ -\sin\phi \\ \cos\phi\cos\theta \end{bmatrix} T_t + m\mathbf{g}, \tag{3.1}$$

where $R(\psi) \in \mathbb{R}^{3\times 3}$ is the yaw rotation matrix. Now, let us define a vector of state variables $\tilde{\tilde{\mathbf{X}}}$ named the pseudo-acceleration vector as

$$\tilde{\tilde{\mathbf{X}}} = \begin{bmatrix} \tilde{\tilde{x}} \\ \tilde{\tilde{y}} \\ \tilde{\tilde{z}} \end{bmatrix} = R^{-1}(\psi)\left(\ddot{\mathbf{X}} - \mathbf{g}\right) = R^{-1}(\psi)(\frac{1}{m}\mathbf{F}). \tag{3.2}$$

Applying Equation (3.2) to (3.1), we obtain the following relationship between $\mathbf{r}$ and $\tilde{\tilde{\mathbf{X}}}$:

$$m\tilde{\tilde{\mathbf{X}}} = -h(\phi,\theta)T_t = -\begin{bmatrix} \cos\phi\sin\theta \\ -\sin\phi \\ \cos\phi\cos\theta \end{bmatrix} T_t. \tag{3.3}$$

15

3.2.2 Calculation of $\mathbf{r}_d$ from $\ddot{\tilde{\mathbf{X}}}_d$ considering dynamics

From Equation (3.3), we begin a discussion on how to calculate $\mathbf{r}_d$ based on $\ddot{\tilde{\mathbf{X}}}_d$. First, Equation (3.3) yields the following expression on $\mathbf{r}$:

$$
\mathbf{r} = \begin{bmatrix} \theta \\ \phi \\ T_t \end{bmatrix} = \begin{bmatrix} \arctan\left(\frac{\ddot{\tilde{x}}}{\ddot{\tilde{z}}}\right) \\ \arctan\left(-\frac{\ddot{\tilde{y}}\cos\theta}{\ddot{\tilde{z}}}\right) \\ -\frac{m\ddot{\tilde{z}}}{\cos\phi\cos\theta} \end{bmatrix}.
\tag{3.4}
$$

Equation (3.4) represents the required states $\mathbf{r}$ to generate such translational acceleration. From this, one might try to find the input to the controller to create the desired acceleration by replacing $\ddot{\tilde{\mathbf{X}}}$ and $\mathbf{r}$ with $\ddot{\tilde{\mathbf{X}}}_d$ and $\mathbf{r}_d$, respectively, as follows.

$$
\theta_d = \arctan\left(\frac{\ddot{\tilde{x}}_d}{\ddot{\tilde{z}}_d}\right)
\tag{3.5}
$$

$$
\phi_d = \arctan\left(-\frac{\ddot{\tilde{y}}_d\cos\theta_d}{\ddot{\tilde{z}}_d}\right) = \arctan\left(\frac{\ddot{\tilde{y}}_d}{\sqrt{\ddot{\tilde{x}}_d^2 + \ddot{\tilde{z}}_d^2}}\right)
\tag{3.6}
$$

$$
T_{t,d} = -\frac{m\ddot{\tilde{z}}_d}{\cos\phi_d\cos\theta_d} = -m\sqrt{\ddot{\tilde{x}}_d^2 + \ddot{\tilde{y}}_d^2 + \ddot{\tilde{z}}_d^2}
\tag{3.7}
$$

However, this method can severely degrade control performance when multi-rotor is larger than a certain size as we discuss below.

Fig. 3.1 shows the internal structure between $\mathbf{r}_d$ and $\mathbf{r}$. In this figure, we can see that ϕ_d and θ_d are realized to ϕ and θ through attitude controller, rotor dynamics, and attitude dynamics. In contrast, $T_{t,d}$ only passes through the rotor dynamics to become T_t. Here, we treat $\mathbf{u}_d = \mathbf{u}$, where $\mathbf{u} = [\mathbf{T}_r \ T_t]^T \in \mathbb{R}^{4\times1}$, since rotor dynamics are mostly negligible. Assuming that the attitude controller is properly designed, we can model the relationship
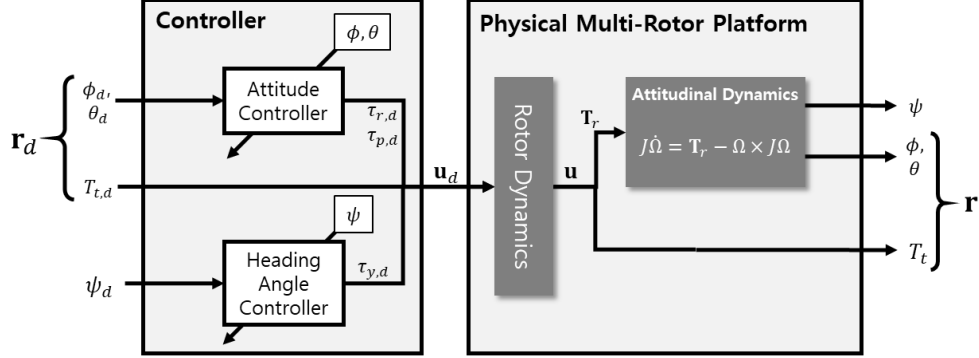
Figure 3.1: A block diagram of the relationship between $\mathbf{r}_d$ and $\mathbf{r}$, where $\mathbf{r} = [\theta, \phi, T_t]^T$, and $\mathbf{u} = [\tau_r, \tau_p, \tau_y, T_t]^T$.

between $\mathbf{r}_d$ and $\mathbf{r}$ as the following equation:

$$
\mathbf{r}(t) = \begin{bmatrix} \theta(t) \\ \phi(t) \\ T_t(t) \end{bmatrix} \approx \begin{bmatrix} \theta_d\left(t - \gamma_\theta\right) \\ \phi_d\left(t - \gamma_\phi\right) \\ T_{t,d}(t) \end{bmatrix}.
\tag{3.8}
$$

Here, $\gamma_* \in [0, \infty)$ are time-varying non-negative delay factors. Applying Equation (3.8) into (3.3), we have

$$
m\ddot{\tilde{\mathbf{X}}} = h\Big(\phi_d\big(t - \gamma_\phi\big), \theta_d\big(t - \gamma_\theta\big)\Big) T_{t,d}(t).
\tag{3.9}
$$

In Equation (3.9), the desired attitude and total thrust are realized asynchronously due to γ_ϕ and γ_θ. Applying Equation (3.7) to Equation (3.9), the result is follows.

$$
\begin{bmatrix} \ddot{\tilde{x}}(t) \\ \ddot{\tilde{y}}(t) \\ \ddot{\tilde{z}}(t) \end{bmatrix} = \begin{bmatrix} \left(\frac{\cos \phi_d(t-\gamma_\phi)}{\cos \phi_d(t) \cos \theta_d(t)} \ddot{\tilde{z}}_d(t)\right) \sin \theta_d(t - \gamma_\theta) \\ -\left(\frac{1}{\cos \phi_d(t) \cos \theta_d(t)} \ddot{\tilde{z}}_d(t)\right) \sin \phi_d(t - \gamma_\phi) \\ \left(\frac{\cos \phi_d(t-\gamma_\phi) \cos \theta_d(t-\gamma_\theta)}{\cos \phi_d(t) \cos \theta_d(t)}\right) \ddot{\tilde{z}}_d(t) \end{bmatrix}
\tag{3.10}
$$

In the $\ddot{\tilde{z}}(t)$ equation of Equation (3.10), the parenthesized part can continuously change if γ_ϕ and γ_θ are too large to be ignored. This indicates that z-directional control performance can be significantly reduced if the delay between the desired and actual attitude signals becomes large, for example in situations when the MOI of the multi-rotor increases, such as large

17

multi-rotor or multi-rotor with large cargo. When the Z-directional control performance degrades, a high-level controller (e.g., position controller) or the operator may need to constantly modify the $\tilde{\ddot{z}}_d$ value to correct the poor Z-directional control performance. As a result, this degrades the X and Y direction control performance because the values in parentheses of the $\tilde{\ddot{x}}(t)$ and $\tilde{\ddot{y}}(t)$ equations in (3.10) also constantly change. The decline in control performance due to this control scheme will be shown in Fig. 3.2.

To address this issue, we next consider two candidate solutions.

3.2.2.1 Solution candidate 1

The first candidate is to time-synchronize the attitude and total thrust output by adding an artificial time delay to $T_{t,d}$ in Equation (3.7) as

$$T_{t,d} = -\frac{m\tilde{\ddot{z}}_d(t - \gamma_v)}{\cos\phi_d(t - \gamma_\phi)\cos\theta_d(t - \gamma_\theta)}. \tag{3.11}$$

Here, γ_v is a delay element deliberately applied to $\tilde{\ddot{z}}_d$. Applying Equation (3.11) to Equation (3.9), the equation of motion is changed from Equation (3.10) to

$$\begin{bmatrix} \tilde{\ddot{x}}(t) \\ \tilde{\ddot{y}}(t) \\ \tilde{\ddot{z}}(t) \end{bmatrix} = \begin{bmatrix} \tan\theta_d(t - \gamma_\theta) \\ -\frac{\tan\phi_d(t-\gamma_\phi)}{\cos\theta_d(t-\gamma_\theta)} \\ 1 \end{bmatrix} \tilde{\ddot{z}}_d(t - \gamma_v). \tag{3.12}$$

Through Equations (3.5), (3.6) and (3.8), $\phi(t)$ and $\theta(t)$ can be described as

$$\begin{cases} \theta(t) = \arctan\left(\frac{\tilde{\ddot{x}}_d(t-\gamma_\theta)}{\tilde{\ddot{z}}_d(t-\gamma_\theta)}\right) \\ \phi(t) = \arctan\left(-\frac{\tilde{\ddot{y}}_d(t-\gamma_\phi)\cos\theta_d(t-\gamma_\phi)}{\tilde{\ddot{z}}_d(t-\gamma_\phi)}\right). \end{cases} \tag{3.13}$$

Let us assume that γ_ϕ and γ_θ have the same value of γ_h since most multi-rotors have nearly the same roll and pitch behavior due to the symmetrical mechanical structure.

Then, Equation (3.12) with Equations (3.8) and (3.13) becomes as

$$
\begin{bmatrix} \ddot{\tilde{x}}(t) \\ \ddot{\tilde{y}}(t) \\ \ddot{\tilde{z}}(t) \end{bmatrix} = \begin{bmatrix} \ddot{\tilde{x}}_d(t - \gamma_h)\left(\frac{\ddot{\tilde{z}}_d(t-\gamma_v)}{\ddot{\tilde{z}}_d(t-\gamma_h)}\right) \\ \ddot{\tilde{y}}_d(t - \gamma_h)\left(\frac{\ddot{\tilde{z}}_d(t-\gamma_v)}{\ddot{\tilde{z}}_d(t-\gamma_h)}\right) \\ \ddot{\tilde{z}}_d(t - \gamma_v) \end{bmatrix} .
\tag{3.14}
$$

Now, we can solve the problem in Equation (3.10) by setting γ_v equal to γ_h. However, this method is not easily applicable in a real-world situation because it is difficult to determine the value of γ_h that changes continuously during the flight. Therefore, the control method through Equation (3.11) cannot be a practical method.

3.2.2.2 Solution candidate 2

Alternatively, we can find a reasonable solution that is applicable in the real world by selectively delaying $\phi_d(t)$ and $\theta_d(t)$ in Equation (3.11) by γ_ϕ and γ_θ, but keeping γ_v at zero. As we can see from Equation (3.8), the values of $\phi_d(t)$ and $\theta_d(t)$ delayed by γ_ϕ and γ_θ seconds are $\phi(t)$ and $\theta(t)$. Applying this idea to Equation (3.11), we can obtain $T_{t,d}$ as

$$
T_{t,d} = -\frac{m\ddot{\tilde{z}}_d(t)}{\cos\phi(t)\cos\theta(t)},
\tag{3.15}
$$

where the values $\phi(t)$ and $\theta(t)$ can be measured from the built-in inertial measurement unit (IMU) sensor. Then, by setting γ_v to zero, we can determine the input/output relationship of the translational accelerations dynamics of the multi-rotor as

$$
\ddot{\tilde{\mathbf{X}}} = \begin{bmatrix} \ddot{\tilde{x}}_d(t - \gamma_h)\left(\frac{\ddot{\tilde{z}}_d(t)}{\ddot{\tilde{z}}_d(t-\gamma_h)}\right) \\ \ddot{\tilde{y}}_d(t - \gamma_h)\left(\frac{\ddot{\tilde{z}}_d(t)}{\ddot{\tilde{z}}_d(t-\gamma_h)}\right) \\ \ddot{\tilde{z}}_d(t) \end{bmatrix} \approx \begin{bmatrix} \ddot{\tilde{x}}_d(t - \gamma_h) \\ \ddot{\tilde{y}}_d(t - \gamma_h) \\ \ddot{\tilde{z}}_d(t) \end{bmatrix} ,
\tag{3.16}
$$

where we assume $\frac{\ddot{\tilde{z}}_d(t)}{\ddot{\tilde{z}}_d(t-\gamma_h)} \approx 1$. This assumption is valid in most cases, except in situations where the change in target vertical acceleration is abnormally large and rapid.

19

Through the control techniques of solution candidate 2 (Equations (3.5), (3.6) and (3.15)), we obtained a three-dimensional translational acceleration control method applicable to actual multi-rotor control. In order to compare the performance of multi-rotor control using Equations (3.7) and (3.15), a brief simulation is conducted as shown in Fig. 3.2.

The simulation shows the comparison of the target acceleration tracking performance of Case 1 with Equations (3.5), (3.6), (3.7) and Case 2 with Equations (3.5), (3.6), (3.15). The upper set of figures show the acceleration tracking performance of Cases 1 and 2 with arbitrary acceleration command. Here, we can see that there are no differences in performance between Cases 1 and 2 when MOI of the multi-rotor has small value of 0.1. On the other hand, when the MOI of the multi-rotor increases, both Cases 1 and 2 show delayed responses in the X and Y direction acceleration tracking as expected. However, we can observe that the Z-directional performance of the Case 2 remains the same regardless of the magnitude of the MOI, unlike Case 1 where the performance degradation is observed. The effect of the decline in Z-directional control performance on the system is evident when controlling the position of the multi-rotor. The bottom set of figures is the situation where the high-level position controller generates the desired acceleration command to track the predefined trajectory. In Case 1, we can observe a decrease in acceleration tracking performance in both the X and Y directions as well as the Z direction as the MOI increases. On the other hand, in Case 2, the Z-directional control performance remains constant regardless of the MOI of the platform, stabilizing the X and Y-directional control performance faster than Case 1.

This phenomenon can be understood in other ways by considering the role of the denominator term of the T_t equation in Equation (3.4), which is to compensate for the reduction of the vertical thrust component in the sense of inertial coordinates when the multi-rotor is tilted. When $T_{t,d}$ is calculated based on the desired attitude as Equation (3.7), the situation is similar to compensating for the future event after γ_h seconds. Instead, it is intuitive to use the current attitude as in Equation (3.15) to correct the vertical thrust reduction.

From the flight results using Equation (3.15) in Fig. 3.2, we can confirm that the control performance in all directions is satisfactory.
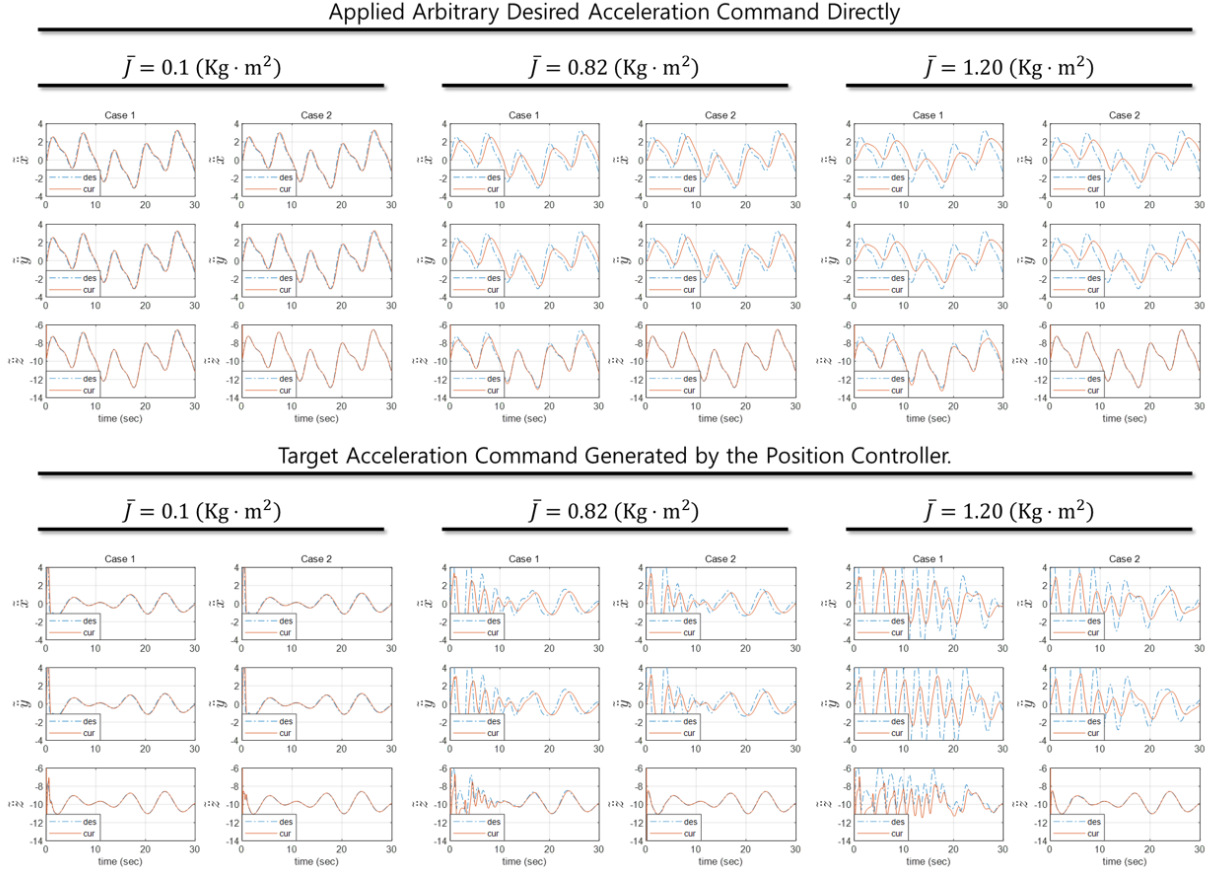
Figure 3.2: [Simulation] A comparison of cases where acceleration command is converted into a target attitude and a thrust signal using Equations (3.5), (3.6) and (3.7) (Case 1), and using Equations (3.5), (3.6) and (3.15) (Case 2) for multi-rotors with different MOI. Acceleration motions are simulated for two scenarios : in the first scenario, an arbitrary target acceleration command is applied (top), and the target acceleration is generated via a position controller that tracks the predefined desired trajectory in the second scenario (bottom).

3.3 Disturbance observer

External disturbances applied to multi-rotor act not only in the form of translational disturbances but also in the form of rotational torques. However, given that a number of solutions for overcoming the rotational torque disturbances [10]~ [17] have already been proposed, this section concerns only translational disturbances applied to the system for straightforward discussion and analysis.

3.3.1   An overview of the disturbance-merged overall system

Fig. 3.3 shows the overall configuration of the system. First, the position controller $C(t)$ generates the target acceleration input $\ddot{\mathbf{X}}_d$. This signal is then transformed into the target force input $\mathbf{F}_d$ through the following force-acceleration relationship:

$$\mathbf{F} = m(\ddot{\mathbf{X}} - \mathbf{g}). \tag{3.17}$$

Then, $\mathbf{F}_d$ signal passes through $\frac{1}{m}R^{-1}(\psi)$ block to transform the signal into the $\tilde{\ddot{\mathbf{X}}}_d$ $\big($refer Equation (3.2)$\big)$. The signal $\tilde{\ddot{\mathbf{X}}}_d$ then passes through the $\mathbf{B}_{[\tilde{\ddot{\mathbf{x}}}_d \to \mathbf{r}_d]}$ block, which converts the target acceleration $\tilde{\ddot{\mathbf{X}}}_d$ to $\mathbf{r}_d$, the input to the multi-rotor controller, based on Equations (3.5), (3.6) and (3.15). Once $\mathbf{r}_d$ passes through the dynamics described in Fig. 3.1 and outputs $\mathbf{r}$, it passes through $\mathbf{B}_{[\mathbf{r} \to \mathbf{F}]}$ block to produce $\mathbf{F}$ $\big($refer Equation (3.2) and (3.3)$\big)$. Right after $\mathbf{F}$ is generated, the external disturbance force $\mathbf{d}_{actual}$ immediately compromises the thrust and results in $\tilde{\mathbf{F}}$ and $\ddot{\mathbf{X}}$.

3.3.2   Disturbance observer

In Fig. 3.3, the translational force disturbance $\mathbf{d}_{actual}$ is combined with $\mathbf{F}$ to become $\tilde{\mathbf{F}}$. However, canceling $\mathbf{d}_{actual}$ is only possible by adding an appropriate disturbance cancellation term to the $\mathbf{F}_d$ signal. Therefore, it is preferable to assume that there is an equivalent input disturbance $\mathbf{d}_{EID}$ that has the same effect on the system as $\mathbf{d}_{actual}$ [37]. Then $\mathbf{d}_{actual}$
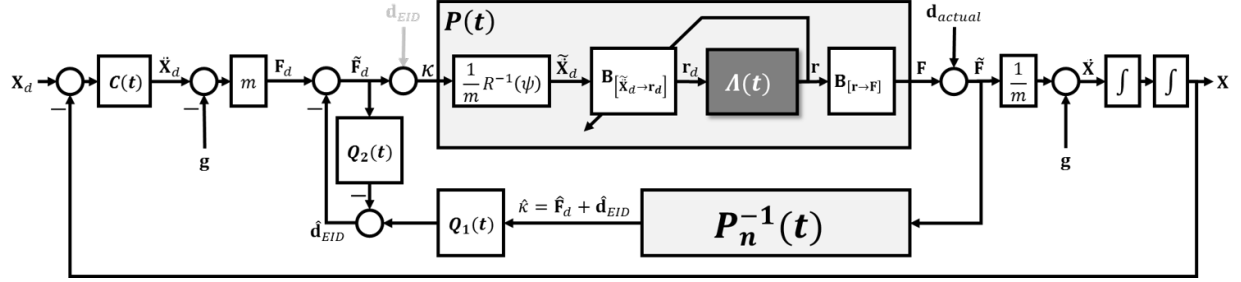
Figure 3.3: Overall system diagram with DOB structure. $C(t)$: Outer-loop controller, $\mathbf{F}_d$: Desired translational force vector, $\tilde{\mathbf{F}}_d$: Sum of $\mathbf{F}_d$ and disturbance cancellation signal $-\hat{\mathbf{d}}_{EID}$, $\mathbf{B}_{[\tilde{\mathbf{x}}_d \to \mathbf{r}_d]}$: $\tilde{\ddot{\mathbf{X}}}_d$ to $\mathbf{r}_d$ translator (eq. (3.5), (3.6), (3.15)), $\Lambda(t)$: Plant dynamics (Fig. 3.1, Eq. (2.4)), $\mathbf{B}_{[\mathbf{r} \to \mathbf{F}]}$: $\mathbf{r}$ to $\mathbf{F}$ translator (Eq. (3.2), (3.3)), $\mathbf{F}$: Force vector generated by the multi-rotor, $\tilde{\mathbf{F}}$: Sum of $\mathbf{F}$ and actual disturbance $\mathbf{d}_{actual}$, $P_n(t)$: Nominal model of $P(t)$, $Q_{1,2}(t)$: Q-filters for DOB.

is replaced by $\mathbf{d}_{EID}$, making $\mathbf{F} = \tilde{\mathbf{F}}$. As we can see in Fig. 3.3, the $\mathbf{d}_{EID}$ signal is merged into $\tilde{\mathbf{F}}_d$, which is the translational acceleration control input with disturbance cancellation signal. Now, let us construct the DOB based on the above settings.

3.3.2.1 $\mathbf{d}_{EID}$ estimation algorithm

For the estimation of $\mathbf{d}_{EID}$, we first estimate κ the sum of $\tilde{\mathbf{F}}_d$ and $\mathbf{d}_{EID}$ by

$$\hat{\kappa}(s) = \hat{\tilde{\mathbf{F}}}_d(s) + \hat{\mathbf{d}}_{EID}(s) = P_n^{-1}(s)\tilde{\mathbf{F}}(s). \tag{3.18}$$

We can easily achieve the $\tilde{\mathbf{F}}$ signal from Equation (3.17) where $\ddot{\mathbf{X}}$ is measured by the IMU sensor. The transfer function $P_n(s)$ is the nominal model of $P(s)$, and $(\hat{*})$ is the representation of the estimation of $(*)$ signal throughout this chapter. Once we estimate $\hat{\kappa}$, we then obtain $\hat{\mathbf{d}}_{EID}$ by

$$\hat{\mathbf{d}}_{EID} = Q_1(s)\hat{\kappa}(s) - Q_2(s)\tilde{\mathbf{F}}_d(s). \tag{3.19}$$

The signal $\hat{\kappa}(s)$ passes through the Q_1 block, which is basically a low pass filter, to overcome both the causality violation issue due to the improperness of $P_n^{-1}(s)$ and the potential instability issue caused by the non-minimum phase characteristic of $P_n(s)$. The filter $Q_2(s)$
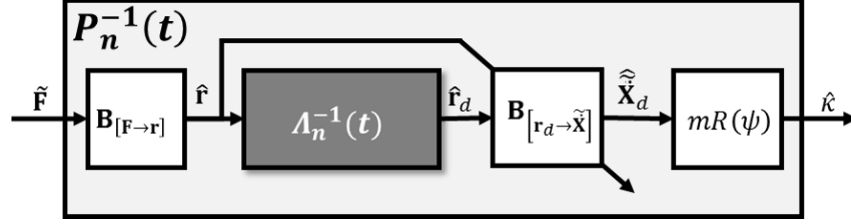
Figure 3.4: Configuration of $P_n^{-1}(t)$. The $P_n^{-1}(t)$ block is composed of the opposite order of $P(t)$, where $\Lambda_n(t)$ is the nominal model of $\Lambda(t)$.

is used to match the phase with $Q_1(s)\hat{\kappa}(s)$ signal. In the end, we generate a disturbance-compensating control input $\tilde{\mathbf{F}}_d$ by

$$\tilde{\mathbf{F}}_d = \mathbf{F}_d - \hat{\mathbf{d}}_{EID}. \tag{3.20}$$

This makes κ become

$$\kappa = \tilde{\mathbf{F}}_d + \mathbf{d}_{EID} = \mathbf{F}_d - \hat{\mathbf{d}}_{EID} + \mathbf{d}_{EID} \approx \mathbf{F}_d. \tag{3.21}$$

The most important factor in the $\mathbf{d}_{EID}$ estimation process is the proper design of P_n and Q. Of these, Q is deeply related to the stability of the system and will be discussed in more detail in the next section. In the remainder of this section, we first discuss the design of the nominal model P_n and then explain the structure of the Q-filter.

3.3.2.2 Nominal model P_n

The internal structure of $P_n^{-1}(t)$ is described as in Fig. 3.4, all of which are simple conversion blocks except for the $\Lambda_n^{-1}(t)$ block. The block $\Lambda(t)$ is the relationship between $\mathbf{r}_d$ and $\mathbf{r}$ depicted in Fig. 3.1. The $\Lambda_n(s)$ is constructed from two parts: attitude and thrust dynamics. We denote these as $\Lambda_{n,a}(s)$ and $\Lambda_{n,t}(s)$ respectively.

As we see from Fig. 3.1, $\Lambda_{n,a}(s)$ is constructed with attitude controller, rotor dynamics and attitudinal dynamics. Since rotor dynamics can be ignored, we only need to find the transfer function of the attitudinal dynamics and attitude controller. For attitude dynamics,

let us refer to Equation (2.3) and express it as

$$\frac{\mathbf{q}_i(s)}{\mathbf{T}_{r,i}(s)} = \frac{1}{J_i s^2}, \tag{3.22}$$

where $i = 1, 2, 3$ represent ϕ, θ, ψ axis, respectively. For attitude control, PD control in the following form is used.

$$\frac{\mathbf{T}_{r,i}(s)}{\mathbf{q}_{i,d}(s) - \mathbf{q}_i(s)} = P_i + D_i s \tag{3.23}$$

The parameters P_i, D_i represent control gains in each attitude component. Then, the overall transfer function $\Lambda_{n,a,i}$ between desired and current attitude becomes

$$\Lambda_{n,a,i}(s) = \frac{\mathbf{q}_i(s)}{\mathbf{q}_{i,d}(s)} = \frac{D_i s + P_i}{J_i s^2 + D_i s + P_i}. \tag{3.24}$$

In the case of $\Lambda_{n,t}$, the only dynamics involved is rotor dynamics, which we decided to neglect. Thus, it can be expressed as

$$\Lambda_{n,t}(s) = 1. \tag{3.25}$$

Now, we can construct the transfer matrix for $\Lambda_n = diag(\Lambda_{n,1}, \Lambda_{n,2}, \Lambda_{n,3})$ using Equations (3.24) and (3.25) as

$$\Lambda_n(s) = \begin{bmatrix} \Lambda_{n,a,2}(s) & 0 & 0 \\ 0 & \Lambda_{n,a,1}(s) & 0 \\ 0 & 0 & \Lambda_{n,t}(s) \end{bmatrix}. \tag{3.26}$$

Equation (3.26) is a detailed representation of the relationship between $\mathbf{r}_d$ and $\mathbf{r}$, which was introduced in Equation (3.8). On the other hand, P_n, which defines the nominal relationship between κ and $\mathbf{F}$ $\left(\text{or } \tilde{\tilde{\mathbf{X}}}_d \text{ and } \tilde{\tilde{\mathbf{X}}} \right)$, was introduced in Equation (3.16) $\left(\text{refer Equation (3.2) for the relationship between } \tilde{\tilde{\mathbf{X}}} \text{ and } \mathbf{F} \right)$. Here, we can see that both Equations (3.8) and (3.16) have the same input/output characteristics with time delay of γ_h for the first and second channels and no time delay for the third channel. Therefore, we can conclude

25

that $\Lambda_n(s)$ in Equation (3.26) is also the transfer function between κ and $\mathbf{F}$ as well as between $\mathbf{r}_d$ and $\mathbf{r}$, which is

$$P_n(s) = \Lambda_n(s). \tag{3.27}$$

3.3.2.3 Q-filter design

In Q-filter design, we choose to make $Q_1(s)\Lambda_n^{-1}(s)$, which is now identical to $Q_1(s)P_n^{-1}(s)$, a proper function with relative degree of 1. Since $P_n(s)$ is composed of three channels in X, Y and Z directions, we need to design three separate Q-filters. As shown in Equation (3.24), $\Lambda_{n,1}(s)\big(= \Lambda_{n,a,2}(s)\big)$ and $\Lambda_{n,2}(s)\big(= \Lambda_{n,a,1}(s)\big)$ among the three transfer functions of $\Lambda_n(s)$ are systems with a relative degree of 1. The thrust transfer function $\Lambda_{n,3}(s)\big(= \Lambda_{n,t}(s)\big)$ has a relative degree of 0, as can be seen from Equation (3.25). Therefore, the Q-filters for making $Q_1(s)\Lambda_n^{-1}(s)$ with a relative degree of 1 are designed as

$$Q_1(s) = diag\big(Q_{1,h}(s), Q_{1,h}(s), Q_{1,v}(s)\big), \tag{3.28}$$

$$Q_{1,h}(s) = \frac{1}{(\tau_1 s)^2 + \zeta(\tau_1 s) + 1}, \tag{3.29}$$

$$Q_{1,v}(s) = \frac{1}{(\tau_2 s) + 1}, \tag{3.30}$$

where $Q_{1,h}$ and $Q_{1,v}$ are Q-filters corresponding to the horizontal ($\Lambda_{n,a}$) and vertical (Λ_t) models respectively. The symbol τ is the time constant and ζ is the damping ratio of the filter. The filter Q_1 is designed to have a gain of 1 when $s = 0$ [38]. The filter Q_2 is set to $Q_2 = Q_1$, to easily achieve the purpose of phase matching.

3.4 Stability analysis

The design of Q-filter in the DOB structure should be based on rigorous stability analysis to ensure the overall stability. In particular, we note that there is always a difference between the nominal model $P_n(s)$ and the actual model $P(s)$, due to various uncertainties and

applied assumptions.

Although the small-gain theorem (SGT) [20] can still be a tool for stability analysis, the SGT analysis based on the largest singular value among uncertainties is likely to yield overly conservative results especially if multiple uncertain elements are involved. Instead, we use structured singular value analysis, or μ-analysis [39–41], to reflect the combined effects of uncertainties.

3.4.1 Modeling of $P(s)$ considering uncertainties

The multi-rotor's actual transfer function $P(s)$ between κ and $\mathbf{F}$ in Fig. 3.3 is

$$P(s) = diag\big(P_1(s), P_2(s), P_3(s)\big). \tag{3.31}$$

Here, P_1, P_2 and P_3 represent the input/output translational force relationship in the X, Y, and Z directions, respectively. This research considers a small but nonzero DC-gain error, parametric error and phase shift error between $P_n(s)$ and $P(s)$. Then each $P_j(s)$ can be expressed as the following equation:

$$\begin{aligned} P_j(s) &= K_j P_{n,j}(s)e^{-\delta_j s} \\ &= K_j \Lambda_{n,j}(s)e^{-\delta_j s} = P_{p,j}(s)\Gamma_j(s), \end{aligned} \tag{3.32}$$

where $j = 1, 2, 3$ represent X, Y, Z axis. The symbols $K_j, \delta_j \in \mathbb{R}$ represent the uncertain variable gain and time delay parameters, respectively. The nominal transfer function $P_{n,j}$ can be replaced by $\Lambda_{n,j}$ based on Equation (3.27). The portion containing only the parametric uncertainty is denoted by $P_{p,j}(s) = K_j \Lambda_{n,j}(s)$, and the time delay uncertainty is denoted by $\Gamma_j(s) = e^{-\delta_j s}$.

In Equation (3.32), each $P_j(s)$ contains three uncertain variables, which are K_j, J_j and δ_j. In the case of K_j, we define K_j as

$$K_j = 1 + K_{\Delta,j}, \tag{3.33}$$
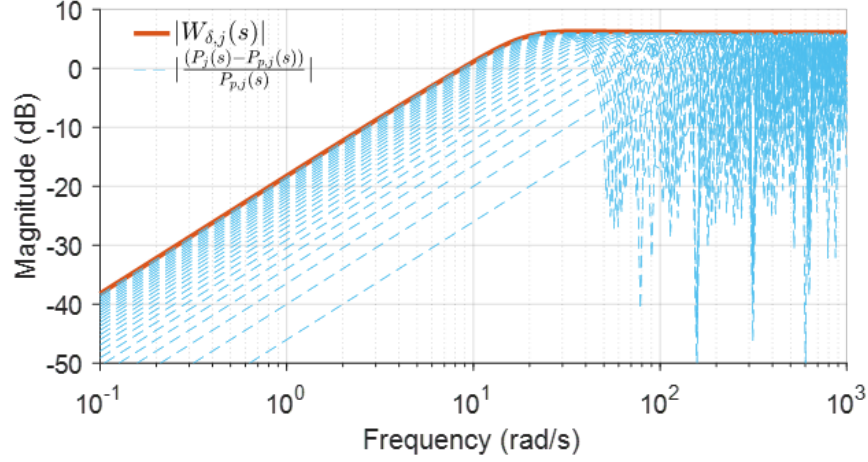
Figure 3.5: Bode magnitude plots of $\Gamma_j(s) - 1$ expressed by varying δ_j from -0.12 to 0.12 (blue dashed line), maximum uncertainty $W_{\delta,j}(s)$ (red solid line).

where $K_{\Delta,j} \in \mathbb{R}$ is the error value of K_j. In the case of J_j, determining the actual value of J_j is difficult compared to other physical quantities. We also define J_j in the same manner as K_j for the convenience of analysis as

$$J_j = \bar{J}_j(1 + J_{\Delta,j}), \tag{3.34}$$

where $\bar{J}_j, J_{\Delta,j} \in \mathbb{R}$ are the nominal and error values of J_j. Because the term $\Gamma_j(s)$ containing δ_j is of an irrational form that is not suitable for analysis, we use an analytic approximation of the uncertain time-delay $\Gamma_j(s)$ to a rational function with unmodeled dynamic uncertainty [41]. First, we change the representation of the $P_j(s)$ model to a multiplicative uncertainty form that combines parametric uncertainties and unmodeled time-delay uncertainty as follows:

$$P_j(s) = P_{p,j}(s)\big(1 + \Delta_{\delta,j}(s)W_{\delta,j}(s)\big), \tag{3.35}$$
$$||\Delta_{\delta,j}(s)||_\infty \leq 1.$$

A complex unstructured uncertainty $\Delta_{\delta,j} \in \mathbb{C}$ corresponds to unknown time delay δ_j, and $W_{\delta,j}(s)$ is the maximum uncertainty that can be caused by $\Gamma_j(s)$. Here, we can obtain

$W_{\delta,j}(s)$ using Equation (3.32) as

$$W_{\delta,j}(s) = \max_{\delta_j} \left| \frac{P_j(s) - P_{p,j}(s)}{P_{p,j}(s)} \right| = \max_{\delta_j}|\Gamma_j(s) - 1|. \tag{3.36}$$

The maximum value of $|\Gamma_j(j\omega) - 1|$ for each ω can be found using Euler's formula as

$$\max_{\delta_j}|\Gamma_j(j\omega) - 1| = \max_{\delta_j}\sqrt{\left(\cos\left(\omega\delta_j\right) - 1\right)^2 + \left(\sin\left(\omega\delta_j\right)\right)^2} \tag{3.37}$$

where

$$\Gamma_j(j\omega) = e^{\delta_j(j\omega)} = \cos\left(\omega\delta_j\right) + j\sin\left(\omega\delta_j\right). \tag{3.38}$$

As a result of analyzing a large amount of actual experimental data, we confirmed that the time delay between $P_n(s)\left(= \Lambda_n(s)\right)$ and $P(s)$ does not exceed 0.1 second in all three channels. We put 20 percent margin so that $|\delta_j| \leq 0.12$. Fig. 3.5 is multiple Bode magnitude plots of $|\Gamma(s)-1|$ generated by varying δ from -0.12 to $+0.12$. From Fig. 3.5, we can extract

$$W_{\delta,j}(s) = \frac{2.015s^3 + 52.88s^2 + 431.6s + 0.415}{s^3 + 36.7s^2 + 606.8s + 3521} \tag{3.39}$$

for all j, which is the upper boundary of $|\Gamma_j(s) - 1|$ sets represented by the red solid line.

The uncertainties of K_j and J_j can also be modeled in the same manner as in Equation (3.35) as

$$\begin{cases} P_{p,j}(s) = K_j\Lambda_{n,j}(s) = \Lambda_{n,j}(1 + \Delta_{K,j}W_{K,j}) \\ \Lambda_{n,j}(s) = \Lambda_{n,n,j}(s)(1 + \Delta_{J,j}W_{J,j}), \end{cases} \tag{3.40}$$

where $||\Delta_{K,j}||_\infty, ||\Delta_{J,j}||_\infty \leq 1$. The transfer function $\Lambda_{n,n,j}$ is basically the same as $\Lambda_{n,j}$, except that J in Equation (3.24) is replaced to the nominal MOI value $\bar{J}$. The transfer

functions $W_{K,j}$ and $W_{J,j}$ are

$$W_{K,j} = \max|K_{\Delta,j}| \tag{3.41}$$

$$W_{J,j} = \begin{cases} \max\limits_{J_{\Delta,j}} \left| \dfrac{-\bar{J}_j J_{\Delta,j} s^3}{J_j (1+J_{\Delta,j}) s^3 + D_j s^2 + P_j s + I_j} \right| & (j=1,2) \\ 0 & (j=3). \end{cases}$$

3.4.2 τ-determination through μ-analysis

3.4.2.1 μ-robust stability analysis

In [42], the structured singular value μ is defined as

$$\mu_\Delta(M_{11}) = \frac{1}{\min\limits_{\Delta \in \boldsymbol{\Delta}} \left(\bar{\sigma}(\Delta) : \det(I - M_{11}\Delta) = 0 \right)} \tag{3.42}$$

where Δ is a complex structured block-diagonal unmodeled uncertainty block which gathers all model uncertainties [43]. Following the common notation, the symbol $\boldsymbol{\Delta}$ represents a set of all stable transfer matrices with the same structure (full, block-diagonal, or scalar blocks) and nature (real or complex) as Δ. The $\bar{\sigma}(\Delta)$ is the maximum singular value of uncertainty block Δ. The matrices M and Δ are defined by collapsing the simplified overall system to upper LFT uncertainty description as

$$\begin{bmatrix} z \\ y \end{bmatrix} = \begin{bmatrix} M_{11} & M_{12} \\ M_{21} & M_{22} \end{bmatrix} \begin{bmatrix} w \\ r \end{bmatrix}, \quad w = \Delta z, \tag{3.43}$$

where M is the known part of the system, r is a reference input and y is an output of the overall system. In the theory of the μ-analysis, it is well-known that the system is robustly stable if μ satisfies the following conditions

$$\mu_\Delta(M_{11}) < 1, \ \forall \omega \tag{3.44}$$
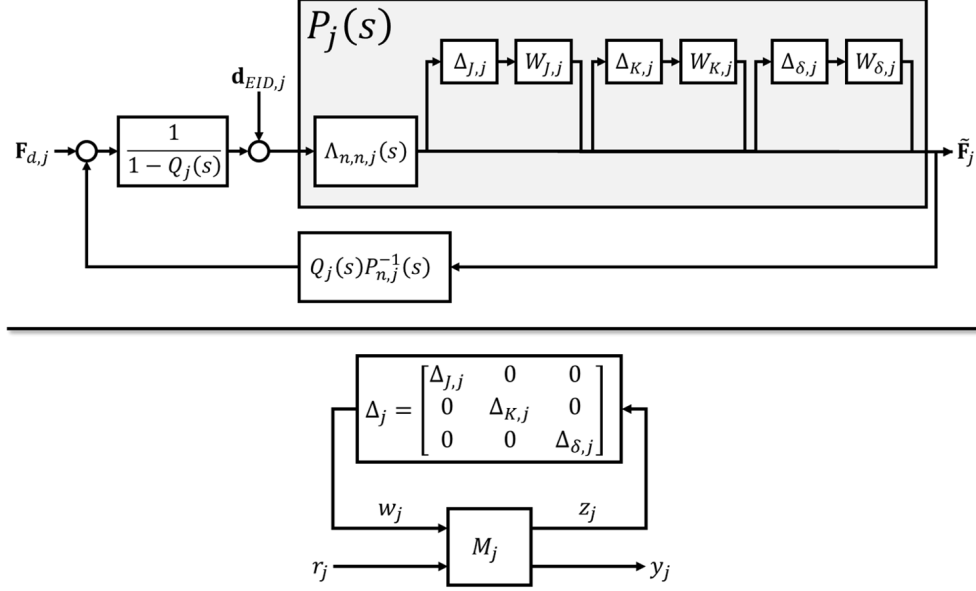
Figure 3.6: Compressed block digram of the DOB-included transfer function from $\mathbf{F}_{d,j}$ to $\tilde{\mathbf{F}}_j$, whose original form was shown in Fig. 3.3 (top), further collapsed form expressed as a nominal closed-loop system M_j and a complex unstructured uncertainty block Δ_j as in Equation (3.45) (bottom).

[39] [42].

The μ-analysis is performed separately for each channel of X, Y, Z thanks to the structure of the platform described by Equation (28), but since X and Y channels are composed of the same structure, they share the identical analysis result. As we can see from Fig. 3.6, the system is collapsed in the form of Equation (3.43) by using MATLAB's Robust Control Toolbox^{TM}, where $r_j = [\mathbf{F}_{d,j} \ \mathbf{d}_{EID,j}]^T \in \mathbb{R}^{2\times 1}$ and $y_j = \tilde{\mathbf{F}}_j \in \mathbb{R}$ in our case. As a reminder, subscript j refers to each channel of X, Y, and Z. Also, structured uncertainty $\Delta_j(s) \in \mathbb{C}^{3\times 3}$ is constructed as

$$\Delta_j(s) = diag\big(\Delta_{J,j}(s), \Delta_{K,j}(s), \Delta_{\delta,j}(s)\big), \tag{3.45}$$

which includes unmodeled MOI uncertainty, time and gain uncertainty in our system.
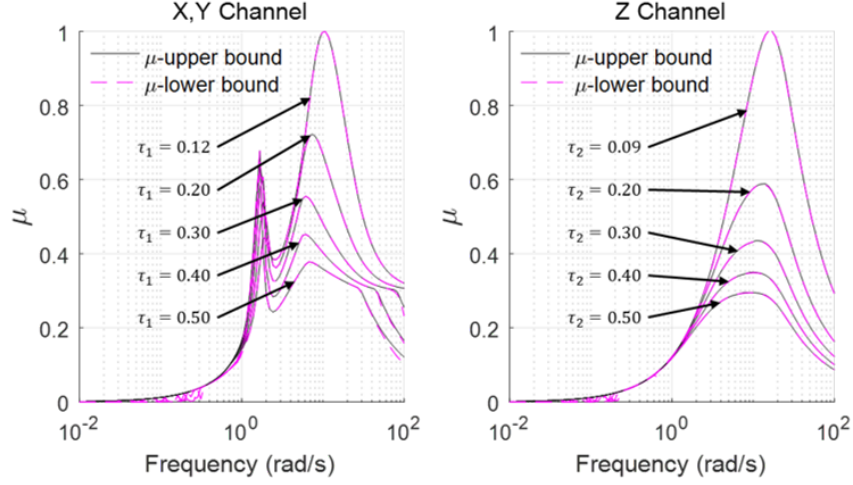
Figure 3.7: μ-analysis results for X, Y channel (left), and Z channel (right).
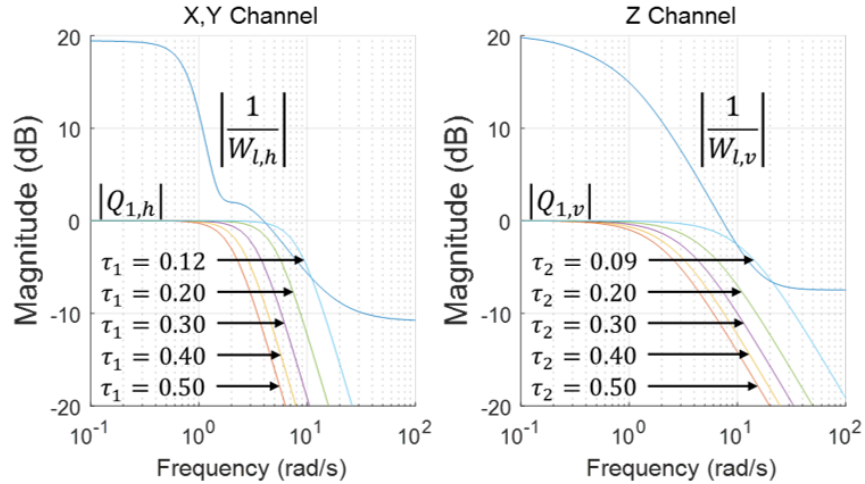
Figure 3.8: SGT-based analysis results for X, Y channel (left), and Z channel (right).

3.4.2.2   Results of analysis

Table 3.1 shows the multi-rotor's physical quantities and controller gains used both in the simulation and the experiment. The gains $P_{\phi,\theta}$ and $D_{\phi,\theta}$ are predefined values set during the primary gain-tuning process to obtain the ability to control the attitude of the platform. The translational acceleration limit is set to prevent flight failure due to excessive acceleration control inputs and is set at ± 3 m/s^2 to have a roll and pitch limit of approximately ± 0.3 rad in level flight condition. As previously mentioned, the unmodeled time delay δ_j is set to

0.1, and the gain error is assumed to be a maximum error of 10 percent. For MOIs that are difficult to estimate, we assumed a wider 30 percent uncertainty. The damping ratio ζ of the second order filter is set to 0.707, which is the critical damping ratio, to balance the overshoot and late response. Fig. 3.7 shows the results of μ-analysis. From the analysis, we can see that the system is stable when $\tau_1 > 0.12$ and $\tau_2 > 0.09$.

Fig. 3.8 shows the results of the SGT-based stability analysis, performed in the same manner as [20]. The analysis is based on the following model:

$$P_j(s) = \Lambda_{n,n,j}(s)(1 + \Delta_{l,j} W_{l,j}), \ ||\Delta_{l,j}||_\infty \le 1, \tag{3.46}$$

where all uncertainties due to δ_j, K_j and J_j are lumped using the functions $W_{l,h}(= W_{l,1}, W_{l,2})$ and $W_{l,v}(= W_{l,3})$, whose magnitude increases over frequency as shown in blue curves of Fig. 3.8. The stability condition of the SGT-based analysis in this case is

$$\bar{\sigma}\big(Q_j(j\omega)\big)\bar{\sigma}\big(W_{l,j}(j\omega)\big) < 1 \tag{3.47}$$

[20, 39, 44]. In the SGT-based analysis, the bode plots of the Q-filter with $\tau_1 = 0.12$ and $\tau_2 = 0.09$ indicate that system with those τ values could be unstable. However, through the μ-analysis, those τ values are still in the stable region. From this, we can confirm that the μ-analysis provides more rigorous τ boundary values than SGT-based analysis.

Table 3.1: Physical quantities and controller gains

Name	Value	Name	Value
$P_{\phi,\theta}$	3	Mass	3.24 Kg
$D_{\phi,\theta}$	1	$\bar{J}_{1,2}$	$0.82 \ \text{Kg} \cdot \text{m}^2$
$\ddot{\mathbf{X}}$ Limit	$\pm 3 \ \text{m/s}^2$	$\bar{J}_3$	$1.49 \ \text{Kg} \cdot \text{m}^2$
$\max |\delta_j|$	0.12	$\max |J_{\Delta,j}|$	0.3
$\max |K_{\Delta,j}|$	0.1	ζ	0.707

3.5 Simulation and experimental result

This section reports simulation and experimental results to validate the performance of our three-dimensional force controller and the disturbance cancellation performance of the DOB technique. The comparison of the acceleration tracking performance of the force control methods according to the MOI variation is already shown in the simulation of Fig. 3.2. Therefore, in this section, we provide

1. experimental result to demonstrate the performance of the proposed force control technique for the actual plant, and

2. simulation and experimental results to demonstrate the capability of the DOB in overcoming the translational force disturbance.

Based on the results from the previous section, the cutoff frequencies of the Q-filter are set to $\tau_1 = 0.15$ and $\tau_2 = 0.12$ in both simulation and actual experiment with additional margins to ensure additional stability.

3.5.1 Validation of acceleration tracking performance

In the experiment, arbitrary desired acceleration commands for X and Y directions are given by the operator-controlled radio controller. Fig. 3.9 shows the multi-rotor accurately following the target acceleration. From this result, we can confirm that our three-dimensional translational acceleration control technique functions effectively even in the actual flight.

3.5.2 Validation of DOB performance

3.5.2.1 Simulation result

In the simulation, the multi-rotor follows a circular trajectory with radius of 3 m and height of 5 m. Meanwhile, the multi-rotor is exposed to periodic disturbances with accelerations up
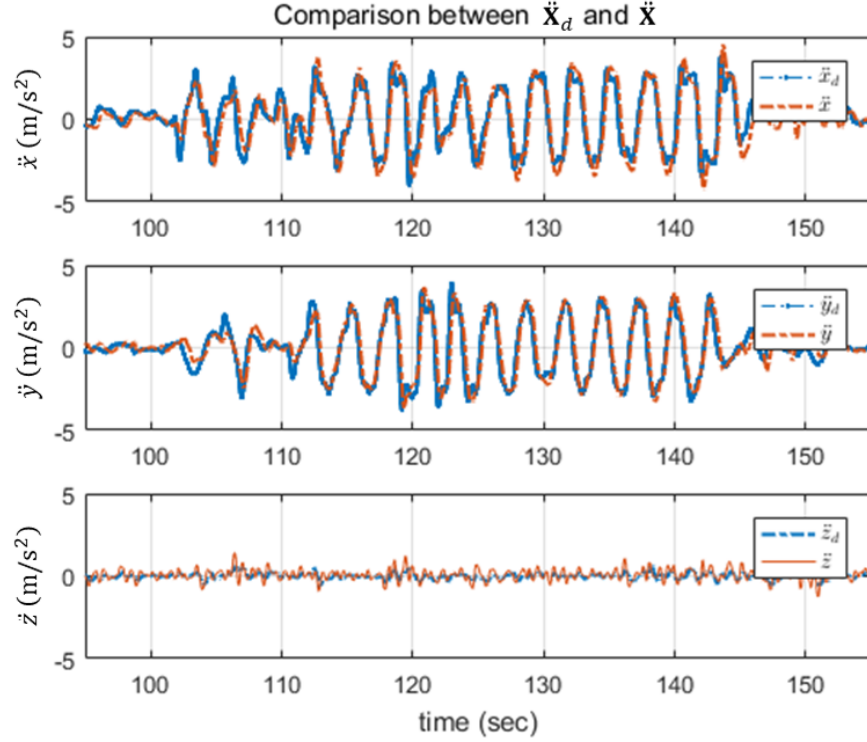
Figure 3.9: [Experiment] Desired 3-D acceleration generated by the operator through the R/C controller (blue), and the actual acceleration (red dash) generated by multi-rotor.

to 5.5 m/s^2 in each axis. Fig. 3.10 compares the multi-rotor's position tracking performance before and after applying DOB. On the left graphs of Fig. 3.10, the target trajectory tracking results are not smooth due to the unexpected disturbances, whereas the trajectory deviation is drastically reduced in the right graphs where the DOB algorithm is applied.

3.5.2.2 Experimental Result

In the experiment, the multi-rotor is commanded to hover at a specific point in three-dimensional space but connected to the translational force measurement sensor via the tether to measure the applied disturbance force. As we can see in Fig. 3.12, the operator aligns the force sensor in the X-axis and pulls and releases the force sensor periodically to apply a disturbance to the multi-rotor.

Fig. 3.11 is a comparison of hovering performance before (left) and after (right) applying
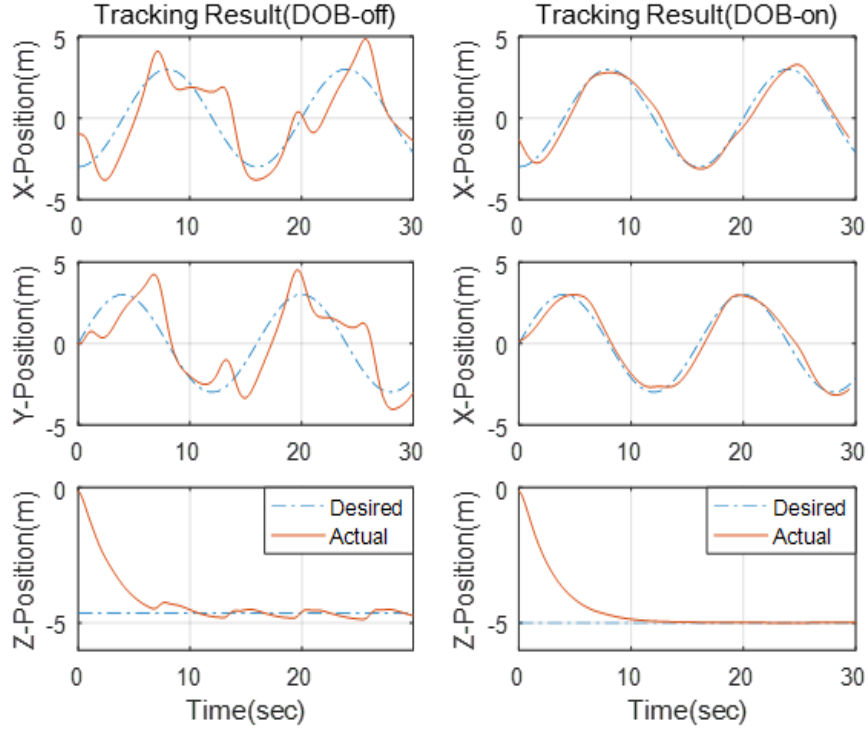
Figure 3.10: [Simulation] Comparison of trajectory tracking performance before (left) and after (right) applying the DOB algorithm.

the DOB algorithm. The graphs in the left column are the case when the DOB is not applied, which has a larger X directional position shift than other axes. Unlike the DOB-off case, the DOB-on case shows a significant reduction in position error. Two graphs at the forth row shows the acceleration tracking results. When DOB is not applied, an acceleration signal is generated by the position error, but we can see that the target acceleration cannot be followed due to the disturbance. Meanwhile, we can see that the acceleration of the platform (yellow solid line) well tracks the target acceleration (blue dash-single dotted line). This is because the well-behaved DOB algorithm generated control input including the disturbance compensation signal (orange dash-single dotted line) and applied to the platform. The effect of the DOB can be confirmed by significantly reduced position error. Four graphs at the bottom of the figure show the difference between the signal $\vec{\mathcal{F}}_d$ and $\tilde{\vec{\mathcal{F}}}_d$ (fifth row), and the comparison between $d_{actual,x}$ measured by force sensor and $\hat{d}_{EID,x}$
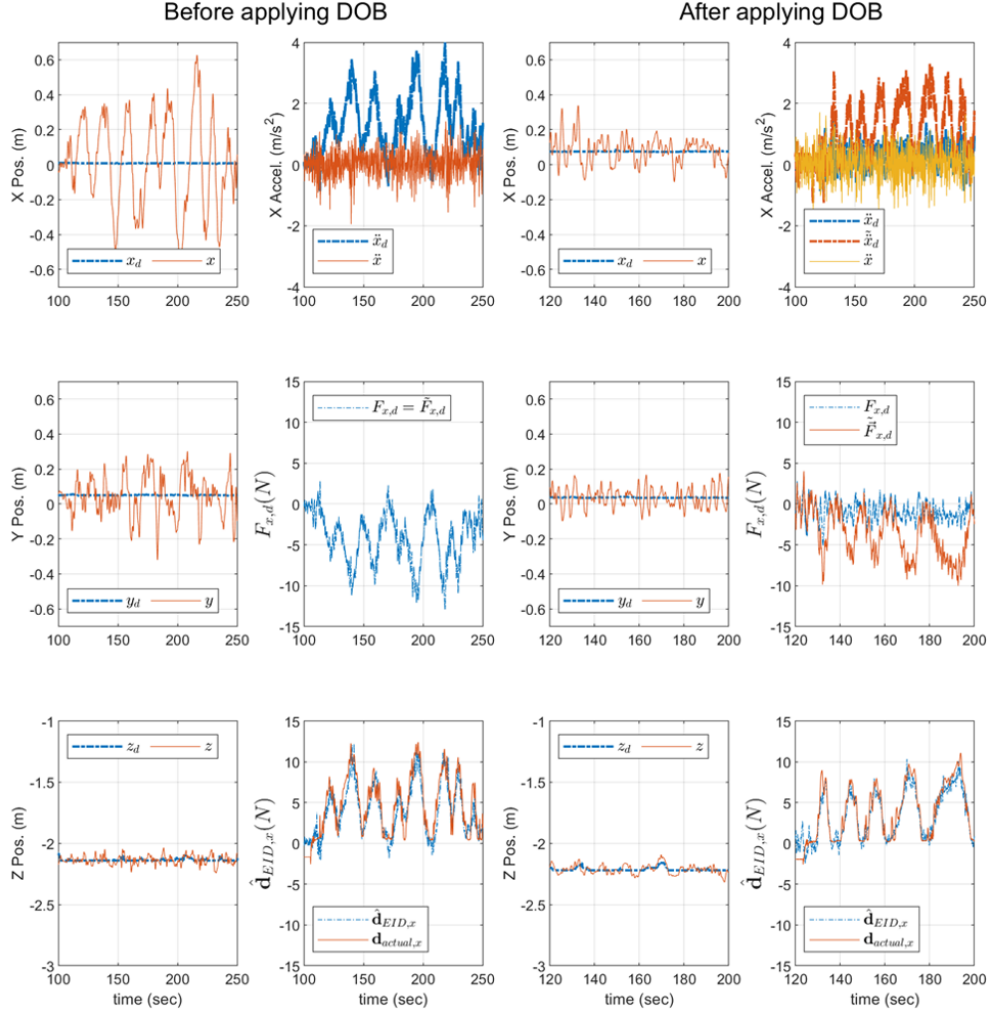
Figure 3.11: Comparison of the target position tracking performance before (left) and after (right) the DOB algorithm is applied.

estimated by DOB algorithm (sixth row). When DOB is not applied, $\hat{d}_{EID}$ estimation process is working internally but the signal is not merged into $\tilde{\vec{\mathcal{F}}}_d$ signal, making $\vec{\mathcal{F}}_d$ and $\tilde{\vec{\mathcal{F}}}_d$ have the same value. On the other hand, we can see the difference between the $\vec{\mathcal{F}}_d$ and the $\tilde{\vec{\mathcal{F}}}_d$ signal when DOB is applied, because the $\hat{d}_{EID}$ signal is merged into the $\tilde{\vec{\mathcal{F}}}_d$ signal. Two graphs in the last row show the comparison between the measured disturbance and the estimated disturbance, and we can confirm that the estimates are fairly accurate in both cases.

An extra flight experiment is conducted under wind disturbance to validate the DOB
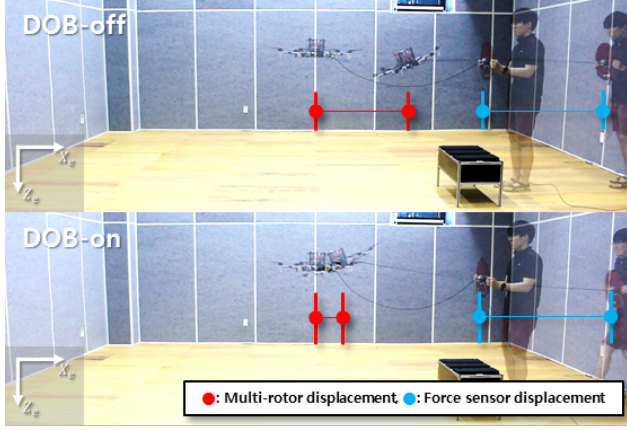
Figure 3.12: Experiment for DOB performance validation with disturbance using a tether. A force sensor is attached to the tether only to check the disturbance estimation performance.
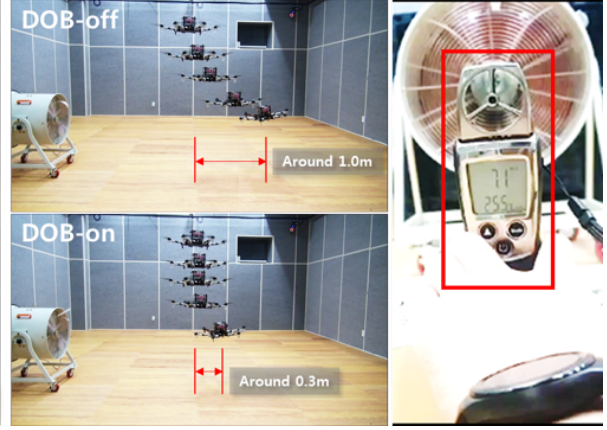
Figure 3.13: Comparison of the target position tracking performance in wind blast environment using an industrial fan.

performance in a more realistic environment. As we can see in Fig. 3.13, the target location of the multi-rotor is set on the centerline of a strong wind generator that generates wind speed of 7 m/s. The performance of DOB is visualized by comparing the position difference between DOB-on and DOB-off situations. the multi-rotor has a position error of about 1 m in the DOB-off case and about 0.3 m in the DOB-on case. Through the experiment, we can confirm that the proposed DOB algorithm works effectively even against a wind disturbance.

4

Fully-Actuated Multirotor Mechanism

4.1 Introduction

In this chapter, we introduce a new fully-actuated flight mechanism that effectively overcomes the under-actuation characteristics of the conventional multirotor. Insufficient controllable DOF of multirotors may reduce their applicability in various situations. For example, in multirotor-based aerial photography, camera position control and camera angle control cannot be performed simultaneously if the camera is fixed to the fuselage [2]. In multirotor-based aerial parcel delivery service using a fully attached cargo, not only the fuselage but also the payload should be tilted. If the payload or cargo has a large moment of inertia (MoI), the attitude control performance or even stability can be deteriorated [45]. In takeoff / landing of a multirotor on a slope surface, a safe motion control could be threatened because of the unwanted attitude change due to a normal force applied to the fuselage while the landing gear is in contact with the ground [46]. This unwanted attitude change generates undesired horizontal force that causes the multirotor to slip along the slope or capsize if severe. In order to overcome the above problems, it is desirable to have additional

39

controllable DOF to perform translational and rotational motion control independently and simultaneously.

Several multirotor structures have been proposed to implement 6-DOF motion control of multirotor [21–35], and they can be classified into two types. The first type [21–27] is to install the thrusters in various directions and control the sum of the thrust vectors to the desired direction and magnitude. The second type [28–35] is to attach multiple single-DOF servomotors to each thruster so that the direction of each thruster can be changed within a certain range. The first type of multirotor allows full control of the translational motion while taking any attitude. However, such mechanism tends to have low energy efficiency because all the thrust vector components other than the target direction component should be internally canceled during the collective thrust generation process. Also, due to the unique shape of the platform that is different from the existing multirotor, mounting a payload such as a sensor or a cargo could become difficult. Unlike the first type, the shape of the second type is similar to the conventional multirotor thus free from the heterogeneity problem. But this type requires numerous additional servomotors, which may increase weight and power consumption.

To overcome the disadvantages of existing fully-actuated flights, a new type of multirotor platform with a corresponding control technique is required. This requirement should include the structural simplicity of the platform (preferably similar to conventional multirotors) while improving energy efficiency by avoiding unnecessary internal force cancellation and excessive increase in the number of servomotors/actuators.

4.2 Mechanism

The structure of the T^3-Multirotor is shown in Fig. 4.1. As described in the left figure of Fig. 4.1, the hardware consists of two main parts: the upper part called the Thruster Part (TP) and the lower part called the Fuselage Part (FP). The upper part has the same structure and operation principle as a general multirotor UAV, but includes only an arm
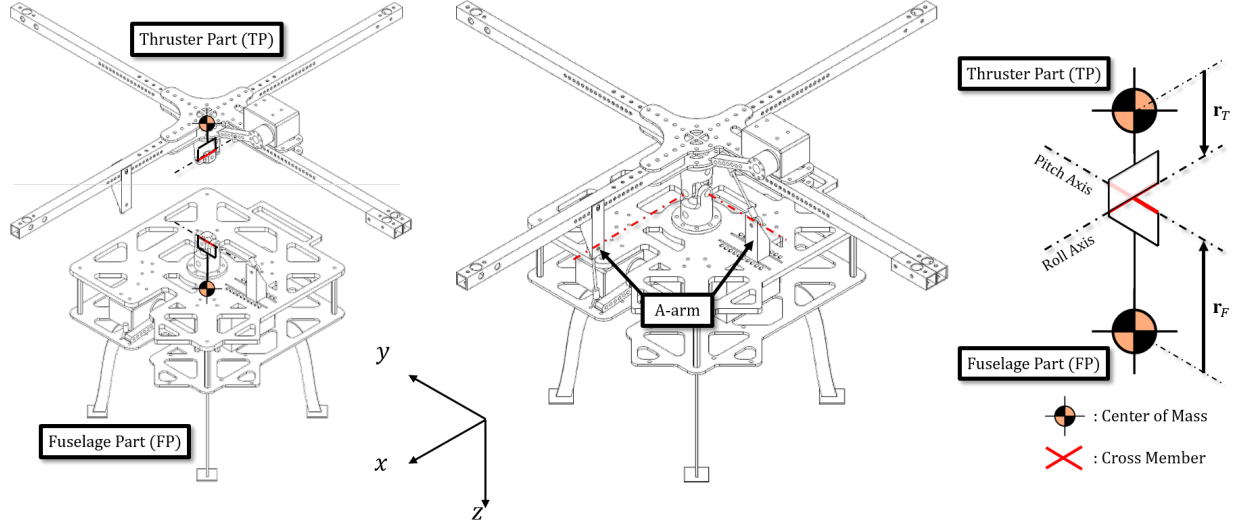
Figure 4.1: Structure of T^3-Multirotor. The T^3-Multirotor consists of two parts, TP and FP (left), and the two parts are connected via a universal joint (middle). The 'Roll Axis' and 'Pitch Axis' of the universal joint have fixed positions and orientations relative to TP and FP, respectively (right).

frame with multiple thrusters attached to the end of each arm, and an attitude sensor. The lower part contains all the remaining components for the flight, including battery, mission computer, landing gears, and various sensors.

As shown in the middle and right figures of Fig. 4.1, the upper and lower parts are connected through a universal joint mechanism to permit relative roll and pitch motion between the two parts. Then, two dedicated servomechanisms called roll and pitch servomechanism (RSM and PSM) are attached to actively control the relative attitude between the two parts. As a result, the lower part corresponding to the fuselage of the vehicle can take independent attitude by utilizing the relative attitude control of the servomechanism while the upper part controls the translational motion by controlling the attitude and the thrust in the same manner as the conventional multirotor UAV.

The operation principle of the servomechanism is as follows. From the right figure of Fig. 4.1, we can see that TP and FP each have a single axis of rotation fixed to the frame ('Roll Axis' and 'Pitch Axis', respectively), and those two rotational axes from the different part are cross-coupled through a member called a 'Cross Member' of a universal joint. Then,

RSM and PSM are placed 90 degrees apart from each other, and each servomechanism controls the relative attitude by controlling the distance between a specific point of TP and FP.

Since the relative roll motion of the platform occurs along the Roll Axis, the points on the Roll Axis are the only location of the TP where the position does not change during the relative roll motion. This feature is also applied to the FP-Pitch Axis relationship during relative pitch motion. Therefore, if the RSM controls the distance between one point on the TP and one point on the Pitch Axis, and the PSM controls the distance between one point on the FP and one point on the Roll Axis, then the relative roll and pitch attitude can be independently controlled regardless of the opponent relative attitude. To implement this concept, an 'A-arm' structure is introduced as shown in the middle figure of Fig. 4.1 to hold one end of the attachment point of the servomechanism on the axis.

4.3 Modeling

In this section, we derive the equations of motion (EoMs) of the T^3-Multirotor. Since the T^3-Multirotor consists of two parts, TP and FP, we construct independent translational and rotational motion equations for each part. However, due to the presence of universal joint and servomechanism, there is a force and torque exchange between the two parts. Therefore, in this section, we establish the translational and rotational EoMs of each of TP and FP considering such an exchange.

4.3.1   General equations of motion of TP and FP

The very right figure of Fig. 4.1 shows a schematic of a T^3-Multirotor. In the figure, TP and FP are replaced by symbols located at the center of mass (CoM) of each part. The TP and FP are connected through Cross Member (CM), one of the major components of the universal joint. The CM consists of roll and pitch axis, where TP is connected to the roll axis and FP is connected to the pitch axis. Thus, the TP can only perform relative

roll motion for the CM, and the FP can only perform relative pitch motion for the CM. Relative roll and pitch motion are controlled via the servomechanisms.

The TP can generate its own thrust and torque in the same manner as a conventional multirotor. However, the FP only receives external forces and torques from the universal joint and servomechanism. Based on these characteristics, we can establish the translational and rotational EoMs of TP and FP as

$$
\begin{cases}
m_T \ddot{\mathbf{X}}_T = \mathbf{R}(\mathbf{q}_T)\mathbf{F}_T + m_T \mathbf{g} + \mathbf{F}_{FT} \\
m_F \ddot{\mathbf{X}}_F = m_F \mathbf{g} + \mathbf{F}_{TF}
\end{cases}
\tag{4.1}
$$

$$
\begin{cases}
J_T \dot{\mathbf{\Omega}}_T = \mathbf{T}_T - \mathbf{\Omega}_T \times J_T \mathbf{\Omega}_T + \mathbf{r}_T \times \left(\mathbf{R}^{-1}(\mathbf{q}_T)\mathbf{F}_{FT}\right) + \mathbf{T}_{FT} \\
J_F \dot{\mathbf{\Omega}}_F = -\mathbf{\Omega}_F \times J_F \mathbf{\Omega}_F + \mathbf{r}_F \times \left(\mathbf{R}^{-1}(\mathbf{q}_F)\mathbf{F}_{TF}\right) + \mathbf{T}_{TF},
\end{cases}
\tag{4.2}
$$

where $m_* \in \mathbb{R}$ is the mass, $\mathbf{X}_* = [x_* \ y_* \ z_*]^T \in \mathbb{R}^{3 \times 1}$ is the position vector, $\mathbf{q}_* = [\phi_* \ \theta_* \ \psi_*]^T \in \mathbb{R}^{3 \times 1}$ is the attitude vector, $\mathbf{R}(\mathbf{q}_*) = R_y(\psi_*)R_p(\theta_*)R_r(\phi_*) \in SO(3)$ is the rotation matrix from the body frame to the Earth-fixed frame, $\mathbf{F}_T = [0 \ 0 \ -F_T]^T \in \mathbb{R}^{3 \times 1}$ is the thrust force vector generated by the TP defined in the body frame of the TP, $\mathbf{g} = [0 \ 0 \ g]^T \in \mathbb{R}^{3 \times 1}$ is the gravitational acceleration vector, and $\mathbf{F}_{ab} \in \mathbb{R}^{3 \times 1}$ is the reaction force vector acting from an object a to b defined in the Earth-fixed frame. The parameter $J_* = diag(J_{1,*}, J_{2,*}, J_{3,*}) \in \mathbb{R}^{3 \times 3}$ is the moment of inertia, $\mathbf{\Omega}_* = [p_* \ q_* \ r_*]^T \in \mathbb{R}^{3 \times 1}$ is the angular velocity vector defined in the body frame, $\mathbf{T}_T = [\tau_{r,T} \ \tau_{p,T} \ \tau_{y,T}]^T \in \mathbb{R}^{3 \times 1}$ is the torque vector generated by the TP defined in the body frame of the TP, $\mathbf{r}_* = [0 \ 0 \ r_*]^T \in \mathbb{R}^{3 \times 1}$ is the distance vector from the CoM of the TP / FP to center of the universal joint defined in the body frame, and $\mathbf{T}_{ab} \in \mathbb{R}^{3 \times 1}$ is the reaction torque vector acting from the object a to b defined in the body frame of the object b. The subscripts $(*)_T$ and $(*)_F$ represent TP and FP respectively.

Due to the universal joint mechanism, the following relationships hold between the position vectors $\mathbf{X}_T$ and $\mathbf{X}_F$

$$
\mathbf{X}_T + \mathbf{R}(\mathbf{q}_T)\mathbf{r}_T = \mathbf{X}_F + \mathbf{R}(\mathbf{q}_F)\mathbf{r}_F
\tag{4.3}
$$

and heading angles ψ_T and ψ_F

$$\psi_T = \psi_F. \tag{4.4}$$

Also, the internal forces and torques acting on the universal joint and servomechanisms follow the additional relationship by the law of action and reaction as below:

$$\begin{cases} \mathbf{F}_{TF} + \mathbf{F}_{FT} = 0 \\ \mathbf{R}(\mathbf{q}_F)\mathbf{T}_{TF} + \mathbf{R}(\mathbf{q}_T)\mathbf{T}_{FT} = 0 \end{cases}. \tag{4.5}$$

By applying equations (5.3) and (4.5) to equation (4.1), we can determine the interactive forces $\mathbf{F}_{TF}$ and $\mathbf{F}_{FT}$. However, in the case of interactive torques $\mathbf{T}_{TF}$ and $\mathbf{T}_{FT}$, torques generated by the roll and pitch servomechanisms as well as the universal joint constraint (equation (4.4)) must also be considered.

In order to obtain $\mathbf{T}_{TF}$ and $\mathbf{T}_{FT}$, we first investigate the torque components caused by a universal joint mechanism. Interactive torques between TP and FP are transferred via the CM of the universal joint. However, the CM cannot transfer roll torque to the TP, since the roll motion between TP and CM is free to rotate. Likewise, the CM cannot deliver pitch torque to the FP. Therefore, the torque applied by the CM to TP and FP can be defined as

$$\begin{cases} \mathbf{T}_{CT} = [0 \ \tau_{p,CT} \ \tau_{y,CT}]^T \\ \mathbf{T}_{CF} = [\tau_{r,CF} \ 0 \ \tau_{y,CF}]^T \end{cases}, \tag{4.6}$$

where $(*)_C$ represents the CM. The following relationship between T_{CT} and T_{CF} can be driven from the rotational EoM of the CM:

$$J_C\dot{\mathbf{\Omega}}_C = -R_r(\phi_r)\mathbf{T}_{CT} - R_p^{-1}(\theta_r)\mathbf{T}_{CF} - \mathbf{\Omega}_C \times J_C\mathbf{\Omega}_C, \tag{4.7}$$

where $\phi_r = \phi_T - \phi_F$, $\theta_r = \theta_T - \theta_F$. The matrices R_r and R_p represent the rotation matrix on a roll or pitch axis. Since the MoI of the CM is negligibly small, we can treat $J_C \approx 0$.

44

Therefore, equation (4.7) simplifies to the following equation:

$$R_r(\phi_r)\mathbf{T}_{CT} + R_p^{-1}(\theta_r)\mathbf{T}_{CF} = 0 . \tag{4.8}$$

By applying Eqn (4.6) to Eqn (4.8), we can rewrite $\mathbf{T}_{CT}$ and $\mathbf{T}_{CF}$ as

$$\begin{cases} \mathbf{T}_{CT} = \tau_{y,CT}[0 \ \tan\phi_r \ 1]^T \\ \mathbf{T}_{CF} = \tau_{y,CF}[\tan\theta_r \ 0 \ 1]^T \end{cases} , \tag{4.9}$$

and the relationship

$$\frac{1}{\cos\phi_r}\tau_{y,CT} + \frac{1}{\cos\theta_r}\tau_{y,CF} = 0 \tag{4.10}$$

holds between $\tau_{y,CT}$ and $\tau_{y,CF}$.

Next, we examine the effect of the servomechanisms on TP and FP. The torques generated by the roll and pitch servomechanisms are defined as follows

$$\begin{cases} \mathbf{T}_{rsT} = [\tau_{rsT} \ 0 \ 0]^T \\ \mathbf{T}_{psF} = [0 \ \tau_{psF} \ 0]^T \end{cases} , \tag{4.11}$$

where $\mathbf{T}_{rsT}$ and $\mathbf{T}_{psF}$ are the torques applied to the TP and FP by the RSM and PSM, respectively. Then, the reaction torques of equation (4.11) are defined as follows.

$$\begin{cases} \mathbf{T}_{rsF} = -\mathbf{R}^{-1}(\mathbf{q}_F)\mathbf{R}(\mathbf{q}_T)\mathbf{T}_{rsT} \\ \mathbf{T}_{psT} = -\mathbf{R}^{-1}(\mathbf{q}_T)\mathbf{R}(\mathbf{q}_F)\mathbf{T}_{psF} \end{cases} \tag{4.12}$$

Through equations (4.9), (4.11) and (4.12), we can express the final form of $\mathbf{T}_{TF}$ and $\mathbf{T}_{FT}$ as follows.

$$\begin{cases} \mathbf{T}_{TF} = \mathbf{T}_{CF} + \mathbf{T}_{psF} + \mathbf{T}_{rsF} \\ \mathbf{T}_{FT} = \mathbf{T}_{CT} + \mathbf{T}_{rsT} + \mathbf{T}_{psT} \end{cases} \tag{4.13}$$

By applying equations (4.4), (4.5) and (4.13) to equation (4.2), we can determine the interactive torques $\mathbf{T}_{TF}$ and $\mathbf{T}_{FT}$.

4.3.2 Simplified equations of motion of TP and FP

Through a thorough analysis of the previous section, we derived the full EoMs of the T^3-Multirotor. These equations, however, contain highly non-linear and complex terms, which hinders intuitive understanding of the platform. But for reasons to be discussed in this subsection, most of the non-linear terms of the full EoMs are negligible. Therefore, in this subsection, we introduce a simplified EoMs of the T^3-Multirotor by adopting several assumptions applicable to most of the typical T^3-Multirotor flight.

4.3.2.1 Simplified translational EoMs

From equations (4.1) and (4.5), we can obtain the following equation

$$m_T\ddot{\mathbf{X}}_T + m_F\ddot{\mathbf{X}}_F = \mathbf{R}(\mathbf{q}_T)\mathbf{F}_T + M\mathbf{g}, \tag{4.14}$$

where $M = m_T + m_F$. Now, let us define

$$\ddot{\mathbf{X}}_F = \ddot{\mathbf{X}}_T + \Delta_a, \tag{4.15}$$

where Δ_a is the gap between the acceleration vector of TP and FP. Here, since $\mathbf{r}_T$ and $\mathbf{r}_F$ in equation (5.3) are very small in most cases and $\mathbf{q}_T$ and $\mathbf{q}_F$ have a limited range near zero due to the operation principle of the multirotor, we can assume that $\Delta_a \approx 0$ in most cases. Applying this assumption to equation (4.14), the simplified translational equations of motion of TP and FP become as follows

$$\ddot{\mathbf{X}} \approx \frac{1}{M}\mathbf{R}(\mathbf{q}_T)\mathbf{F}_T + \mathbf{g}, \tag{4.16}$$

where $\ddot{\mathbf{X}} = \ddot{\mathbf{X}}_T, \ddot{\mathbf{X}}_F$.

4.3.2.2　Simplified rotational EoMs

Through the comparison of equations (4.1) and (4.16), we can obtain the interactive force of a universal joint as follows.

$$\mathbf{F}_{FT} = -\left(\frac{m_F}{M}\right) R(\mathbf{q}_T)\mathbf{F}_T \tag{4.17}$$

Applying equations (4.5) and (4.17) to (4.2) , the rotational EoMs of TP and FP become

$$\begin{cases} J_T\ddot{\mathbf{q}}_T = \mathbf{T}_T + \mathbf{T}_{FT} \\ J_F\ddot{\mathbf{q}}_F = \left(\frac{m_F}{M}\right)\left(\mathbf{r}_F \times \left(\mathbf{R}^{-1}(\mathbf{q}_F)\mathbf{R}(\mathbf{q}_T)\mathbf{F}_T\right)\right) + \mathbf{T}_{TF} \end{cases} , \tag{4.18}$$

where we applied the assumptions $\dot{\Omega} \approx \ddot{\mathbf{q}}$ and $\Omega \times J\Omega \approx 0$ that are widely used in the simplification process of rotational dynamics of the multirotors [19, 47, 48]. Then, applying equation (4.13) into equation (4.18) brings the following equation.

$$\begin{cases} J_T\ddot{\mathbf{q}}_T = \begin{bmatrix} \tau_{r,T} \\ \tau_{p,T} \\ \tau_{y,T} \end{bmatrix} + \begin{bmatrix} 1 \\ 0 \\ 0 \end{bmatrix}\tau_{rsT} - \begin{bmatrix} -\sin\theta_r\sin\phi_F \\ \cos\phi_T\cos\phi_F + \sin\phi_T\cos\theta_r\sin\phi_F \\ -\sin\phi_T\cos\phi_F + \cos\phi_T\cos\theta_r\sin\phi_F \end{bmatrix}\tau_{psF} + \begin{bmatrix} 0 \\ \tan\phi_r \\ 1 \end{bmatrix}\tau_{y,CT} \\[3em] J_F\ddot{\mathbf{q}}_F = \frac{m_F r_F}{M}\begin{bmatrix} \cos\phi_F\sin\phi_T - \sin\phi_F\cos\theta_r\cos\phi_T \\ \sin\theta_r\cos\phi_T \\ 0 \end{bmatrix}F_T - \begin{bmatrix} \cos\theta_r \\ -\sin\phi_F\sin\theta_r \\ \cos\phi_F\sin\theta_r \end{bmatrix}\tau_{rsT} + \begin{bmatrix} 0 \\ 1 \\ 0 \end{bmatrix}\tau_{psF} + \begin{bmatrix} \tan\theta_r \\ 0 \\ 1 \end{bmatrix}\tau_{y,CF} \end{cases} \tag{4.19}$$

In a typical multirotor flight except for the rapid vertical acceleration / deceleration, the magnitude of the F_T always remain near hovering thrust (the magnitude of the thrust to make $\ddot{z}_T = 0$). From equation (4.16), we can obtain the hovering thrust $F_{T,h} \in \mathbb{R}$ as follows.

$$F_{T,h} = \frac{Mg}{\cos\phi_T\cos\theta_T} \tag{4.20}$$

Utilizing equation (4.20), we can express the actual thrust force F_T as

$$F_T = F_{T,h} + \Delta_T, \tag{4.21}$$

where $\Delta_T \in \mathbb{R}$ represents the gap between the actual thrust and the hovering thrust, and the value of Δ_T can be assumed to be negligibly small in most typical flight situations.

Next, we investigate the value of $\tau_{y,CT}$ and $\tau_{y,CF}$. Applying the small angle assumption to ϕ_* and θ_* of the yaw EoM in equation (4.19), the equations can be written as

$$\begin{cases} J_{3,T}\ddot{\psi}_T \approx \tau_{y,T} + \phi_r \tau_{psF} + \tau_{y,CT} \\ J_{3,F}\ddot{\psi}_F \approx -\theta_r \tau_{rsT} + \tau_{y,CF} \end{cases}. \tag{4.22}$$

When we apply equations (4.4) and (4.10) into (4.22), then the value of $\tau_{y,CT}$ can be described as follows.

$$\tau_{y,CT} \approx -\frac{J_{3,F}\tau_{y,T} + J_{3,T}\theta_r \tau_{rsT} + J_{3,F}\phi_r \tau_{psF}}{J_{3,F} + J_{3,T}\frac{\cos \theta_r}{\cos \phi_r}} \tag{4.23}$$

Considering that relative attitudes have a small value near zero, $\tau_{y,CT}$ can be rewritten as

$$\tau_{y,CT} = -\frac{J_{3,F}}{J_{3,F} + J_{3,T}}\tau_{y,T} + \Delta_Y, \tag{4.24}$$

where $\Delta_Y \in \mathbb{R}$ represents the residual values that are not expressed in equation (4.24) among the values of equation (4.23).

If we apply equations (4.21) and (4.24) to (4.19) with assuming that $\Delta_T \approx 0$ and $\Delta_Y \approx 0$, then the final form of the simplified attitude EoM becomes

$$\begin{cases} J_T \ddot{\mathbf{q}}_T \approx \begin{bmatrix} \tau_{r,T} \\ \tau_{p,T} \\ \tau_{y,T} \end{bmatrix} + \begin{bmatrix} 1 \\ 0 \\ 0 \end{bmatrix}\tau_{rsT} - \begin{bmatrix} 0 \\ 1 \\ -\phi_r \end{bmatrix}\tau_{psF} + \begin{bmatrix} 0 \\ \phi_r \\ 1 \end{bmatrix}\tau_{y,CT} = \mathbf{T}_T + \mathbf{T}_{rsT} - \mathbf{T}_{psF} - \begin{bmatrix} 0 \\ 0 \\ \frac{J_{3,F}}{J_{3,T}+J_{3,F}} \end{bmatrix}\tau_{y,T} + \boldsymbol{\Delta}_{res,T} \\[3em] J_F \ddot{\mathbf{q}}_F \approx K\begin{bmatrix} \phi_r \\ \theta_r \\ 0 \end{bmatrix} - \begin{bmatrix} 1 \\ 0 \\ \theta_r \end{bmatrix}\tau_{rsT} + \begin{bmatrix} 0 \\ 1 \\ 0 \end{bmatrix}\tau_{psF} + \begin{bmatrix} \theta_r \\ 0 \\ 1 \end{bmatrix}\tau_{y,CF} = K\begin{bmatrix} \phi_r \\ \theta_r \\ 0 \end{bmatrix} - \mathbf{T}_{rsT} + \mathbf{T}_{psF} + \begin{bmatrix} 0 \\ 0 \\ \frac{J_{3,F}}{J_{3,T}+J_{3,F}} \end{bmatrix}\tau_{y,T} + \boldsymbol{\Delta}_{res,F} \end{cases}, \tag{4.25}$$

where $K = m_F r_F g$. The symbol $\boldsymbol{\Delta}_{res,*} = [d_{1,*} \ d_{2,*} \ d_{3,*}]^T \in \mathbb{R}^{3\times 1}$ represents a residual term of each equation, which remains small throughout the flight.

4.4 Controller design

From the system model derived in the previous section, we can find that the T^3-Multirotor has six independent control inputs of $\tau_{r,T}$, $\tau_{p,T}$, $\tau_{y,T}$, τ_{rsT}, τ_{psF} and F_T (refer equations (4.16) and (4.25)). Thus, with the fact that the number of independent control inputs matches the number of DOF of the platform, we can confirm that the platform is a fully-actuated system. Based on this result, in this section, we design a dedicated controller to implement the 6-DOF motion performance of the FP.

4.4.1   Controller overview

Fig. 4.2 shows an overview of the proposed control algorithm. The controller is divided into a translational motion controller (TMC) module and a rotational motion controller (RMC) module. The TMC module controls the position $\mathbf{X}$ of the platform, while the RMC module controls the $\mathbf{q}_F$, which is the attitude of the FP.

4.4.1.1   TMC module

The TMC module generates the $\tau_{r,T}$, $\tau_{p,T}$ and F_T signals to control the direction and magnitude of the collective thrust vector generated by the unidirectionally aligned thrusters of the TP. The signals are then combined with external signal $\tau_{y,T}$ to form the $\mathbf{U}_T = [\tau_{r,T} \; \tau_{p,T} \; \tau_{y,T} \; F_T]^T \in \mathbb{R}^{3 \times 1}$ signal. By the predefined relationship [47], $\mathbf{U}_T$ signal is converted to $\mathbf{U}_M = [F_1 \; F_2 \; \cdots \; F_n]^T \in \mathbb{R}^{n \times 1}$ signal, which is a set of target force signal of each thruster, and applied to each motor of TP. The value n represents the number of thrusters.

4.4.1.2   RMC module

The roll and pitch attitude of the FP are mainly controlled by the servomechanisms. Thus, the τ_{rsT} and τ_{psF} signals are generated through the dedicated relative roll and pitch attitude controller configured inside the RMC module, and applied directly to RSM and PSM.
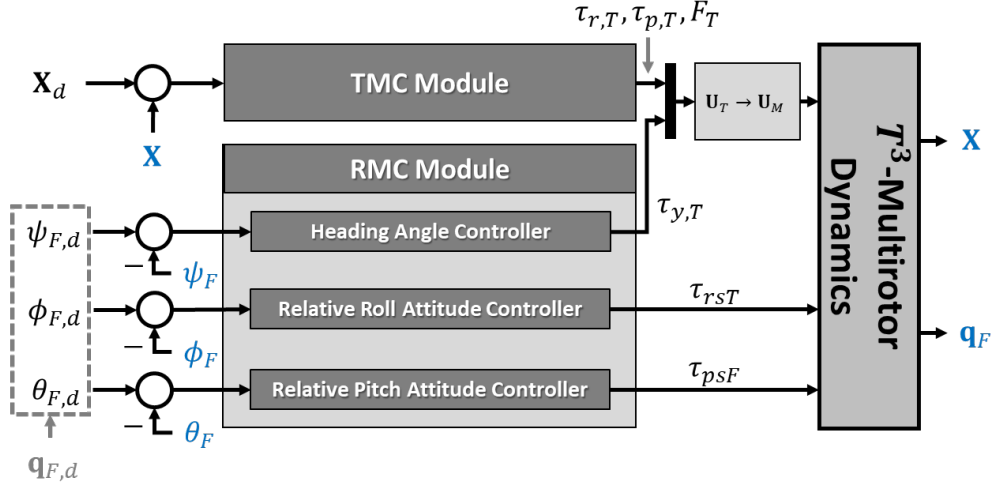
Figure 4.2: Overall structure of 6-DOF controller of T^3-Multirotor. The blue signals are the feedback signals, which are measured through the sensor.

However, unlike other components of the $\mathbf{q}_F$, the heading angle ψ_F $(= \psi_T)$ is controlled through the set of thrusters of the TP. Therefore, an independent heading angle controller is constructed to generate the $\tau_{y,T}$ signal, which is then merged into the $\mathbf{U}_T$ signal.

In order to implement the proposed controller structure, the attitude of TP and FP must be controlled independently. However, the rotational dynamics of TP and FP are coupled to each other by the relationship of equation (4.25). Therefore, we first need to devise a way to overcome the motion coupling between the two parts. In the following subsection, we describe the detailed structure of attitude controller to overcome the motion coupling problem.

4.4.2 Independent roll and pitch attitude control of TP and FP

Fig. 4.3 is a block diagram of the roll dynamics among the results of equation (4.25). The symbols $d_{1,T} \in \mathbb{R}$ and $d_{1,F} \in \mathbb{R}$ in the figure represent unknown external disturbances that can be applied to the roll EoM of TP and FP. For roll dynamics, TP and FP dynamics are coupled due to the exchange of τ_{rsT} and $K\phi_r$ signal. However, the primary control input of the attitude ϕ_T is $\tau_{r,T}$ as the conventional multirotor, and ϕ_F is mainly controlled by

50
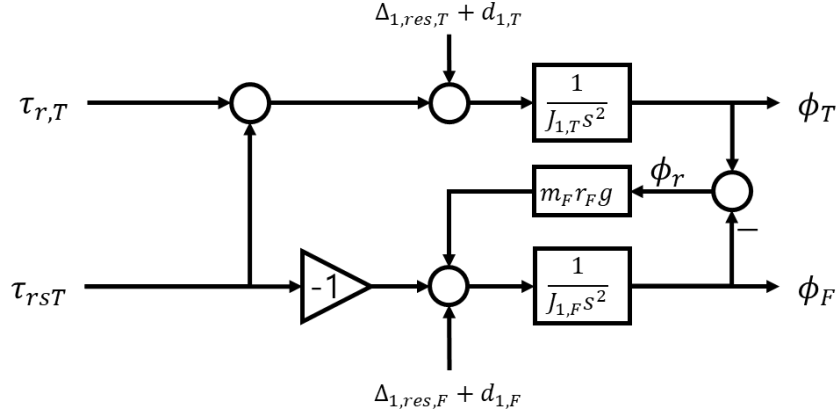
Figure 4.3: Block diagram of the simplified roll dynamics of equation (4.25). Motion coupling occurs between TP and FP dynamics due to roll servo torque and relative roll attitude.

τ_{rsT}, which is the only control input of the FP. Therefore, one can reorganize the system shown in Fig. 4.3 as Fig. 4.4, by treating TP and FP attitude dynamics as two decoupled systems with various sources of disturbances. In this case, each channel treats all system inputs except $\tau_{r,T}$ and τ_{rsT} respectively as undesired external inputs.

In the approach shown in Fig. 4.4, the τ_{rsT} and $K\phi_r$ signals can be treated as major disturbances applied to TP and FP, respectively. Therefore, we can consider canceling τ_{rsT} and $K\phi_r$ signal in each channel directly by subtracting those signals from the control inputs $\tau_{r,T}$ and τ_{rsT}. However, measuring the exact servomotor torque for signal compensation in an actual environment is impractical, and it is also difficult to know the accurate $K(= r_F m_F g)$ value if such unknown external payload (ex. sensor, cargo) is attached to the FP. Moreover, residual terms and disturbances in each channel cannot be overcome in this approach.

As an alternative, the Disturbance Observer (DOB) robust control algorithm is applied as shown in Fig. 4.5. Introduced by Onishi et. al [49], the DOB robust control algorithm has been applied to many multirotor studies, allowing the system to maintain nominal flight performance even when unknown disturbances are applied to the system. The capability of the DOB in maintaining the nominal performance is achieved by estimating and canceling external input signals other than the control input [50–52]. Therefore, by applying the DOB control structure to the TP and FP channels in Fig. 4.4 respectively, we can expect
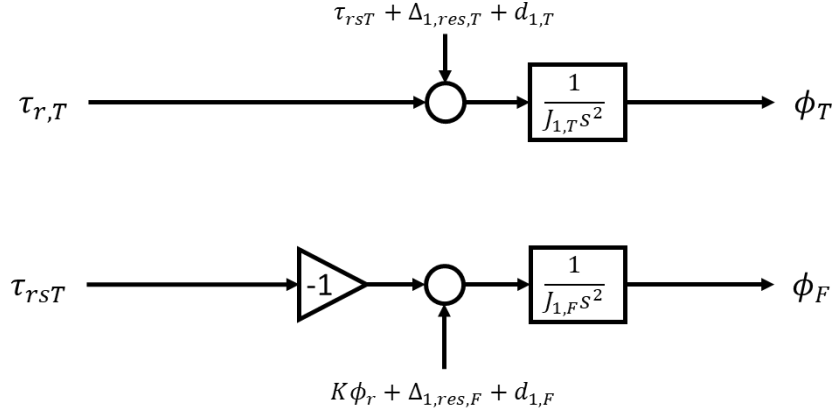
Figure 4.4: Simplified roll dynamics of equation (4.25) after treating the coupling terms as external disturbances of TP and FP, respectively. In this case, we can treat the dynamics of TP and FP as two independent systems.

to cancel the effect of the remaining signals except for the control inputs ($\tau_{r,T}$ and τ_{rsT}) of each channel. This allows us to compensate not only the coupling terms but also the residual and actual disturbance terms of each channel, resulting in the high-level of decoupling of TP and FP dynamics and maintaining the nominal flight performance.

Fig. 4.5 shows the controller architecture of the TP and FP with the DOB algorithm applied. In the figure, the sum of the external signals of each part is expressed as $D_{1,T} \in \mathbb{R}$ and $D_{1,F} \in \mathbb{R}$, respectively. The operating principle of DOB is to estimate those $D_{1,T}$ and $D_{1,F}$, and then to compensate the disturbances by applying the corresponding estimate in the next control step. As shown in Fig. 4.5, the transfer function of the TP roll motion is $\frac{1}{J_{1,T}s^2}$ (derived from equation (4.25)). Therefore, we can estimate the final input signal $\alpha_{r,T}$ through the nominal model inverse $\bar{J}_{1,T}s^2$ as $\hat{\alpha}_{r,T}$, where $\hat{*}$ represents the estimated quantity and $\bar{*}$ represents the nominal quantity throughout this chapter.

However, since the transfer function $\bar{J}_{1,T}s^2$ is an improper transfer function, the estimation process cannot be realized. Instead, we add a transfer function called Q-filter to the existing block to make the $\hat{\alpha}_{r,T}$ estimation block proper ($Q_{r,T}\bar{J}_{1,T}s^2$ block of Fig. 4.5). We aimed to make the relative degree of the estimation block to 1, and the third-order
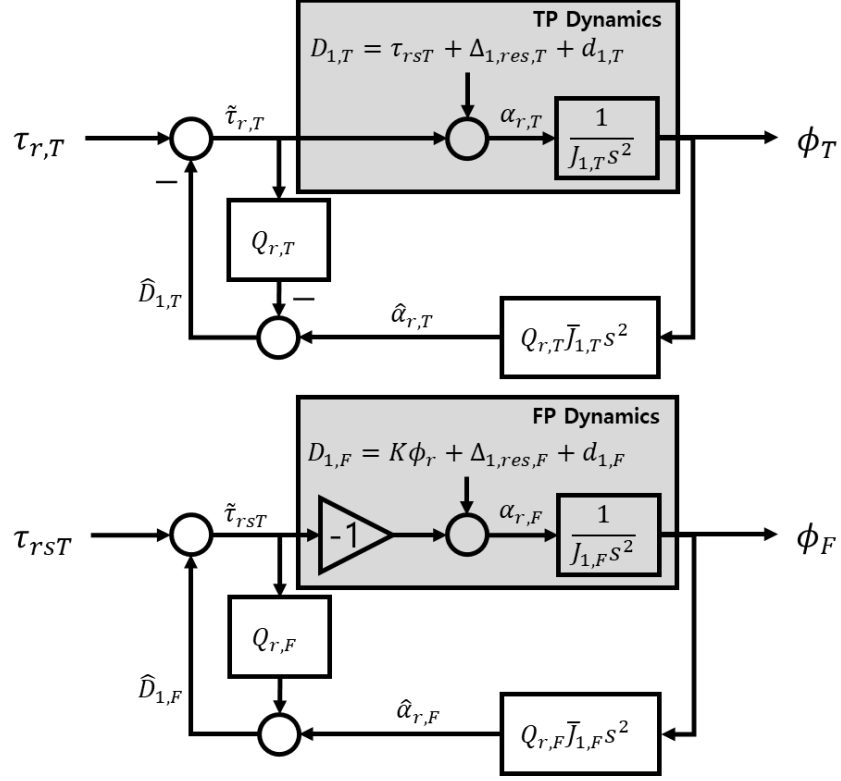
Figure 4.5: Simplified roll dynamics with DOB robust control algorithm for roll motion decoupling between TP and FP dynamics.

Butterworth filter with

$$Q_{r,T} = \frac{1}{\left(\frac{s}{f_{r,T}} + 1\right)\left(\left(\frac{s}{f_{r,T}}\right)^2 + \frac{s}{f_{r,T}} + 1\right)} \tag{4.26}$$

is chosen as the Q-filter to preserve the magnitude response of the nominal model inverse until the designated cutoff frequency $f_{r,T}$.

Since $\alpha_{r,T}$ is the sum of the two components as in the following equation

$$\alpha_{r,T} = \tilde{\tau}_{r,T} + D_{1,T}, \tag{4.27}$$

we can obtain the estimated disturbance $\hat{D}_{1,T}$ from the comparison between $\hat{\alpha}_{r,T}$ and the actual control input $\tilde{\tau}_{r,T}$. During the comparison process, the $\tilde{\tau}_{r,T}$ signal also passes through

the $Q_{r,T}$ filter for phase synchronization with the $\hat{\alpha}_{r,T}$ signal. In final, the $\hat{D}_{1,T}$ signal is combined with $\tau_{r,T}$ to become

$$\tilde{\tau}_{r,T} = \tau_{r,T} - \hat{D}_{1,T}, \tag{4.28}$$

from which $\alpha_{r,T}$ in equation (4.27) becomes as

$$\alpha_{r,T} = \tilde{\tau}_{r,T} + D_{1,T} = \tau_{r,T} + (D_{1,T} - \hat{D}_{1,T}) \approx \tau_{r,T}$$

and the disturbance is canceled. As shown in Fig. 4.5, DOB applies equally to FP, and also the pitch dynamics of TP and FP.

4.4.3 Heading angle control

By ignoring the residual terms in equation (4.25) which remains a small values in a general flight situation, the simplified yaw EoMs of TP and FP can be written as follows.

$$\begin{cases} J_{T,3}\ddot{\psi}_T = \tau_{y,T} - \frac{J_{3,F}}{J_{3,T}+J_{3,F}}\tau_{y,T} \\ J_{F,3}\ddot{\psi}_F = \frac{J_{3,F}}{J_{3,T}+J_{3,F}}\tau_{y,T} \end{cases} \tag{4.29}$$

When we apply equation (4.4) to the above equations, the yaw EoM becomes follows.

$$(J_{T,3} + J_{F,3})\ddot{\psi}_T = \tau_{y,T}, \quad \ddot{\psi}_T = \ddot{\psi}_F \tag{4.30}$$

Based on this result, we can treat the yaw dynamics as an independent system. Therefore, we control the yaw motion by constructiong an independent heading angle controller in the same way as the conventional yaw motion control method of a multirotor [47].

4.4.4 Overall control scheme

Fig. 4.6 shows the overall control scheme including the detailed structure of TMC and RMC.
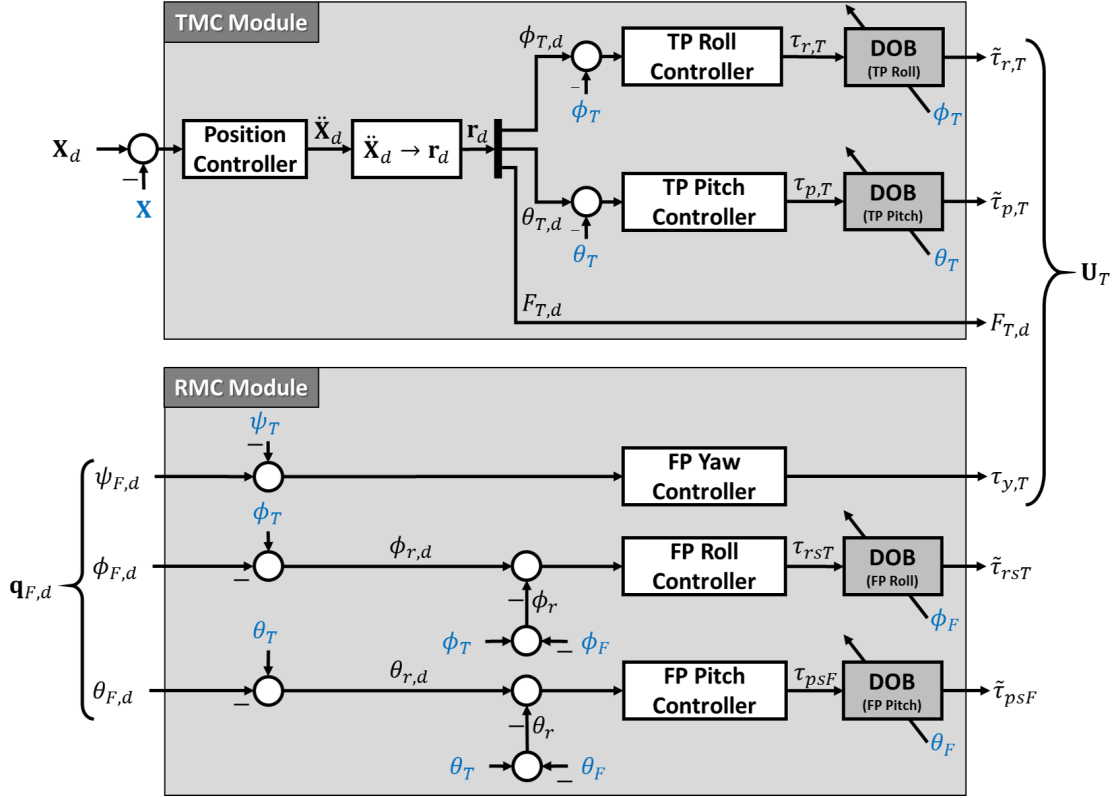
Figure 4.6: Configuration diagram of T^3-Multirotor control algorithm. The blue signals are collected via the sensor as feedback signals.

For TMC module, a cascaded control structure is adopted. First, the position controller generates $\ddot{\mathbf{X}}_d$ the desired translational acceleration command. Then, $[\ddot{\mathbf{X}}_d \rightarrow \mathbf{r}_d]$ block changes $\ddot{\mathbf{X}}_d$ signal into a $\mathbf{r}_d = [\phi_{T,d}\ \theta_{T,d}\ F_{T,d}]^T \in \mathbb{R}^{3 \times 1}$ signal (refer [53] for signal conversion process). Among the components of the $\mathbf{r}_d$ signal, the $\phi_{T,d}$ and $\theta_{T,d}$ signals pass through the feedback attitude controller to become the $\tau_{r,T}$ and $\tau_{p,T}$ signals. Later, those two torque commands are modified as $\tilde{\tau}_{*,T}$ signal through a disturbance compensation process using the DOB algorithm as shown in Fig. 4.5.

For RMC module, three independent controllers are configured for FP attitude control. In case of the heading angle control, an independent feedback FP yaw controller corresponding to the yaw dynamics of equation (4.29) is constructed to generate the $\tau_{y,T}$ signal. For roll and pitch control, the target relative attitude signal is first generated as in the

following equation.

$$(*)_{r,d} = (*)_T - (*)_{F,d} \qquad (4.31)$$

Then, the feedback FP roll and pitch controller generates the τ_{rsT} and τ_{psF} signal. Later, the two signals are modified to $\tilde{\tau}_{rsT}$ and $\tilde{\tau}_{psF}$ by passing through the DOB algorithm as shown in Fig. 4.5.

4.5 Simulation result

The simulation of T^3-Multirotor is conducted to validate the 6-DOF flight performance of the proposed control algorithm. [1] The simulation proceeds in two different flight scenarios:

- Scenario 1: Changing FP attitude during hovering,

- Scenario 2: Fixing FP attitude during translation,

each of which is designed to demonstrate the independence of translational and rotational motion of the T^3-Multirotor.

The first scenario focuses on validating the independent attitude control performance of the TP (independent translational motion control performance) for the attitude motion of the FP, and additionally validates the reference trajectory tracking performance of the FP attitude. If independent attitude control of the TP is not guaranteed in this scenario, unwanted translational motion occurs due to the relationship of equation (4.1).

In converse, the second scenario focuses on validating the control independence of the FP attitude for the attitude motion of the TP, and additionally validates the reference trajectory tracking performance of the TP. If the independent attitude control of the FP is not guaranteed in this scenario, the FP attitude continuously changes without having a constant value in accordance of the attitude change of the TP.

---

[1] T^3-Multirotor simulator with motion visualization tool is available at `https://www.sjlazza.com/research-blog/matlab-t3-multirotor-simulator`.

Table 4.1: Physical parameters and controller gains

TP Parameter	Value	FP Parameter	Value
m_T	1 Kg	m_F	2 Kg
r_T	0.03 m	r_F	-0.1 m
$J_{1,T}, J_{2,T}$	0.01 Kg m^2	$J_{1,F}, J_{2,F}$	0.01 Kg m^2
$J_{3,T}$	0.1 Kg m^2	$J_{3,T}$	0.1 Kg m^2
Controller Gain	Value	Controller Gain	Value
P (TP Roll, Pitch)	3	P (FP Roll, Pitch)	3
D (TP Roll, Pitch)	1	D (FP Roll, Pitch)	1
P (X, Y Position)	3	P (Z Position)	3
I (X, Y Position)	1	I (Z Position)	1
D (X, Y Position)	3	D (Z Position)	1
P (Heading Angle)	3	f_{cutoff} (TP DOB)	30 Hz
D (Heading Angle)	1	f_{cutoff} (FP DOB)	30 Hz

The parameters of the dynamic system model constructed for the simulation and the gain values used in the controller are shown in Table 4.1. To confirm the improvement of 6-DOF control performance due to the application of the DOB algorithm, flight performance of the 'No-DOB' and 'With-DOB' situation is compared in each scenario. In the 'No-DOB' situation, the disturbance compensation signal $\hat{D}_*$ of all channels including the roll channel of equation (4.28) does not apply to the final control input, resulting in the following relationship

$$\tilde{\tau}_* = \tau_*$$

holds for all DOB-applied channels in Fig. 4.6. On the other hand, in the 'With-DOB' situation, the disturbance compensation signal is incorporated into the $\tilde{\tau}_*$ signal, making

$$\tilde{\tau}_* = \tau_* - \hat{D}_*$$

relationship holds.

4.5.1 Scenario 1: Changing FP attitude during hovering

The left set of figures in Fig. 4.7 shows the flight result of Scenario 1. In this scenario, a sinusoidal reference attitude of 1.5 rad/s is applied to ϕ_F and θ_F while $\mathbf{X}_d$ is fixed at the origin.

In the 'No-DOB' situation, we can see that the attitude of the TP which should have a fixed attitude to attain the hovering goal continuously oscillates. As a result, the position of the T^3-Multirotor also continued to oscillate in the absence of DOB algorithm. Furthermore, we can also confirm that neither TP and FP has shown a satisfactory reference trajectory tracking performance. However, in the 'With-DOB' situation, the reference translational motion-tracking performance of the TP is greatly improved by the effective cancellation of the reaction torque applied from the FP. Also, the FP showed a highly improved reference attitude-tracking performance compared to the 'No-DOB' situation.

4.5.2 Scenario 2: Fixing FP attitude during translation

The right set of figures in Fig. 4.7 shows the flight result of Scenario 2. In the second scenario, a sinusoidal reference position of 1.5 rad/s is applied to $x_{T,d}$ ($= x_{F,d}$) and $y_{T,d}$ ($= y_{F,d}$) while $\phi_{F,d}$ and $\theta_{F,d}$ are fixed to zero throughout the flight.

Simulation results show no significant difference in position tracking performance between 'No-DOB' and 'With-DOB' cases. However, in the case of 'No-DOB', a large overshoot is found in TP attitude due to the reaction torque and the FP also continuously vibrates without the fixed attitude due to the same reason. On the other hand, in the 'With-DOB' case, both TP and FP followed the reference attitude fairly accurate.
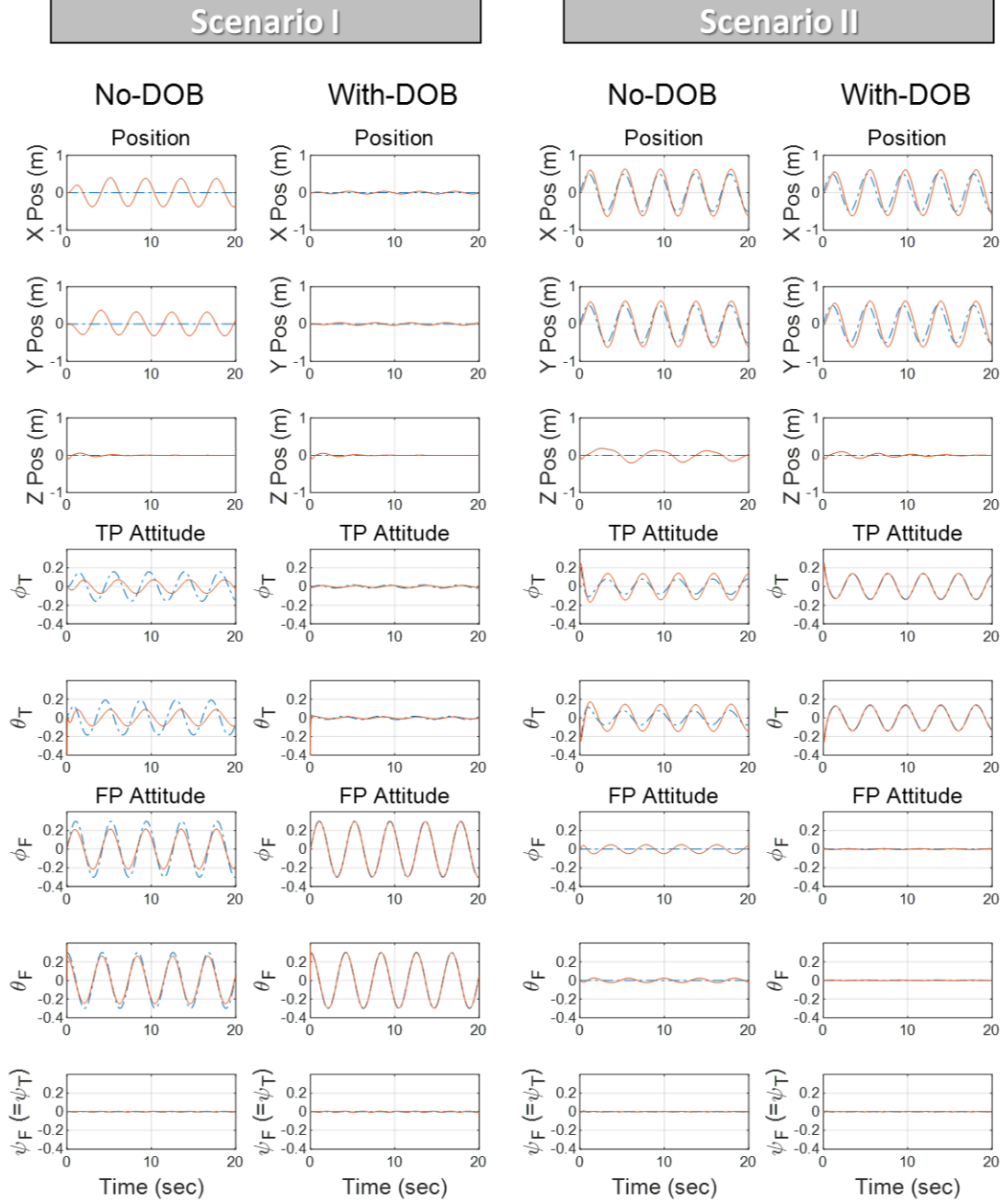
Figure 4.7: [SIMULATION RESULTS] Comparison of flight performance according to the application of DOB in Scenario 1 (left) and 2 (right). The blue dash line represents the reference trajectory, and the red solid line represents the tracking result.

4.6 Experimental result

For validating 6-DOF control performance in an actual environment, the same two scenarios as simulations are performed as actual experiments. However, unlike the simulation, arbitrary reference signals are applied in this case to validate the stable flight performance of the platform for control inputs with various frequency. The physical quantities of the platform and the controller gains used in the actual experiment have the values shown in Table 4.1 as in the simulation.

4.6.1 Scenario 1: Changing FP attitude during hovering

The set of figures on the left side of Fig. 4.8 shows the flight results for 'No-DOB' and 'With-DOB' conditions in Scenario 1. During the flight, hovering is performed at an altitude of about 0.8 m by fixing x_d and y_d as the origin. Then, $\phi_{F,d}$ and $\theta_{F,d}$ values of arbitrary amplitude and frequency are generated by the human-controlled r/c controller and applied to the system. When DOB is not applied, we can see that the position of the platform changes in accordance with the attitude variation of the FP. Especially, the position change in the X direction depends on the variation of θ_F, and the Y-direction depends on the variation of the ϕ_F attitude. Also, the reference trajectory tracking performance was insufficient for both TP and FP. Meanwhile, after applying DOB, we can see that the position is well maintained even though the arbitrary ϕ_F and θ_F are applied. In addition, the attitude tracking performance of TP and FP is also improved greatly.

4.6.2 Scenario 2: Fixing FP attitude during translation

The set of figures on the right side of Fig. 4.8 shows the flight results of Scenario 2. During the flight, $\phi_{T,d}$ and $\theta_{T,d}$ signals with arbitrary amplitude and frequency are applied to the system in the same way as Scenario 1, while the altitude is controlled autonomously via the feedback height controller. First, in FP attitude control, stable attitude leveling

is achieved in both cases of 'No-DOB' and 'With-DOB'. However, in the case of the TP attitude control, we can see that a very large overshoot in the 'No-DOB' condition. But after DOB is applied, the TP accurately followed the target attitude trajectory.
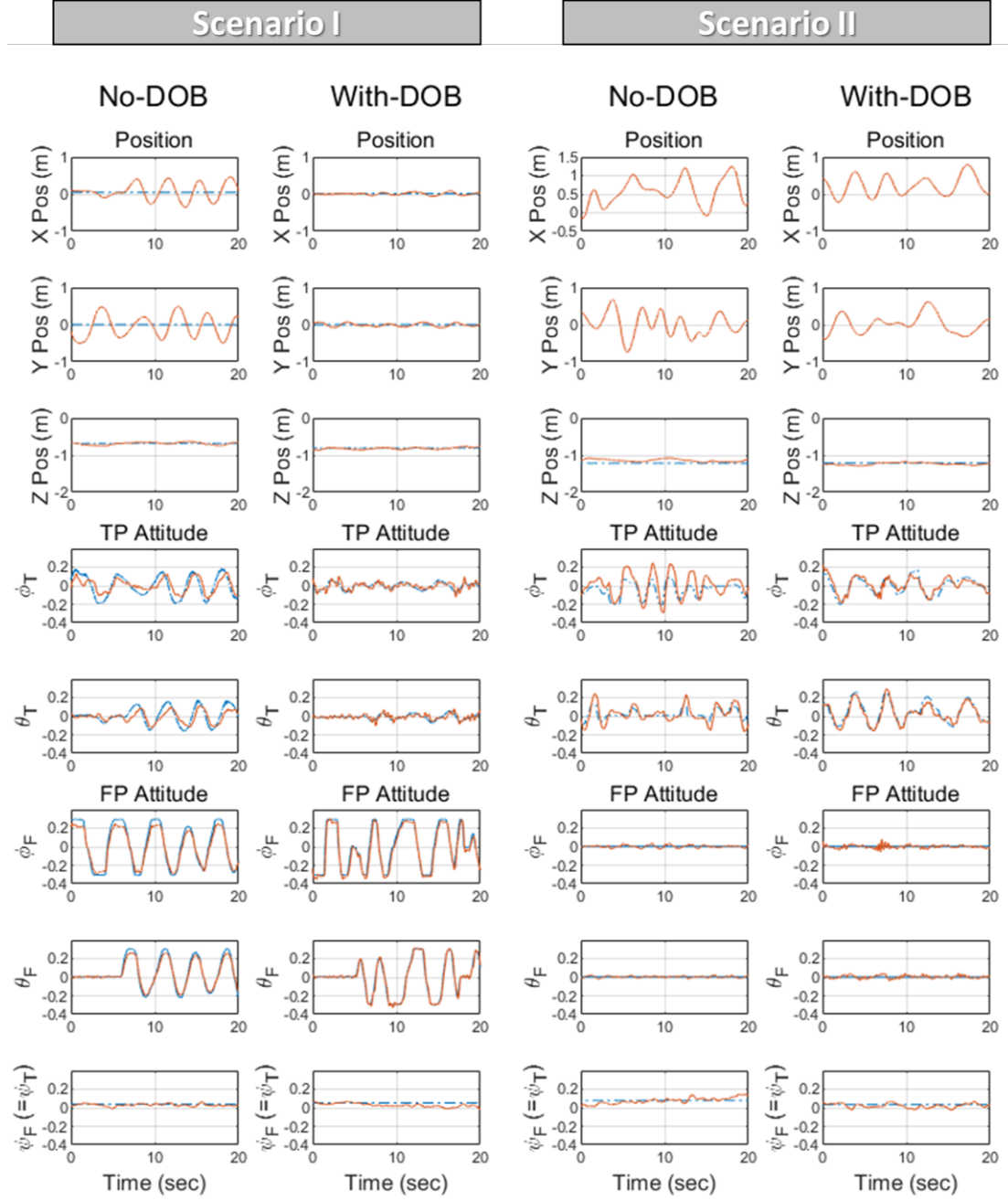
Figure 4.8: [EXPERIMENTAL RESULTS] Comparison of flight performance according to the application of DOB in Scenario 1 (left) and 2 (right). The blue dash line represents the reference trajectory, and the red solid line represents the tracking result.

4.7 Applications

Through sections V and VI, we have confirmed the 6-DOF flight performance of the T^3-Multirotor. However, the utility of 6-DOF flight in multirotor-based engineering applications has not been demonstrated. Therefore in this section, we introduce several flight examples that utilize T^3-Multirotor to achieve flight goal where conventional multirotor platforms cannot perform.

4.7.1 Personal aerial vehicle

The ability of FP to maintain a constant attitude shown in Fig. 1.2 and scenario II of Fig. 4.7 and 4.8 can be useful in the personal aerial vehicle (or air-taxi) flight. According to [54], numerous eVTOL aircraft that are regarded as aerial mobility platforms have the form-factor of a multirotor. However, since the attitude of a multirotor always changes to control the translational motion, the occupant must experience constant attitude change in addition to the translational acceleration at all times, which can cause motion sickness or significant reduction in riding comfort. By introducing the T^3-Multirotor mechanism and keeping the FP attitude constant, passengers can experience only the translational acceleration, thus enabling a pleasant flight experience.

4.7.2 High MoI payload transportation platform - revisit of [1]

In multirotor-based aerial cargo transportation, cargo is usually tightly fixed to the fuselage. In this case, tightened cargo rotates with the fuselage during the attitude control for translational motion. If the MOI of cargo is very large (e.g. bar, box with a large volume), the rotational dynamics of the platform changes significantly, resulting in a large change in attitude control performance. This can lead to a decline in flight control performance and, if severe, to unstable flight.

However, by using T^3-Multirotor, it is possible to keep a constant attitude of cargo-
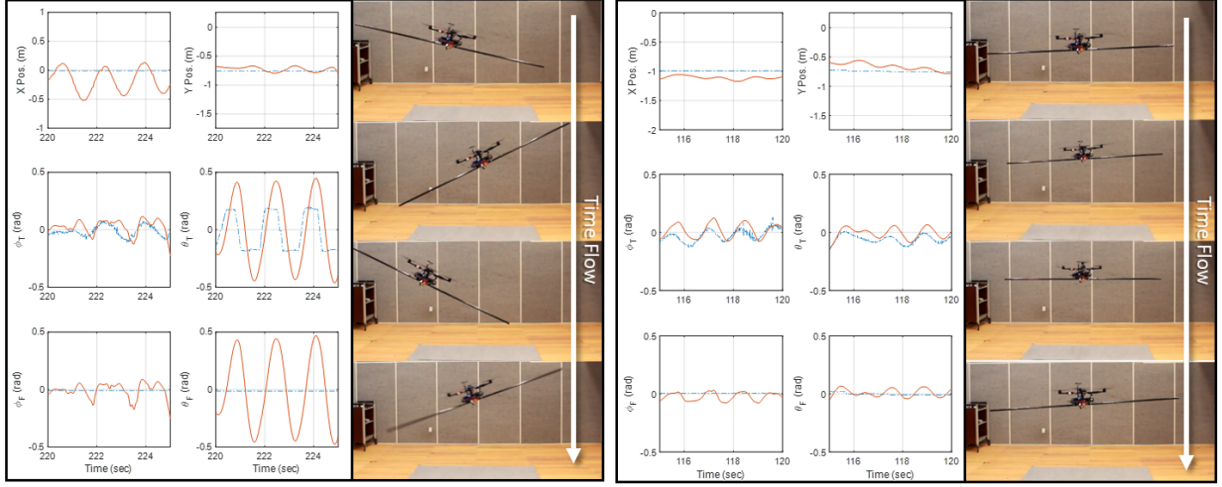
Figure 4.9: Flight results with attaching a rod with a length of 2 m and a mass of 430 g (0.1433 Kg·m² of rod MoI) to the FP along pitch axis. The blue dash line represents the reference trajectory, and the red solid line represents the tracking result. [**TOP**] Flight results in the situation where $\phi_r, \theta_r = 0$, same as general multirotor. [**BOTTOM**] Flight results with $\phi_{F,d}, \theta_{F,d} = 0$.

attached FP during the flight. This method ensures that the TP, which is responsible for translational motion, does not have to rotate the cargo and thus ensuring well-regulated translational motion control performance. Fig. 4.9 shows a flight example in which a bar-shaped cargo with a large MoI is transported stably using a T^3-Multirotor. The top set of figures shows the result of flying the cargo on the FP with the relative attitude to zero ($\mathbf{q}_T = \mathbf{q}_F$), as in a conventional multirotor. In this case, we can see that a large overshoot occurs in the control of the specific attitude channel due to the large MoI of the cargo, also bringing the positional oscillation. However, we can see that stable flight is achieved in the bottom set of figures, by utilizing the servomechanism to keep the FP attitude constant ($\mathbf{q}_{F,d} = 0$).

4.7.3 Take-off and landing on an oscillating landing pad

The T^3-Multirotor is capable of landing/take-off on a landing pad where position and attitude changes simultaneously (e.g. landing pad of maritime vessel) by utilizing the advantage
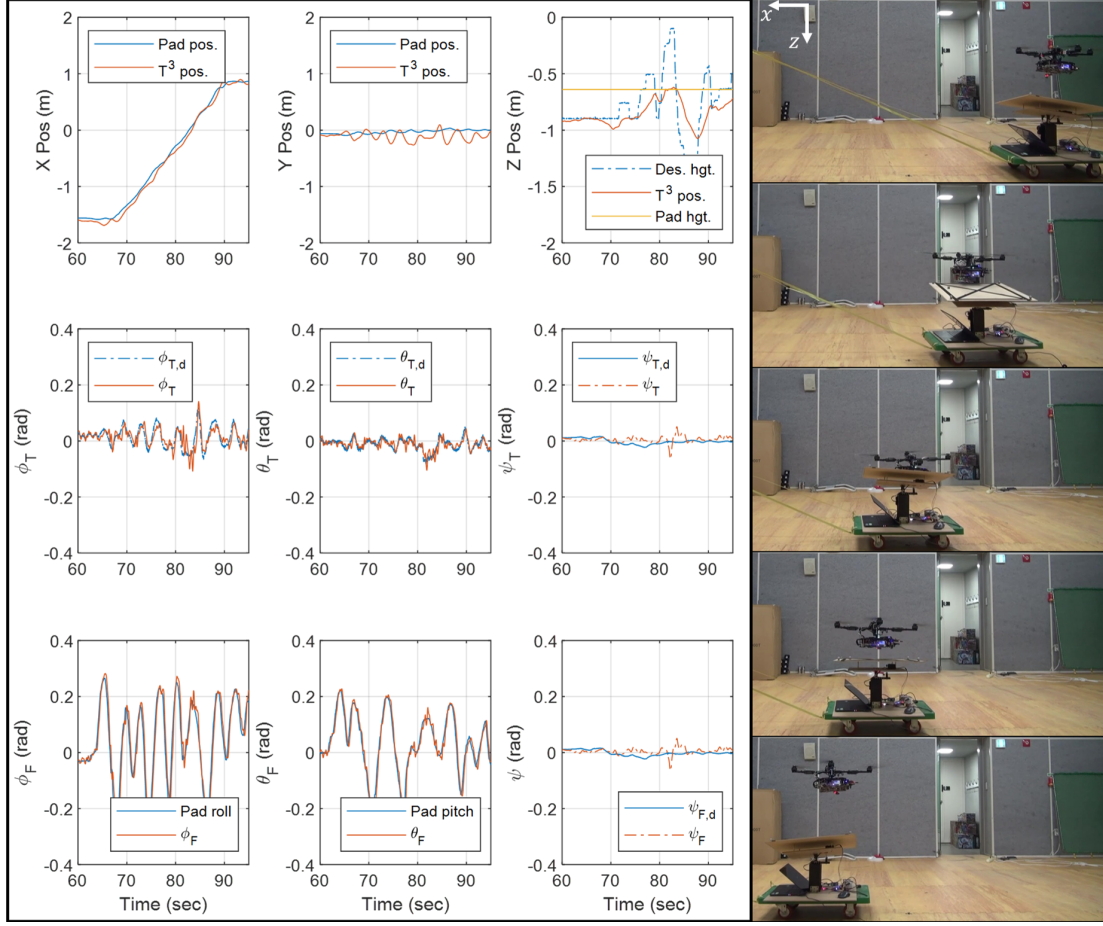
Figure 4.10: Experimental result of landing and re-take-off on a landing pad where position and attitude change simultaneously. The landing pad position is set to the target position $\mathbf{X}_d$ of the TMC module, and the landing pad attitude is set to the target attitude $\mathbf{q}_{F,d}$ of the RMC module.

of platform's independent translational and attitudinal motion control.

In the case of ships, for example, the attitude of the vessel can constantly change due to the ocean waves during seafaring. The conventional multirotor cannot maintain a parallel attitude to the wobbling landing pad for safe and stable landing while flying along the vessel, because the attitude is determined by the position controller. However, the T^3-Multirotor allows stable take-off/landing by controlling the FP attitude parallel to the landing pad while tracking the position of the landing pad through TP attitude/thrust control.

Experiment is conducted to validate the stable landing/re-take-off capability of the

T^3-Multirotor. As shown in Fig. 4.10, a landing pad with constantly changing attitude is introduced for the experiment. During the experiment, the landing pad moves in the X-direction of the earth-fixed frame with arbitrary attitude change. Then, the current position and attitude of the landing pad are respectively applied as the target position $\mathbf{X}_d$ and the target FP attitude $\mathbf{q}_{F,d}$ of the T^3-Multirotor. With proper height control, the T^3-Multirotor touches down on the landing pad and takes-off soon afterward.

Fig. 4.10 shows the position and attitude tracking results of the ship deck landing pad.

4.7.3.1   Position tracking

The position graphs (the top row) show the tracking results of applying the current position of the landing pad as the target position of the T^3-Multirotor, and we can see that the platform stably and accurately followed the pad's position. During the flight, the target altitude is controlled by the operator, and the descent started from 70 seconds, touched down from 80 seconds to 4 seconds, and took off again.

4.7.3.2   TP attitude tracking

The TP attitude graphs (the middle row) show the attitude control results of the TP that are dependent on the translational position control. Even in the touchdown of 80 to 84 seconds, the TP tracked the target TP attitude in a stable and accurate manner.

4.7.3.3   FP attitude tracking

The FP attitude graphs (the bottom row) show the tracking results of applying the attitude of the landing pad as the target FP attitude, and we can confirm that the FP stably followed the pad attitude within the entire flight.

From the experimental results, we confirmed that the platform can always maintain the FP attitude in parallel with the landing pad even during the position tracking, thus ensuring safe landing/take-off at all times.

5

Derived Research:

Fail-safe Flight

in a Single Motor Failure Scenario

5.1 Introduction

Multi-rotor UAVs (hereafter called 'multirotors') have various fuselage shapes depending on the number of thrusters (e.g. quad-, hexa-, octo-copters), but they all share the same principle of controlling flight through four control inputs: roll, pitch yaw torque and overall thrust [3]. Since the number of control inputs is four, multirotors generally require at least four thrusters, and severe problems with stable flight can occur if the number of available thrusters is reduced to less than four [55]. From this fact we can see that the quadcopter configuration with four thrusters is the minimum requirement for a stable multirotor flight, and it is highly difficult to maintain a stable flight if one or more thrusters fail.

Despite these difficulties, however, several methods have been studied to overcome the

flight failure in a motor failure situation.

5.1.1 Related works

Representative studies on emergency flights include [55]$\sim$ [56]. For multirotors with more than four thrusters [57]$\sim$ [56], the platform's redundancy in the actuator is applied to recover full advantage of multirotor flight. In the case of quadcopters, however, one or more controllable degrees of freedom (c-DOF) must be given up depending on the number of the failed motor because the number of actuators available in the event of motor failure is less than four. As a result, quadcopter-based fail-safe flight commonly gives up yaw motion instead of maintaining full control of three-dimensional translational motion [55]$\sim$ [58]. This approach prevents the crash and guarantees safe return/land, but causes continuous rotation of the fuselage with payloads or sensors. Therefore, this approach could cause difficulties for multirotor to carry out designated missions after the failure. Also, for multirotor flights utilizing visual odometry data, continuous camera rotation could drastically deteriorate the quality of the sensor data and result in unstable flight.

To solve this yaw rotation problem, the research of [59] adopted a tilt-rotor-type quadrotor platform with eight c-DOFs. In this case, both translational and yaw motion can be controlled even with the quadrotor configuration. However, this method has the disadvantage of increasing the weight and power consumption, since the servomotor must be installed on each and every thruster for fail-safe flight.

5.1.2 Contributions

In order to solve the problems of previous fail-safe flight, in this chapter, we introduce a new quadcopter fail-safe flight method utilizing the modified T^3-Multirotor (the platform in Fig. 5.1). First introduced in [60] and [1], the T^3-Multirotor platform is a fully-actuated quadcopter platform with fixed thrust direction developed to overcome the dependence of fuselage attitude on translational motion control. With unique mechanical features of the
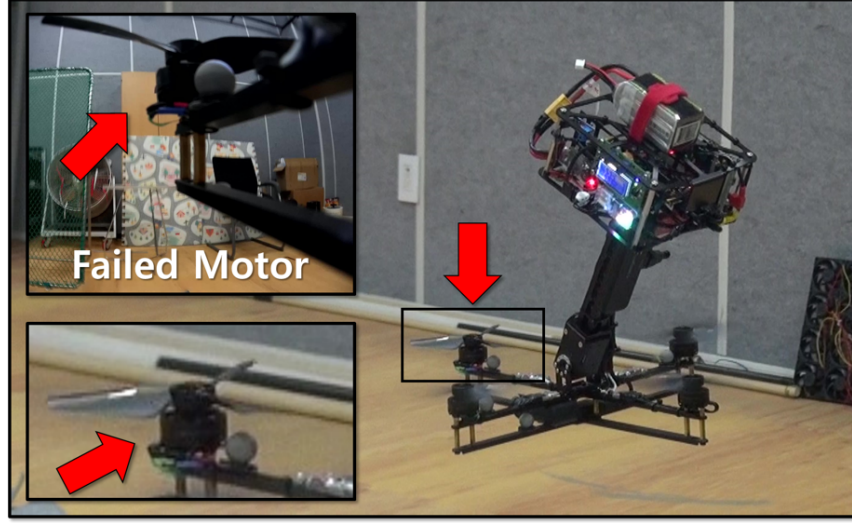
Figure 5.1: The fail-safe flight of the T^3-Multirotor in a single-motor failure condition. The platform actively controls the position of the center of mass to restore the attitude-control torque disrupted by the motor-failure.

T^3-Multirotor, we introduce a new flight strategy that can independently control all four control inputs: roll, pitch, yaw, and thrust in the event of a single motor failure.

5.2 Mechanism and dynamics

In this section, we briefly describe the mechanism of the T^3-Multirotor and derive the platform's equations of motion.

5.2.1 Mechanism

Fig. 5.2 shows the schematic of the T^3-Multirotor. As shown in Fig. 5.2-A, the platform consists of three major parts: Thruster Part (TP), Cross Member (CM), and Fuselage Part (FP).

The TP consists of only a frame with four arms, four propeller thrusters and an IMU sensor. With thrusters, the TP can generate attitude control torques and overall thrust on the same principle as a regular quadcopter. Meanwhile, the FP consists of the remaining

components other than those mounted on the TP (e.g. battery, mission computer, auxiliary sensors). Since there are no thrusters on FP, it cannot generate thrust on its own. Instead, the FP is connected to the TP via the universal joint mechanism to receive the force required for flight.

The TP and the FP are connected to each of the two rotation axes of a CM, which is a cross-shaped rigid body with two orthogonal rotational axes (refer Fig. 5.2-A and B), whereby the TP and FP have degrees of freedom in roll and pitch rotation for the CM, respectively (refer Fig. 5.2-C and D). Then the servomotors are attached to the roll and pitch axes of CM to actively control the relative attitude. This feature allows the FP to take an arbitrary attitude independent of the TP while the TP performs attitude control for translational motion control as in the conventional multirotor.

As shown in Fig. 5.3, the structure of T^3-Multirotor is not limited to the shape shown in Fig. 5.2 and the arrangement of TP and FP may vary depending on the purpose of the mission. For example, if the platform needs to interact downward (e.g. cargo transportation [1], ground observation), a structure with FP at the bottom is desirable. On the contrary, in a mission requiring upward interaction (e.g. aerial surveillance, interaction with the ceiling), a structure in which the TP is located at the bottom is preferable. However, both structures have almost identical operating principles and motion dynamics, so the system can be controlled and operated in the same manner.

5.2.2   Platform dynamics

In this subsection, we describe the vehicle dynamics based on the T^3-Upright platform.

5.2.2.1   General equations of motion

The general translational and rotational equations of motion (EoM) of T^3-Multirotor are as follows [1].

$$
\begin{cases}
m_T \ddot{\mathbf{X}}_T = \mathbf{R}\left(\mathbf{q}_T\right) \mathbf{F}_T + m_T \mathbf{g} + \mathbf{F}_{FT} \\
m_F \ddot{\mathbf{X}}_F = m_F \mathbf{g} + \mathbf{F}_{TF}
\end{cases}
\tag{5.1}
$$
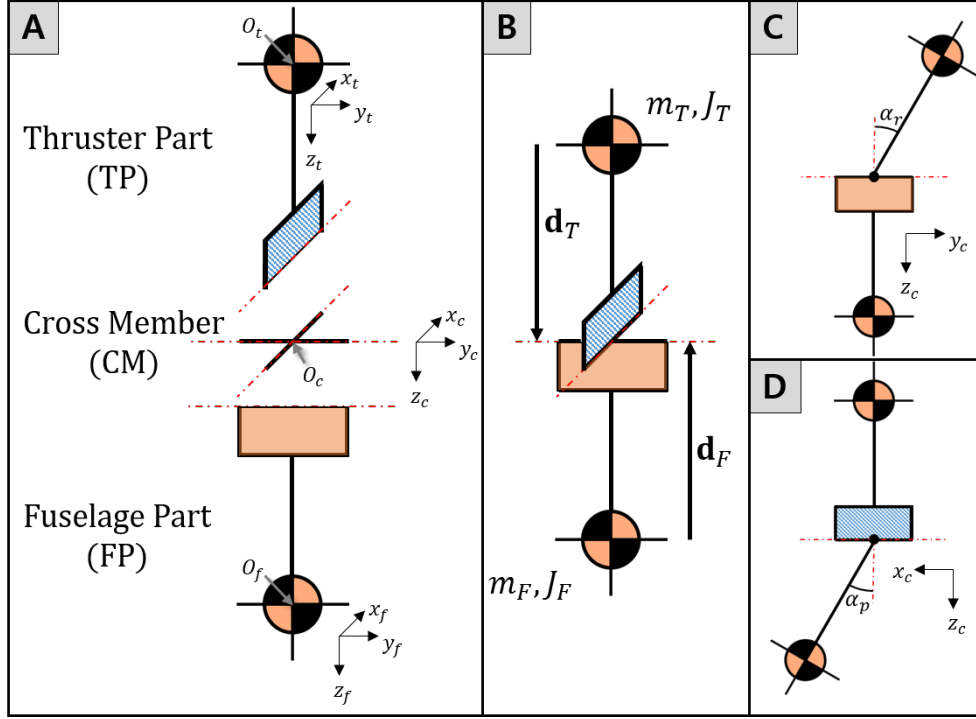
Figure 5.2: Schematic of the T^3-Multirotor. The platform consists of three major parts, where the relative roll and pitch attitude between TP and FP can be controlled.

$$\begin{cases} J_T \dot{\mathbf{\Omega}}_T = \mathbf{T}_T - \mathbf{\Omega}_T \times J_T \mathbf{\Omega}_T + \mathbf{d}_T \times \left(\mathbf{R}^{-1} \left(\mathbf{q}_T \right) \mathbf{F}_{FT} \right) + \mathbf{T}_{CT} \\ J_C \dot{\mathbf{\Omega}}_C = -R_r \left(\alpha_r \right) \mathbf{T}_{CT} - R_p \left(\alpha_p \right) \mathbf{T}_{CF} - \mathbf{\Omega}_C \times J_C \mathbf{\Omega}_C \\ J_F \dot{\mathbf{\Omega}}_F = -\mathbf{\Omega}_F \times J_F \mathbf{\Omega}_F + \mathbf{d}_F \times \left(\mathbf{R}^{-1} \left(\mathbf{q}_F \right) \mathbf{F}_{TF} \right) + \mathbf{T}_{CF}, \end{cases} \tag{5.2}$$

The symbol $m_* \in \mathbb{R}$ is the mass, $\mathbf{X}_* = [x_* \ y_* \ z_*]^T \in \mathbb{R}^{3 \times 1}$ is the position vector, $\mathbf{q}_* = [\phi_* \ \theta_* \ \psi_*]^T \in \mathbb{R}^{3 \times 1}$ is the attitude vector, $\mathbf{R}(\mathbf{q}_*) = R_y(\psi_*) R_p(\theta_*) R_r(\phi_*) \in SO(3)$ is the rotation matrix from the body frame to the Earth-fixed frame, $\mathbf{F}_T = [0 \ 0 \ -F_T]^T \in \mathbb{R}^{3 \times 1}$ is the thrust force vector generated by the TP defined in the body frame of the TP, $\mathbf{g} = [0 \ 0 \ g]^T \in \mathbb{R}^{3 \times 1}$ is the gravitational acceleration vector, and $\mathbf{F}_{ab} \in \mathbb{R}^{3 \times 1}$ is the reaction force vector acting from an object a to b defined in the Earth-fixed frame. The symbol $J_* = diag(J_{1,*}, J_{2,*}, J_{3,*}) \in \mathbb{R}^{3 \times 3}$ represents the moment of inertia, $\mathbf{\Omega}_* = [p_* \ q_* \ r_*]^T \in \mathbb{R}^{3 \times 1}$ is the angular velocity vector defined in the body frame, $\mathbf{T}_T = [\tau_{r,T} \ \tau_{p,T} \ \tau_{y,T}]^T \in \mathbb{R}^{3 \times 1}$ is the torque vector generated by the TP defined in the TP's body frame, $\mathbf{d}_* = [0 \ 0 \ d_*]^T \in \mathbb{R}^{3 \times 1}$ is the distance vector from the CoM of the TP / FP to the center of the universal joint defined
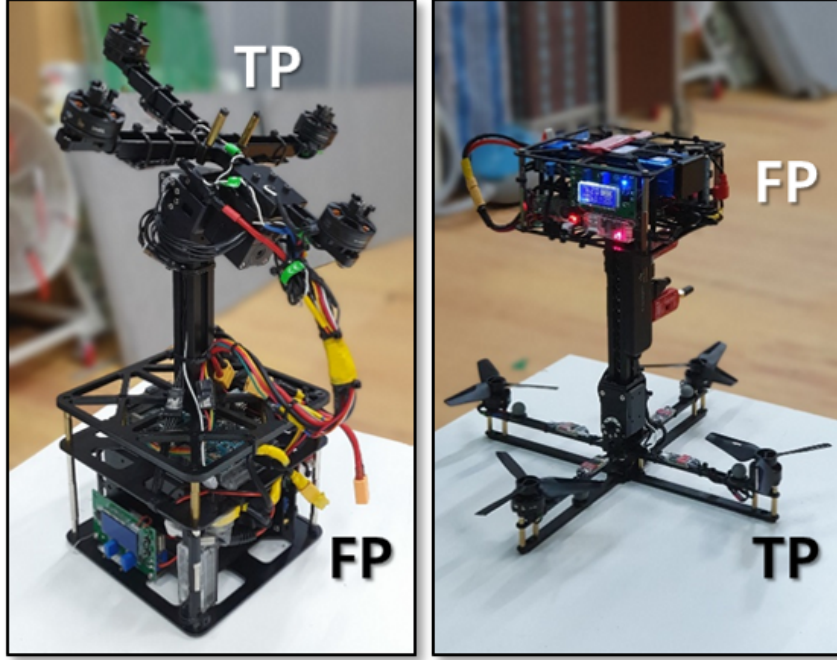
Figure 5.3: Examples of T^3-Multirotor structures that can vary depending on mission objectives. T^3-Upright (Left): Case where TP is on top of FP. T^3-Inverted (Right): Case where FP is on top of TP.

in the body frame, and $\mathbf{T}_{ab} \in \mathbb{R}^{3 \times 1}$ is the reaction torque vector acting from the object a to b defined in the body frame of the object b. The values α_r and α_p are relative angles of TP and FP respectively for CM as defined in Figs. 5.2-C and 5.2-D. The subscripts $(*)_T$ $(*)_C$ and $(*)_F$ represent TP, CM, and FP respectively.

5.2.2.2 Universal joint constraints

Due to the universal joint mechanism, the following relationship holds between the position vectors $\mathbf{X}_T$ and $\mathbf{X}_F$.

$$\mathbf{X}_T + \mathbf{R}(\mathbf{q}_T)\mathbf{r}_T = \mathbf{X}_F + \mathbf{R}(\mathbf{q}_F)\mathbf{r}_F \tag{5.3}$$

Also, the following relationship holds by the law of action and reaction.

$$\mathbf{F}_{TF} + \mathbf{F}_{FT} = 0 \tag{5.4}$$

The value J_C in rotational dynamics of CM in Equation (5.2) can be ignored because of its negligible physical quantity. Then, the EoM of the CM becomes the following rotational action-reaction relationship between TP and FP as

$$R_r(\alpha_r)\mathbf{T}_{CT} + R_p(\alpha_p)\mathbf{T}_{CF} = 0. \tag{5.5}$$

Also, the following relationship holds between $\mathbf{\Omega}_T$ and $\mathbf{\Omega}_F$ by the definition of α_r and α_F.

$$\mathbf{\Omega}_T - [\dot{\alpha}_r \; 0 \; 0]^T = \mathbf{\Omega}_F - [0 \; \dot{\alpha}_p \; 0]^T \tag{5.6}$$

The interaction torque between TP/FP and CM is definded as

$$\mathbf{T}_{C(*)} = \mathbf{T}_{s,C(*)} + \mathbf{T}_{f,C(*)}, \tag{5.7}$$

where $\mathbf{T}_{s,CT} = [\tau_{rs} \; 0 \; 0]^T$ and $\mathbf{T}_{s,CF} = [0 \; \tau_{ps} \; 0]^T$ are servo-generated torques, $\mathbf{T}_{f,CT} = [0 \; \tau_{p,CT} \; \tau_{y,CT}]^T$ and $\mathbf{T}_{f,CF} = [\tau_{r,CF} \; 0 \; \tau_{y,CF}]^T$ are the torques transferred by the CM structure. Applying Equation (5.7) to Equation (5.5), we can get the following relationships

$$\begin{cases} \tau_{p,CT} = -\frac{1}{c(\alpha_r)}\tau_{ps} + t(\alpha_r)\,\tau_{y,CT} \\ \tau_{r,CF} = -\frac{1}{c(\alpha_p)}\tau_{rs} - t(\alpha_p)\,\tau_{y,CF} \end{cases}, \tag{5.8}$$

where $c(*)$, $s(*)$ and $t(*)$ represent cosine, sine, and tangent functions. Among the terms of Equation (5.8), τ_{rs} and τ_{ps} are control inputs which are known values, so only $\tau_{y,CT}$ and $\tau_{y,CF}$ are unknown terms. To derive the yaw interaction torques, we need to revisit Equation (5.2). The yaw motion of TP and FP in the rotational EoMs of Equation (5.2) are as follows

$$\begin{cases} J_{3,T}\dot{r}_T = \tau_{y,T} + \tau_{y,CT} \\ J_{3,F}\dot{r}_F = \tau_{y,CF} \end{cases}, \tag{5.9}$$

where we applied the $\mathbf{\Omega}_* \times J_*\mathbf{\Omega}_* \approx 0$ assumption that is widely used in the simplification process of rotational dynamics of the multirotors [3], [61], [48]. Since the relationship of

73

$\dot{r}_T = \dot{r}_F$ holds by Equation (5.6), we can obtain the following yaw motion constraint from Equation (5.9) as

$$\frac{1}{J_{3,T}}\left(\tau_{y,T} + \tau_{y,CT}\right) = \frac{1}{J_{3,F}}\tau_{y,CF}. \tag{5.10}$$

By applying Equation (5.10) to Equation (5.5), we can derive the following result

$$\begin{cases} \tau_{y,CT} = \frac{J_{3,T}}{AJ_{3,T}+J_{3,F}}\left(-s(\alpha_p)\tau_{rs} - As(\alpha_r)\tau_{ps} - \frac{J_{3,F}}{J_{3,T}}\tau_{y,T}\right) \\ \tau_{y,CF} = \frac{J_{3,F}}{AJ_{3,T}+J_{3,F}}\left(-s(\alpha_p)\tau_{rs} - As(\alpha_r)\tau_{ps} + A\tau_{y,T}\right) \end{cases}, \tag{5.11}$$

where

$$A\left(\alpha_r, \alpha_p\right) = \frac{c(\alpha_p)\left(c^2(\alpha_r) + s^2(\alpha_p)\right)}{c(\alpha_r)\left(s^2(\alpha_r) + c^2(\alpha_p)\right)}. \tag{5.12}$$

5.2.2.3 Simplified equations of motion

It is known that the values of $\ddot{\mathbf{X}}_T$ and $\ddot{\mathbf{X}}_F$ are similar under normal flight conditions [1]. This condition brings the following simplified translational EoMs from Equation (5.1)

$$\begin{cases} \ddot{\mathbf{X}}_T = \frac{1}{M}\mathbf{R}(\mathbf{q}_T)\mathbf{F}_T + \mathbf{g} + \boldsymbol{\Delta}_T^{trans} \\ \ddot{\mathbf{X}}_F = \frac{1}{M}\mathbf{R}(\mathbf{q}_T)\mathbf{F}_T + \mathbf{g} + \boldsymbol{\Delta}_F^{trans}, \end{cases} \tag{5.13}$$

where M $(= m_T + m_F)$ is the overall mass of the platform, $\boldsymbol{\Delta}_*^{trans}$ is a gap between the simplified and actual translational acceleration of an object $(*)$ which remains small in most cases that satisfies $\ddot{\mathbf{X}}_T \approx \ddot{\mathbf{X}}_F$ assumption. From equations (5.1), (5.4) and (5.13), we can derive the values of $\mathbf{F}_{FT}$ and $\mathbf{F}_{TF}$ as

$$\begin{cases} \mathbf{F}_{TF} = \left(\frac{m_F}{M}\right)\mathbf{R}(\mathbf{q}_T)\mathbf{F}_T \\ \mathbf{F}_{FT} = -\mathbf{F}_{FT} \end{cases}. \tag{5.14}$$

In idle relative attitude condition $(\alpha_r, \alpha_p = 0)$, the interaction torques $\mathbf{T}_{CT}^{idle}$, $\mathbf{T}_{CF}^{idle}$ are as follows.

$$\mathbf{T}_{CT}^{idle} = \begin{bmatrix} \tau_{rs} \\ -\tau_{ps} \\ -\frac{J_{3,F}}{J_{3,T}+J_{3,F}}\tau_{y,T} \end{bmatrix}, \mathbf{T}_{CF}^{idle} = -\mathbf{T}_{CT}^{idle} \tag{5.15}$$

74

Thus, we can express the rotational interaction torques simply as

$$\mathbf{T}_{CT} = \mathbf{T}_{CT}^{idle} + \mathbf{\Delta}_{CT}^{rot}, \mathbf{T}_{CF} = \mathbf{T}_{CF}^{idle} + \mathbf{\Delta}_{CF}^{rot} \tag{5.16}$$

where $\mathbf{\Delta}_{C*}^{rot}$ represents the gap between idle and actual torque value.

By applying the equations (5.14) and (5.16) to (5.2), we can obtain the simplified rotational EoMs of the T^3-Multirotor as

$$\begin{cases} J_T \ddot{\mathbf{q}}_T = \mathbf{T}_T + \mathbf{T}_{CT}^{idle} + \mathbf{\Delta}_{CT}^{rot} \\ J_F \ddot{\mathbf{q}}_F = \left(\frac{m_F}{M}\right)\left(\mathbf{r}_F \times \left(\mathbf{R}^{-1}\left(\mathbf{q}_F\right)\mathbf{R}\left(\mathbf{q}_T\right)\mathbf{F}_T\right)\right) + \mathbf{T}_{CF}^{idle} + \mathbf{\Delta}_{CF}^{rot} \end{cases}, \tag{5.17}$$

where $\mathbf{\Delta}_{C*}^{rot}$ remains small under small relative attitude conditions.

5.3 Fail-safe flight strategy

In this section, we introduce a control method that utilizes the unique feature of the T^3-Multirotor to provide full control of the multirotor even under single motor failure condition. Then, we discuss the hardware requirement for enabling the proposed control strategy.

5.3.1 Fail-safe flight method

As is well known, the flight of the quadcopter is controlled via the signal $\mathbf{u} \in \mathbb{R}^{4\times1}$ [3], which is generated by combining four motor thrusts as

$$\mathbf{u} = \begin{bmatrix} \mathbf{T}_T \\ F_T \end{bmatrix} = \begin{bmatrix} 0 & -l & 0 & l \\ l & 0 & -l & 0 \\ \frac{b}{k} & -\frac{b}{k} & \frac{b}{k} & -\frac{b}{k} \\ 1 & 1 & 1 & 1 \end{bmatrix} \mathbf{c_0}, \ \mathbf{c_0} = \begin{bmatrix} F_1 \\ F_2 \\ F_3 \\ F_4 \end{bmatrix}. \tag{5.18}$$

The symbol $l \in \mathbb{R}$ represents the length of the TP arm, $\frac{b}{k} \in \mathbb{R}$ represents the ratio between the yaw torque and the thrust force of the motor under the same rotation speed condition, and $F_i \in \mathbb{R}$ represents the thrust force generated from motor i.
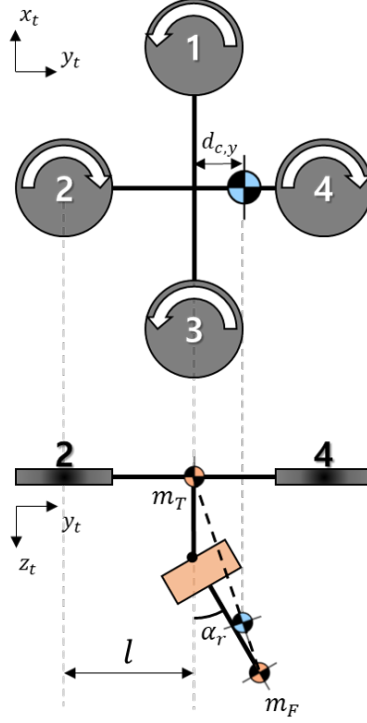
Figure 5.4: The platform's overall CoM position $d_{c,\{x,y\}}$ can be changed by manipulating the relative attitude $\alpha_{\{r,p\}}$.

Unlike conventional multirotor, T^3-Multirotor is equipped with two additional servo-motors to control relative attitudes between TP and FP. Therefore, two control inputs (τ_{rs}, τ_{ps}) are added to the four existing control inputs, make a total of six control inputs of the system. This allows the T^3-Multirotor to perform four c-DOF flight even in a single motor failure condition and partially in a dual-motor failure condition.

The fail-safe flight method that we introduce can be derived through both kinematics and dynamics-based approaches, where we provide both approaches in this subsection.

5.3.1.1 Kinematics-based approach

By taking advantage of the platform's capability of relative attitude control, we can change the platform's CoM position. Fig. 5.4 shows the y-directional CoM position change according to the relative roll attitude $\alpha_r \in \mathbb{R}$. In the same manner, we can also change the CoM position in the x-direction with pitch servomechanism.

The position of the altered CoM with respect to the TP frame is represented by $\mathbf{X}_{CoM} = [d_{c,x} \; d_{c,y} \; d_{c,z}]^T \in \mathbb{R}^{3\times1}$, and the relationship between the relative attitudes and the CoM position are as follows.

$$
\mathbf{X}_{CoM} = \frac{1}{M}\left(m_T \begin{bmatrix} 0 \\ 0 \\ 0 \end{bmatrix} + m_F \left(\begin{bmatrix} 0 \\ 0 \\ d_T \end{bmatrix} + R_r(\alpha_r)R_p(\alpha_p) \begin{bmatrix} 0 \\ 0 \\ d_F \end{bmatrix} \right) \right) \tag{5.19}
$$

Then, we can find the relationship between relative attitude $\alpha_{\{r,p\}}$ and $d_{c,\{x,y\}}$ derived from Equation (5.19) as follows.

$$
\begin{cases} \alpha_p = \arcsin\left(\frac{M}{m_F} \frac{d_{c,x}}{d_F} \right) \\ \alpha_r = \arcsin\left(\frac{-1}{\cos(\alpha_p)} \frac{M}{m_F} \frac{d_{c,y}}{d_F} \right) \end{cases} \tag{5.20}
$$

Thus, we can calculate the required servomotor angles to relocate the position of CoM to the desired location.

The attitude-control torques reflecting the change in position of CoM are as follows.

$$
\begin{cases} \tau_{r,T} = -(l + d_{c,y}) F_2 - d_{c,y}(F_1 + F_3) + (l - d_{c,y}) F_4 \\ \tau_{p,T} = (l - d_{c,x}) F_1 - d_{c,x}(F_2 + F_4) - (l + d_{c,x}) F_3 \\ \tau_{y,T} = \frac{b}{k}(F_1 - F_2 + F_3 - F_4) \end{cases} \tag{5.21}
$$

Based on the result of Equation (5.21), the control input $\mathbf{u}$ of the T^3-Multirotor becomes as

$$
\begin{aligned}
\mathbf{u} &= \begin{bmatrix} \mathbf{T}_T \\ F_T \end{bmatrix} = A(F_T)\mathbf{c}_{aug} \\
&= \begin{bmatrix} 0 & -l & 0 & l & 0 & -F_T \\ l & 0 & -l & 0 & -F_T & 0 \\ \frac{b}{k} & -\frac{b}{k} & \frac{b}{k} & -\frac{b}{k} & 0 & 0 \\ 1 & 1 & 1 & 1 & 0 & 0 \end{bmatrix} \mathbf{c}_{aug},
\end{aligned} \tag{5.22}
$$

where $A(F_T) \in \mathbb{R}^{4 \times 6}$ is the relationship between $\mathbf{c}_{aug}$ and $\mathbf{u}$, $\mathbf{c}_{aug} = [\mathbf{c_0}^T \mathbf{d}^T]^T \in \mathbb{R}^{6 \times 1}$ is an augmented input vector, and $\mathbf{d} = [d_{c,x} \ d_{c,y}]^T \in \mathbb{R}^{2 \times 1}$ is a CoM position. From Equation (5.22), we can see that the system became a redundant system with six inputs to generate $\mathbf{u} \in \mathbb{R}^{4 \times 1}$.

Single motor failure In the case of a single motor failure, our strategy is to relocate the position of CoM along the axis where the failed motor is located, in order to obtain the necessary additional attitude control torque. For example, when Motor 2 of the T^3-Multirotor with the motor configuration shown in Fig. 5.4 fails, our strategy is to fix the $d_{c,x}$ value to zero and apply only $d_{c,y}$ as augmented control input to restore the controllability of the system. As a result, Equation (5.22) changes as follows

$$\mathbf{u} = A_2(F_T)\mathbf{c}_2 = \begin{bmatrix} 0 & 0 & l & -F_T \\ l & -l & 0 & 0 \\ \frac{b}{k} & \frac{b}{k} & -\frac{b}{k} & 0 \\ 1 & 1 & 1 & 0 \end{bmatrix} \mathbf{c}_2, \tag{5.23}$$

where $\mathbf{c}_2 = [F_1 \ F_3 \ F_4 \ d_{c,y}]^T \in \mathbb{R}^{4 \times 1}$ and $A_2(F_T) \in \mathbb{R}^{4 \times 4}$ are new control input and matrix excluding components corresponding to F_2 and $d_{c,y}$ from control input $\mathbf{c}$ and matrix $A(F_T)$. Since $rank\,(A_2(F_T)) = 4$ condition always holds during the flight ($F_T > 0$), we can calculate

the value of $\mathbf{c}_2$ to satisfy the desired $\mathbf{u}$ as follows.

$$
\mathbf{c}_2 = A_2^{-1}(F_T)\mathbf{u} = \begin{bmatrix} 0 & \frac{1}{2l} & \frac{k}{4b} & 0.25 \\ 0 & -\frac{1}{2l} & \frac{k}{4b} & 0.25 \\ 0 & 0 & -\frac{k}{2b} & 0.5 \\ -\frac{1}{F_T} & 0 & -\frac{lk}{2bF_T} & \frac{l}{2F_T} \end{bmatrix} \mathbf{u}
$$

$$
= \begin{bmatrix} \frac{1}{2l}\tau_{p,T} + \frac{k}{4b}\tau_{y,T} + 0.25F_T \\ -\frac{1}{2l}\tau_{p,T} + \frac{k}{4b}\tau_{y,T} + 0.25F_T \\ -\frac{k}{2b}\tau_{y,T} + 0.5F_T \\ -\frac{1}{F_T}\left(\tau_{r,T} + \frac{lk}{2b}\tau_{y,T}\right) + 0.5l \end{bmatrix}
$$

(5.24)

In the same principle, we can reconfigure A_i and $\mathbf{c}_i$ to recover the controllability in the event of a motor $i = 1, 2, 3, 4$ failure.

(Optional) Dual motor failure In case of dual motor failure, we can configure $\mathbf{c}_{ij} \in \mathbb{R}^{4\times1}$ and $A_{ij}(F_T) \in \mathbb{R}^{4\times4}$ by excluding terms and matrix columns related to the failed motors i and j. However, if the combination of failed motors is $i = 1, j = 3$ or $i = 2, j = 4$, $Rank\,(A_{i,j})$ becomes 3, which makes nominal 4-cDOF flight impossible. But otherwise, the signal $\mathbf{c}_{ij}$ can always be found to satisfy all components of $\mathbf{u}$ vector.

5.3.1.2 Dynamics-based approach

Applying equations (5.15) and (5.16) to (5.17), we get the following relationship.

$$
J_T\ddot{\mathbf{q}}_T = \mathbf{T}_T - \frac{m_F d_F}{M} \begin{bmatrix} s(\alpha_r) \\ -s(\alpha_p)c(\alpha_r) \\ 0 \end{bmatrix} F_T - J_F\ddot{\mathbf{q}}_F + \boldsymbol{\Delta}_{CT}^{rot} + \boldsymbol{\Delta}_{CF}^{rot}
$$

(5.25)

Then, by applying Equation (5.20) to (5.25), we can obtain the following equation

$$
\begin{aligned}
J_T \ddot{\mathbf{q}}_T &= \mathbf{T}_T - F_T \begin{bmatrix} d_{c,y} \\ d_{c,x} \\ 0 \end{bmatrix} - J_F \ddot{\mathbf{q}}_F + \mathbf{\Delta}_{CT}^{rot} + \mathbf{\Delta}_{CF}^{rot} \\
&= (A(F_T)\mathbf{c}_{aug})_{[1:3]} - J_F \ddot{\mathbf{q}}_F + \mathbf{\Delta}_C^{rot}
\end{aligned}
\tag{5.26}
$$

where $(A(F_T)\mathbf{c}_{aug})_{[1:3]}$ is a sub-matrix of rows 1 to 3 of $A(F_T)\mathbf{c}_{aug}$ in the Equation (5.22) and $\mathbf{\Delta}_C^{rot}$ is the sum of the residuals. From Equation (5.26), we can see that the control input for governing the rotational motion of TP is derived in the same way as in Equation (5.22). Thus, the fail-safe flight strategy introduced in the kinematics-based approach is valid even in the dynamics-based approach.

However, unlike Equation (5.22), Equation (5.26) shows that there are reaction torque components due to the rotational motion of the FP. Therefore, consideration of the reaction torque generated from the FP's rotational motion is required during a fail-safe controller design.

5.3.2   Hardware condition for single motor fail-safe flight

Now, we examine the physical conditions of the T^3-Multirotor to perform a suggested single motor fail-safe flight. The hardware conditions are derived from the Motor 2 failure scenario, but the results are valid for all single motor failure scenarios.

From Equation (5.24), we can find the idle value of $\mathbf{c}_2$ to satisfy hovering condition $\mathbf{u}^{hover} = [0\ 0\ 0\ Mg]^T$ during Motor 2 fail-safe flight as follows.

$$
\begin{aligned}
\mathbf{c}_2^{idle} &= A_2^{-1}(Mg)\mathbf{u}^{hover} \\
&= [0.25Mg\ 0.25Mg\ 0.5Mg\ 0.5l]^T
\end{aligned}
\tag{5.27}
$$

And we can define the ranges of $\mathbf{T}_T$ and F_T in flight as follows

$$|\tau_{r,T}| \leq \Delta_r, \ |\tau_{p,T}| \leq \Delta_p, \ |\tau_{y,T}| \leq \Delta_y,$$
$$-Mg \leq (F_T - Mg) \leq \Delta_t, \tag{5.28}$$

where $\Delta_{\{r,p,y,t\}}$ represent the maximum control input which are limited by both hardware and software conditions. Applying equations (5.27) and (5.28) to (5.24), we can obtain the maximum value of $\mathbf{c}_2$ that can occur in a fail-safe flight as

$$\mathbf{c}_2^{max} = \mathbf{c}_2^{idle} + \begin{bmatrix} \frac{1}{2l}\Delta_p + \frac{k}{4b}\Delta_y + 0.25\Delta_t \\ \frac{1}{2l}\Delta_p + \frac{k}{4b}\Delta_y + 0.25\Delta_t \\ \frac{k}{2b}\Delta_y + 0.5\Delta_t \\ \frac{1}{Mg-\Delta_t}\left(\Delta_r + \frac{lk}{2b}\Delta_y\right) \end{bmatrix}. \tag{5.29}$$

Constraints imposed on the T^3-Multirotor include the maximum thrust constraint of the individual motor and the maximum relative attitude constraint. First, in the case of thrust constraints, we can define the thrust range of the individual motor as follows.

$$0 \leq F_i \leq F_{max}, \ i = 1, 2, 3, 4 \tag{5.30}$$

Amongst the F_i of $\mathbf{c}_2^{max}$ in Equation (5.29), F_4 has the largest value during the flight. Therefore, for motor thrust, we need to verify whether the value of F_4 does not exceed the condition of Equation (5.30) during the flight.

The range of relative attitude determined by the hardware configuration is as follows Next, for relative attitude constraints, we can define the range of relative attitude as follows:

$$|\alpha_{r,p}| \leq \Delta_\alpha, \tag{5.31}$$

81

which brings the following constraint from Equation (5.20) as

$$|d_{c,\{x,y\}}| \leq \frac{m_F d_F}{M} s(\Delta_\alpha).$$

(5.32)

Therefore, we need to verify that $d_{c,y}$ always satisfies the condition in Equation (5.32) during the flight.

Based on the above two constraints, the conditions of T^3-Multirotor's fail-safe flight are:

$$\begin{cases} 0.5\left(Mg + \frac{k}{b}\Delta_y + \Delta_t\right) \leq F_{max} \\ 0.5l + \frac{1}{Mg-\Delta_t}\left(\Delta_r + \frac{lk}{2b}\Delta_y\right) \leq \frac{m_F d_F}{M}s(\Delta_\alpha) \end{cases}.$$

(5.33)

Among the variables in Equation (5.33), F_{max}, $\frac{b}{k}$, Δ_α, and $\Delta_{\{r,p,y,t\}}$ are fixed values. Therefore, the adjustable hardware parameters remain M, m_F, l and d_F. Thus, Equation (5.33) can be rewritten as

$$\begin{cases} M \leq \frac{1}{g}\left(2F_{max} - \frac{k}{b}\Delta_y - \Delta_t\right) \\ d_F \geq \frac{M}{m_F s(\Delta_\alpha)}\left(0.5l + \frac{1}{Mg-\Delta_t}\left(\Delta_r + \frac{lk}{2b}\Delta_y\right)\right) \end{cases}.$$

(5.34)

The conditions of Equation (5.34) can be explained as follows.

5.3.2.1 Mass constraint

As we see in Equation (5.27), the motor on the opposite side of the failed motor must generate a thrust equal to half of the fuselage weight. This is because the opposite side of a failed motor is the only actuator to offset the yaw torque of the other two remaining motors rotating in the same direction. Therefore, the overall mass M should be less than twice the maximum thrust of the individual motors $(2F_{max}/g)$ and the value should be lesser to generate extra yaw torque and thrust for vehicle control.
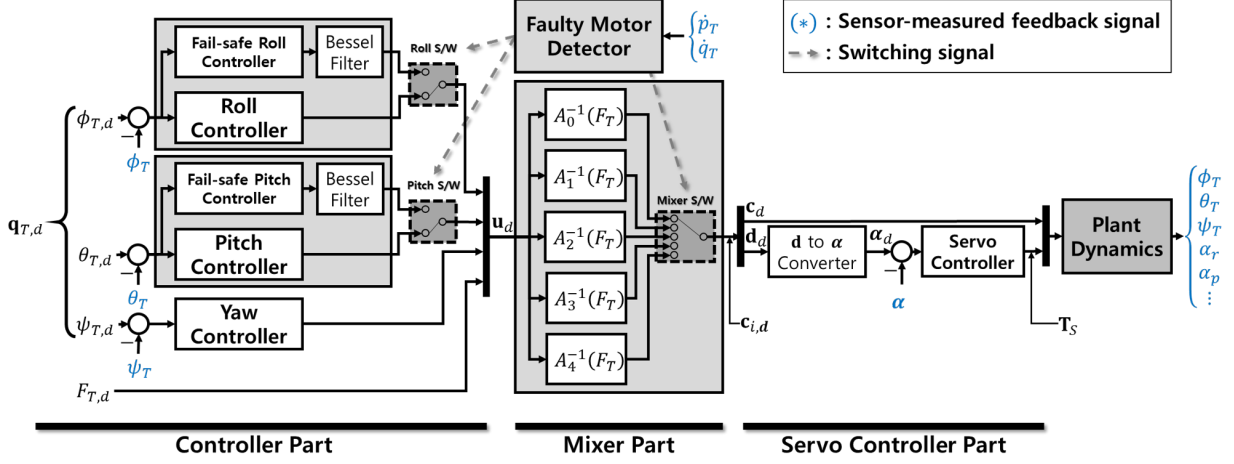
Figure 5.5: The control scheme of the T^3-Multirotor with a fail-safe algorithm. The 'Faulty Motor Detector' monitors the roll and pitch angular accelerations to identify the failed motor, and then activates the fail-safe controller and mixer matrix $A_i^{-1}(F_T)$ by triggering roll/pitch switch and mixer switch.

5.3.2.2 d_F constraint

Equation (5.27) also shows that the altered CoM should be located around a half the length of the TP arm l in the hovering state. Thus, the d_F value should be greater than $\frac{0.5lM}{m_F s(\Delta_\alpha)}$ (refer Equations (5.20) and (5.34)) and should include extra redundancy for stable platform control.

5.4 Controller design

In this section we introduce a fail-safe flight controller design. First, we introduce a faulty motor detection method, and then introduce a detailed structure of the proposed fail-safe flight controller.

5.4.1 Faulty motor detection

In nominal flight, all attitude control torques of T^3 -Multirotor are generated through a combination of thrusts according to the relationship in Equation (5.18). In this case, $d_{c,\{x,y\}}$,

Table 5.1: Faulty motor identification table

Condition	Faulty Motor	Condition	Faulty Motor
$\dot{p}_T > \beta$	Motor 4	$\dot{q}_T > \beta$	Motor 3
$\dot{p}_T < -\beta$	Motor 2	$\dot{q}_T < -\beta$	Motor 1

and $\mathbf{\Delta}_{C,\{T,F\}}^{R}$ values remain zero, and the Equation (5.26) becomes as follows.

$$(J_T + J_F)\,\ddot{\mathbf{q}}_T = \mathbf{T}_T, \;\; \ddot{\mathbf{q}}_F = \ddot{\mathbf{q}}_T \tag{5.35}$$

Under these conditions, a single motor failure results in the instantaneous generation of abnormally large roll or pitch torque with a magnitude of lF_k, causing a rotational acceleration of $lF_k / \left(J_{\{1,2\},T} + J_{\{1,2\},F}\right)$. Here, the symbol k, which is

$$\begin{cases} k = i + 2 \;\; (i = 1, 2) \\ k = i - 2 \;\; (i = 3, 4) \end{cases},$$

indicates the motor located on the opposite side of the failed motor. Thus, we can specify a faulty motor according to the relationship in Table I, where the value $\beta \in \mathbb{R}$ is defined as

$$\beta = \gamma \frac{0.25lMg}{J_{\{1,2\},T} + J_{\{1,2\},F}}. \tag{5.36}$$

Equation (5.36) includes the $F_i \approx 0.25Mg$ assumption, and the value $\gamma \in \mathbb{R}$ is a heuristically adjustable parameter.

5.4.2 Controller design

Fig. 5.5 shows the structure of a flight controller designed to achieve the proposed fail-safe flight. The proposed controller is divided into four parts: Controller Part, Mixer Part, Servo Controller Part, and Faulty Motor Detector.

5.4.2.1 Controller part

The Controller Part includes a roll, pitch and yaw controller for controlling the attitude of the TP. For roll and pitch controllers, however, two selectable sub-controllers are configured in each controller block. This configuration is due to the difference in system dynamics between normal and fail-safe flight. In normal flight, the relationship between $\tau_{\{r,p\},T}$ and $\{\phi, \theta\}$ are defined by the Equation (5.35). However, in the fail-safe scenario, the relationship changes and mainly governed by the rules of the Equation (5.25). Therefore, in order to maintain the performance and stability of the system in two different situations, a separate suiting controller with a switching algorithm must be configured. Also in Fig. 5.5, an independent 'Faulty Motor Detector' is configured to trigger the switching function of the Roll, Pitch and Mixer switch. The detector follows the operation principle of Table 5.1, where it activates Roll S/W in case of failure of motor 2 or 4 and Pitch S/W in case of failure of motor 1 or 3.

In a fail-safe mode, servo motor becomes the sole actuator to generate the $\tau_{\{r,p\},T}$ command of the disrupted attitude channel $\big($refer Equation (5.24)$\big)$. However, the servo motor has significantly slow response characteristics compared to the motor thruster due to their inherent characteristics. This characteristics often causes destructive vibration when high-frequency control input is applied. To avoid this issue, a low pass filter is introduced to limit the frequency of the control input applied to the servo motor. In our research, a Bessel filter with maximally flat phase delay characteristics is introduced to prevent additional phase delay.

5.4.2.2 Mixer part

For the Mixer Part, the Faulty Motor Detector triggers the Mixer S/W to select the $A_i^{-1}(F_T)$ matrix in accordance of the failed motor i for generating $\mathbf{c}_i$ command. Here, $i = 0$ indicates that no faults occurred, so $A_0(F_T) \in \mathbb{R}^{4\times4}$ is the same conversion matrix as the sub-matrix of columns 1 to 4 of $A(F_T)$ matrix in Equation (5.22). All other components of $\mathbf{c}_{aug}$ not

included in $\mathbf{c}_i$ have a value of zero throughout the flight.

5.4.2.3　Servo controller part

The $\mathbf{c}_i$ signal generated by the Mixer Part is sent to the Servo Controller Part. Among the signals included in $\mathbf{c}_{i,d}$, the motor control signal $\mathbf{c}_d$ is directly applied to the thrusters. However, the $\mathbf{d}_d$ signal, which is a desired CoM position signal, passes through an independent servo controller. First, the $\mathbf{d}_d$ signal is converted into an $\boldsymbol{\alpha}_d = [\alpha_{r,d}\ \alpha_{p,d}]^T \in \mathbb{R}^{2\times 1}$ signal through Equation (5.20). Then, the feedback servo controller generates the servo torque $\mathbf{T}_s$ for the relative attitude control and changes the relative attitude $\boldsymbol{\alpha}$.

5.4.2.4　Faulty motor detector

The Faulty Motor Detector monitors the angular acceleration of the TP. When a faulty motor is identified according to the relationships in Table I, it commands Roll or Pitch S/W and Mixer S/W to select the appropriate fail-safe controller and $A_i^{-1}(F_T)$ matrix.

5.4.3　Attitude dynamics in fail-safe mode

Among the structures in Fig. 5.5, the input/output relationship of the attitude component subject to fail-safe mode is shown in Fig. 5.6. The structure is classified into three blocks. In this section, we analyze the input/output relationships of individual blocks and derive the transfer function of the TP attitude in fail-safe mode.

5.4.3.1　Block 1

Block 1 of Fig. 5.6 is an input/output system of relative attitude $\alpha_{\{r,p\}}$. By applying the PID control scheme as a servo controller, the input/output transfer function of Block 1 is

Figure 5.6: The fail-safe input-output relationship of the attitude channel disrupted by motor failure.

derived from Equation (5.17) as follows

$$
\begin{aligned}
\Lambda_\alpha(s) &= \frac{\alpha_{\{r,p\}}(s)}{\alpha_{\{r,p\},d}(s)} \\
&\approx \frac{D_s s^2 + P_s s + I_s}{\zeta_{\{1,2\}} s^3 + D_s s^2 + \left(P_s - \frac{\zeta_{\{1,2\}} m_F d_F g}{J_{\{1,2\},F}}\right) s + I_s},
\end{aligned}
\tag{5.37}
$$

where

$$
\zeta_{\{1,2\}} = \frac{J_{\{1,2\},T} J_{\{1,2\},F}}{J_{\{1,2\},T} + J_{\{1,2\},F}}.
\tag{5.38}
$$

The derivation includes the $F_T \approx Mg$ (hovering condition) and $\sin\left(\alpha_{\{r,p\}}\right) \approx \alpha_{\{r,p\}}$ (small-angle approximation) assumptions that are valid during most of the flight. The symbols $P_s,\ I_s\ D_s \in \mathbb{R}$ represent gains of the Servo Controller.

5.4.3.2 Block 2

Block 2 is an input/output system of the fail-safe attitude control torque $\tau_{\{r,p\},T}$. The block first converts the torque command $\tau_{\{r,p\},T,d}$ to the target CoM position $d_{c,\{x,y\},d}$ as in Equation (5.24), and then converts $d_{c,\{x,y\},d}$ to the target relative attitude $\alpha_{\{r,p\},d}$ according to the relationship in Equation (5.20). The $\alpha_{\{r,p\},d}$ is then passes through Λ_α dynamics to become $\alpha_{\{r,p\}}$, $d_{c,\{x,y\}}$, and $\tau_{\{r,p\}}$.

If we define L as the signal transformation that is made through the continuous calculation of Equations (5.24) and (5.20), L can be expressed as follows.

$$
\begin{aligned}
\alpha_{\{r,p\}} &= L\left(\tau_{\{r,p\},T}, \tau_{y,T}, F_T\right) \\
&= \arcsin\left(\frac{M}{m_F d_F}\left(\frac{\tau_{\{r,p\},T} + \frac{lk}{2b}\tau_{y,T}}{F_T} - 0.5l\right)\right)
\end{aligned}
\tag{5.39}
$$

Then, by introducing the stable flight assumptions of $F_T \approx Mg$ and $\tau_{y,T} \approx 0$ into L, $\bar{L}$ the simplified version of L becomes as

$$
\begin{aligned}
\bar{L}\left(\delta\right) &= \arcsin\left(\delta\left(\tau_{\{r,p\},T}\right)\right) \\
\delta\left(\tau_{\{r,p\},T}\right) &= \frac{\tau_{\{r,p\},T} - 0.5 m_F d_F gl}{m_F d_F g},
\end{aligned}
\tag{5.40}
$$

which is a SISO signal conversion. Thus, we define the conversion between torque and relative attitude of Block 2 in general flight conditions as $\bar{L}\left(\delta\right)$.

During the fail-safe flight, $\alpha_{\{r,p\}}$ has a narrow range of motion. In this case we can treat $\bar{L}$ as a linear signal transformation. Since the identical forward and inverse linear transformations are located before and after the Λ_α transfer function, we can conclude the torque transfer function Λ_τ of Block 2 as follows [62].

$$
\Lambda_\tau(s) \approx \Lambda_\alpha(s).
\tag{5.41}
$$

The small operation range of $\alpha_{\{r,p\}}$ in fail-sfe flight mode will be confirmed by later experimental results.

5.4.3.3 Block 3

A second-order filter is selected for Bessel filter, in which case the transfer function is

$$\Lambda_B(s) = \frac{3}{(s/f_B)^2 + 3\,(s/f_B) + 3}. \tag{5.42}$$

The symbol $f_B \in \mathbb{R}$ represents the cutoff frequency of the filter. If we select the PID controller as a fail-safe controller, the transfer function of the controller block becomes as follows.

$$\Lambda_{FS}(s) = \frac{D_f s^2 + P_f s + I_f s}{s} \tag{5.43}$$

The symbols $P_f, I_f, D_f \in \mathbb{R}$ represent gains of the Fail-safe Controller.

From Equation (5.26), we can derive the transfer function between the servo torque and the TP attitude. First we apply $\alpha_{\{r,p\}} = \{\phi, \theta\}_T - \{\phi, \theta\}_F$ relationship into the equation (5.26) to bring the following equation

$$(J_{T,\{1,2\}} + J_{F,\{1,2\}})\{\ddot{\phi}, \ddot{\theta}\}_T = \tau_{\{r,p\}} + J_F \ddot{\alpha}_{\{r,p\}}, \tag{5.44}$$

where $\tau_{\{r,p\}}$ is the torque generated by the position shift of CoM, and $J_F \ddot{\alpha}_{\{r,p\}}$ is the inertial term generated during the relative attitude motion. Since the effect of the inertia remains small with respect to the $\tau_{\{r,p\}}$ term due to the small value of J_F, we can derive the following transfer function between $\tau_{\{r,p\}}$ and $\{\phi, \theta\}_T$ as

$$\Lambda_{\tau\{\phi,\theta\}} \approx \frac{1}{\left(J_{T,\{1,2\}} + J_{F,\{1,2\}}\right) s^2} \tag{5.45}$$

Then, the final form of the input/output attitude transfer function in fail-safe mode becomes as follows.

$$\Lambda_{\{\phi,\theta\}} = \frac{1}{1 + \Lambda_{FS}\Lambda_B\Lambda_\alpha\Lambda_{\tau\{\phi,\theta\}}} \tag{5.46}$$

5.5 Experiment result

5.5.1 Experimental settings

The 'T^3-Inverted' platform in Fig. 5.3 is selected for fail-safe flight. In the case of the T^3-Upright platform, the FP could interfere with the TP's downwash airflow during the CoM position control. However, with the T^3-Inverted platform, thrusters can always maintain nominal performance throughout the flight since there is no airflow obstruction by the FP during the CoM position control.

Table 5.2 shows the hardware parameters and the controller gains of the experimental platform. This information allows us to determine the availability of fail-safe flight through the proposed platform. By applying the above information to Equation (5.24), we can have the following results.

$$
\begin{cases}
M = 1.31 \, \text{kg} \leq 2.325 \, \text{kg} \\
d_F = 0.21 \, \text{m} \geq 0.1847 \, \text{m}
\end{cases}
\tag{5.47}
$$

Since both M and d_F values satisfy the conditions, we can conclude that fail-safe flight through the proposed platform is valid. Also, we can predict from Equation (5.24) that the platform has an average relative attitude of $0.5328 \, \text{rad}$ during flight.

Table 5.2: Physical quantities and controller gains of the experimental platform

Physical Parameters			
Parameter	Value	Parameter	Value
m_T	$0.389\,\text{kg}$	$J_{\{1,2\},T}$	$\approx 0.002\,\text{kg} \cdot \text{m}^2$
m_F	$0.921\,\text{kg}$	$J_{3,T}$	$\approx 0.01\,\text{kg} \cdot \text{m}^2$
d_T	$0.02\,\text{m}$	$J_{\{1,2\},F}$	$\approx 0.014\,\text{kg} \cdot \text{m}^2$
d_F	$0.21\,\text{m}$	$J_{3,F}$	$\approx 0.04\,\text{kg} \cdot \text{m}^2$
l	$0.15\,\text{m}$	b/k ratio	≈ 0.05
F_{max}	$12.9\,\text{N}$		-

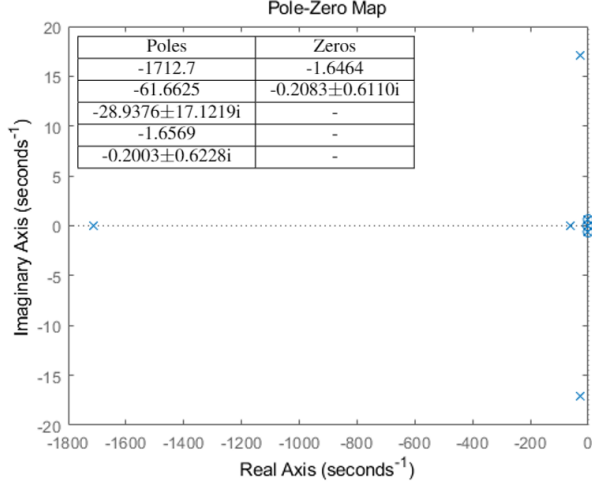| Controller Gains			
Gain	Value	Gain	Value
P_n	3	P_f	0.1
I_n	0.5	I_f	0.1
D_n	0.3	D_f	0.24
P_s	5	Yaw Atti. P gain	0.3
I_s	0.1	Yaw Atti. I gain	0.01
D_s	3	Yaw Atti. D gain	0.06
Pos. P gain	2	Height P gain	10
Pos. I gain	0.5	Height I gain	1
Pos. D gain	2	Height D gain	1
$\Delta_{\{r,p\}}$	$0.5\,\text{N} \cdot \text{m}$	Δ_y	$0.1\,\text{N} \cdot \text{m}$
Δ_t	$1\,\text{N}$	Δ_α	$1.5708\,\text{rad}$
f_b	$40\,\text{Hz}$		-

Figure 5.7: The location of the poles and zeros of the transfer function $\Lambda_{\{\phi,\theta\}}$.
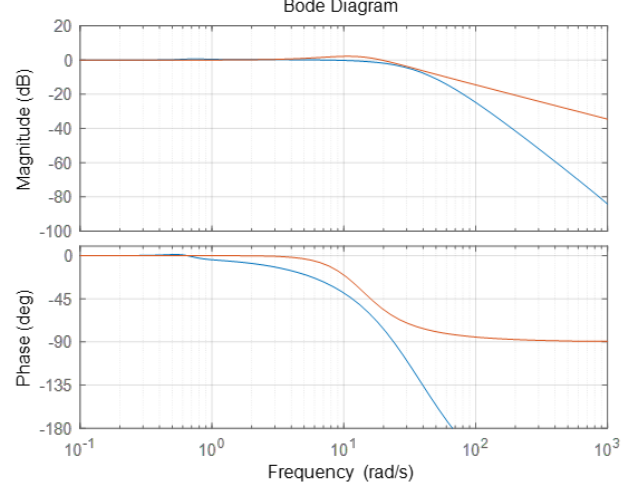
Figure 5.8: Comparison of Bode magnitude and phase plot of the transfer functions $\Lambda_{\{\phi,\theta\},nom}$ (red) and $\Lambda_{\{\phi,\theta\}}$ (blue).

5.5.2 Stability and control performance review

A simple stability analysis can be performed using the fail-safe attitude transfer function of Equation (5.46) with the parameters in Table II. Fig. 5.7 shows the locations of the poles and zeros of $\Lambda_{\{\phi,\theta\}}$. Here we can see that the system is a minimum phase proper system whose relative degree is four. Thus we can confirm that the system is stable at the current gain settings and physical parameters.

The frequency response of the fail-safe flight system is reviewed to examine the control performance in fail-safe mode. Fig. 5.8 is a bode diagram with comparison between the nominal flight and the fail-safe flight. For nominal flight, the transfer function is

$$\Lambda_{\{\phi,\theta\},nom} = \frac{D_n s^2 + P_n s + I_n}{\left(J_{T,\{1,2\}} + J_{F,\{1,2\}}\right) s^3 + D_n s^2 + P_n s + I_n} \tag{5.48}$$

which is similar to Equation (3.24), where $P_n, I_n, D_n \in \mathbb{R}$ represent nominal PID attitude gains applied in non-fail-safe roll and pitch controller. Here, we can see that both systems show $0\,\mathrm{dB}$ magnitude response in the range up to about $50\,\mathrm{Hz}$, but relatively large phase shift compared to the nominal flight mode occurs in fail-safe mode. Thus, a relatively large output delay compared to the nominal attitude control is expected in fail-safe mode due to
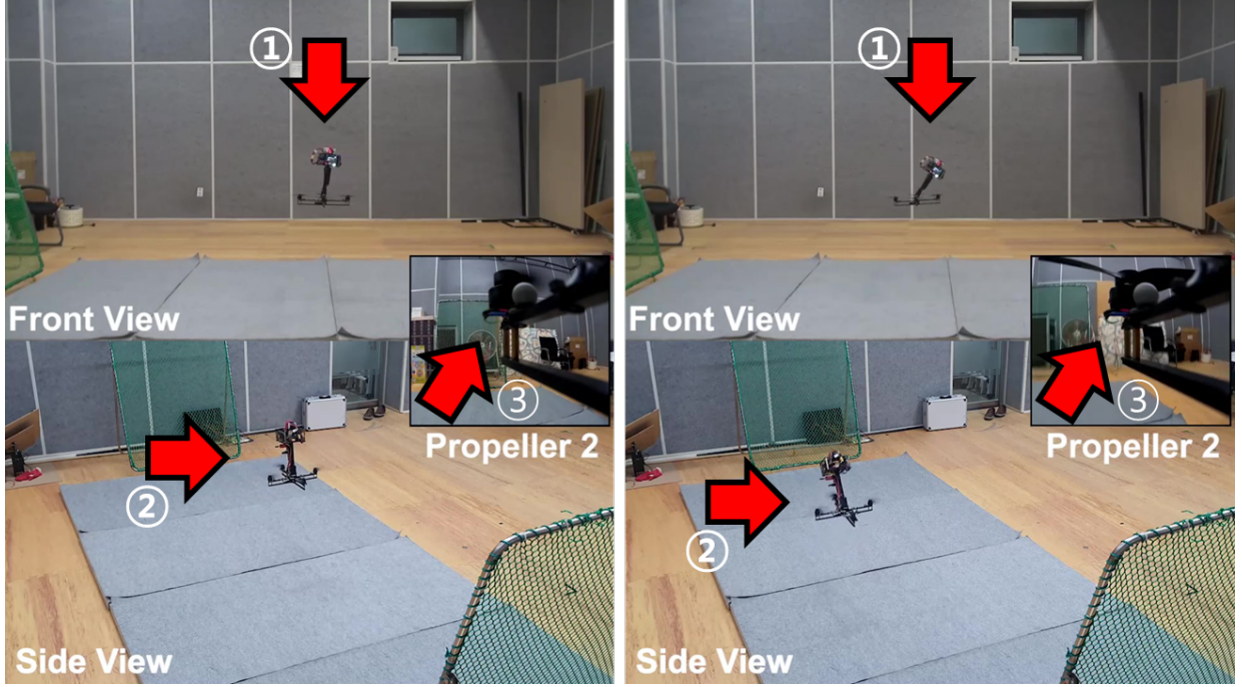
Figure 5.9: Fail-safe flight experiment with T^3-Multirotor (Top: Before failure, Bottom: After failure). ①,②: Significant change in relative attitude between TP and FP is observed when the fail-safe mode is activated, ③: Propeller 2 stopped by the operator at an arbitrary time.

the inherent characteristics of the servo-based relative attitude control system Λ_α, which has a slow response compared to the motor-based thruster.

5.5.3 Flight results

In the experiment, the motor failure is caused by the operator triggering the stop signal of Motor 2 at any time. Once the motor fails, the Faulty Motor Detector identifies the failed motor and activates the fail-safe roll control mode, whilst the pitch channel remains the conventional control mode.

Fig. 5.9 shows a fail-safe flight experiment. In the figure, we can see that the relative attitude between TP and FP changes drastically to overcome the roll-directional control failure caused by Motor 2 failure.

Fig. 5.10 shows the fail-safe flight results. The figure includes the tracking results of the TP attitude, the three-dimensional platform position, the four propeller PWM control inputs, and the relative roll attitude. From the PWM 2 command log in the Control Input graph, we can see that Motor 2 stopped rotating at about 26 seconds. After then, the faulty motor detector triggers the fail-safe roll controller to control the servo motor for restoring the disrupted roll attitude. As a result, not only the roll attitude control but also the position control was successfully restored, and the x-direction position is converged to the target position within 10 seconds after the event. Also, the average relative roll attitude remained about 0.5328 rad as predicted in the previous section.

Fig. 5.11 shows the tracking results when changing $\psi_{T,d}$, x_d and z_d values in order to validate heading, horizontal and vertical motion control performance during fail-safe flight. Experimental results show satisfactory heading and height control performance. In the x-directional position control, however, the reference trajectory tracking performance is reduced compared to other channels. However, only oscillations within a limited range are occurred and and tendency to tracking the target position is confirmed. Thus, we can conclude that the results satisfies the goal of emergency fail-safe flight.
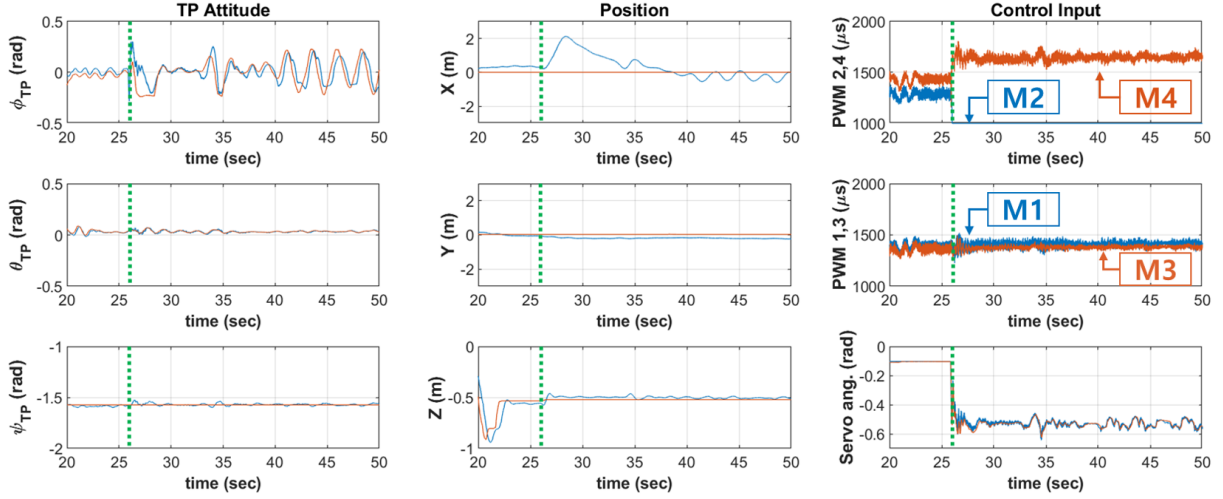
Figure 5.10: [**Fail-safe flight #1**] [Red: reference trajectory, Blue: tracking result] Attitude and position tracking results before and after motor failure. Motor failure occurred at around 26 seconds, which triggered fail-safe control mode including the servomotor-based relative attitude control.

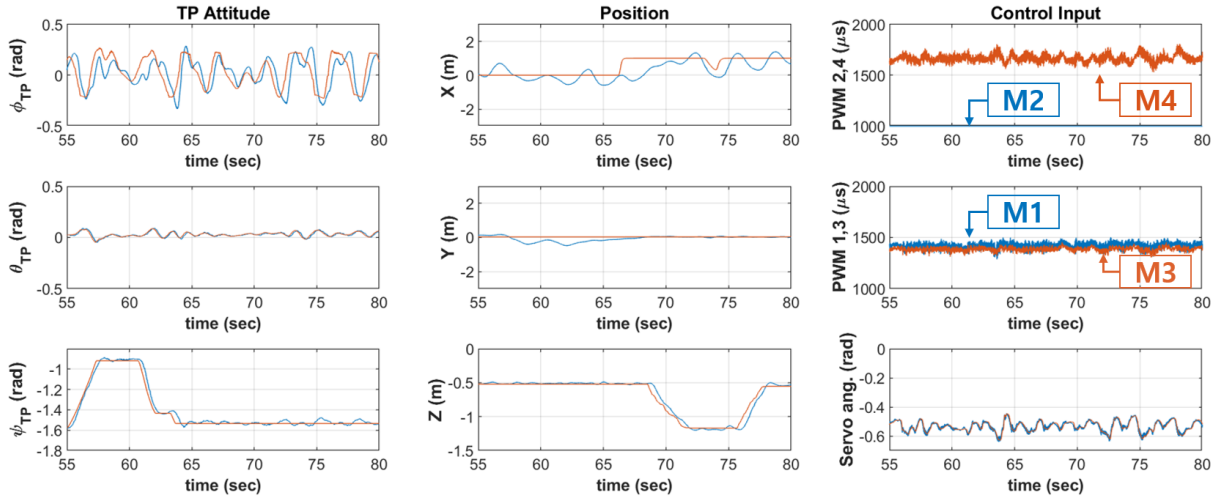Figure 5.11: [**Fail-safe flight #2**] [Red: reference trajectory, Blue: tracking result] Reference trajectory tracking results with and arbitrary ψ_T, x, and z position applied.

6

Conclusions

In this research, we introduced a robust translation control method of the multi-rotor UAV, along with the novel T^3-Multirotor flight mechanism that overcomes the underactuation characteristics of the multirotor with minimal structural deformation.

For translational motion control, we introduced 1) a new method of converting the target acceleration command to the desired attitude and total thrust, and 2) an implementation method of DOB to acceleration controller for overcoming disturbances that hinders the accurate translational motion. In the study of 1), we reflected the different dynamic characteristics between attitude and thrust for bringing more precise control better than the existing methods. To compensate for the translational force disturbance, a three-dimensional force/acceleration control technique based on the combination of thrust and attitude control of the multi-rotor is proposed. In the study of 2), we introduced the DOB-based robust control algorithm based on the nominal translational force system, which estimates and compensates the magnitude of the disturbance force applied to the fuselage. For guaranteeing the stability of the proposed controller, the Q-filter of the DOB is designed based on the μ-stability analysis. The validity of the proposed method is confirmed

through simulation and actual experiments.

For full actuation of the multirotor, the novel kinematic structure utilizing universal joint and the servomechanism is proposed to expand the degree of freedom of the multirotor. The nominal system dynamics is first derived to understand the flight characteristics of the platform. Then, a DOB-based 6-DOF motion controller is introduced, and the six controllable DOF flight of the platform is validated through both simulation and actual experiments. With multiple application examples, we demonstrated the potential of the new platform in performing flight scenarios that are not possible with conventional multirotor.

The proposed robust controller is useful in various applications such as aerial parcel delivery service or drone-based industrial operations where precise acceleration control is required. For example, in a multi-rotor-based parcel delivery service, the proposed DOB algorithm can maintain the nominal flight performance by considering the additional force due to the weight of the cargo attached to the multi-rotor as a disturbance to be estimated. Also, the proposed algorithm is suitable for situations that require precise trajectory tracking performance even in windy conditions such as maritime operations or human-rescue missions. For industrial applications involving collaborative flight of multiple multi-rotors, the proposed algorithm can be used to estimate and stabilize internal forces caused in between physically-coupled multi-rotors.

The current limitation of the T^3-Multirotor is that only the attitude of the FP within a certain range can be taken due to the inherent limitations of the universal joint mechanism. Current hardware can only take about 0.5 rad of relative attitude in each axis, and it is difficult to cope with situations where relative attitude exceeding this limitation is required. Secondly, there is a problem that excessive TP torque is often required in the process of compensating the reaction torque generated during the FP attitude control. For example, when the attitude of the FP is fixed to a specific attitude other than zero, a certain amount of RSM and PSM torque is applied to maintain the attitude. As a future work to overcome the first issue, we can think of ways to connect TP and FP in other device than a universal joint, which can be used to improve the hardware to have a wider relative attitude range.

For the second problem, we can think of a hardware modification that can make the size of r_F zero. This modification makes K of equation (4.25) zero, leaving only the servo torques and yaw torque due to universal joint as the rotational motion coupling term between TP and FP.

References

[1] S. J. Lee, D. Lee, and H. J. Kim, "Cargo transportation strategy using t 3-multirotor uav," in *2019 International Conference on Robotics and Automation (ICRA)*. IEEE, 2019, pp. 4168–4173.

[2] A. S. Brandao, F. N. Martins, and H. B. Soneguetti, "A vision-based line following strategy for an autonomous uav," in *2015 12th International Conference on Informatics in Control, Automation and Robotics (ICINCO)*, vol. 2. IEEE, 2015, pp. 314–319.

[3] R. Beard, "Quadrotor dynamics and control rev 0.1," 2008.

[4] O. Mofid and S. Mobayen, "Adaptive sliding mode control for finite-time stability of quad-rotor uavs with parametric uncertainties," *ISA transactions*, vol. 72, pp. 1–14, 2018.

[5] Z. Zuo, "Trajectory tracking control design with command-filtered compensation for a quadrotor," *IET control theory & applications*, vol. 4, no. 11, pp. 2343–2355, 2010.

[6] B. Zhao, B. Xian, Y. Zhang, and X. Zhang, "Nonlinear robust adaptive tracking control of a quadrotor uav via immersion and invariance methodology," *IEEE Transactions on Industrial Electronics*, vol. 62, no. 5, pp. 2891–2902, 2015.

[7] S. Mobayen and F. Tchier, "An lmi approach to adaptive robust tracker design for uncertain nonlinear systems with time-delays and input nonlinearities," *Nonlinear Dynamics*, vol. 85, no. 3, pp. 1965–1978, 2016.

[8] ——, "Composite nonlinear feedback integral sliding mode tracker design for uncertain switched systems with input saturation," *Communications in Nonlinear Science and Numerical Simulation*, vol. 65, pp. 173–184, 2018.

[9] K. Ohnishi, M. Shibata, and T. Murakami, "Motion control for advanced mechatronics," *IEEE/ASME transactions on mechatronics*, vol. 1, no. 1, pp. 56–67, 1996.

[10] W. Qingtong, W. Honglin, W. Qingxian, and C. Mou, "Backstepping-based attitude control for a quadrotor uav using nonlinear disturbance observer," in *34th Chinese Control Conference (CCC)*. IEEE, 2015, pp. 771–776.

[11] A. T. Salton, D. Eckhard, J. V. Flores, G. Fernandes, and G. Azevedo, "Disturbance observer and nonlinear damping control for fast tracking quadrotor vehicles," in *IEEE Conference on Control Applications (CCA)*. IEEE, 2016, pp. 705–710.

[12] T. Tomic, "Evaluation of acceleration-based disturbance observation for multicopter control," in *European Control Conference (ECC)*. IEEE, 2014, pp. 2937–2944.

[13] K. Lee, J. Back, and I. Choy, "Nonlinear disturbance observer based robust attitude tracking controller for quadrotor uavs," *International Journal of Control, Automation and Systems*, vol. 12, no. 6, pp. 1266–1275, 2014.

[14] H. Wang and M. Chen, "Trajectory tracking control for an indoor quadrotor uav based on the disturbance observer," *Transactions of the Institute of Measurement and Control*, vol. 38, no. 6, pp. 675–692, 2016.

[15] A. Aboudonia, R. Rashad, and A. El-Badawy, "Time domain disturbance observer based control of a quadrotor unmanned aerial vehicle," in *XXV International Conference on Information, Communication and Automation Technologies (ICAT)*. IEEE, 2015, pp. 1–6.

[16] P. Castaldi, N. Mimmo, R. Naldi, and L. Marconi, "Robust trajectory tracking for underactuated vtol aerial vehicles: Extended for adaptive disturbance compensation," *IFAC Proceedings Volumes*, vol. 47, no. 3, pp. 3184–3189, 2014.

[17] S. Kim, S. Choi, H. Kim, J. Shin, H. Shim, and H. J. Kim, "Robust control of an equipment-added multirotor using disturbance observer," *IEEE Transactions on Control Systems Technology*, vol. 26, no. 4, 2018.

[18] A. Chovancová, T. Fico, P. Hubinský, and F. Duchoň, "Comparison of various quaternion-based control methods applied to quadrotor with disturbance observer and position estimator," *Robotics and Autonomous Systems*, vol. 79, pp. 87–98, 2016.

[19] W. Dong, G.-Y. Gu, X. Zhu, and H. Ding, "High-performance trajectory tracking control of a quadrotor with disturbance observer," *Sensors and Actuators A: Physical*, vol. 211, pp. 67–77, 2014.

[20] S. J. Lee, S. Kim, K. H. Johansson, and H. J. Kim, "Robust acceleration control of a hexarotor uav with a disturbance observer," in *IEEE 55th Conference on Decision and Control (CDC)*. IEEE, 2016, pp. 4166–4171.

[21] D. Brescianini and R. D'Andrea, "Design, modeling and control of an omni-directional aerial vehicle," in *2016 IEEE international conference on robotics and automation (ICRA)*. IEEE, 2016, pp. 3261–3266.

[22] G. Jiang and R. Voyles, "A nonparallel hexrotor uav with faster response to disturbances for precision position keeping," in *2014 IEEE International Symposium on Safety, Security, and Rescue Robotics (2014)*. IEEE, 2014, pp. 1–5.

[23] E. Kaufman, K. Caldwell, D. Lee, and T. Lee, "Design and development of a free-floating hexrotor uav for 6-dof maneuvers," in *2014 IEEE Aerospace Conference*. IEEE, 2014, pp. 1–10.

[24] D. Langkamp, G. Roberts, A. Scillitoe, I. Lunnon, A. Llopis-Pascual, J. Zamecnik, S. Proctor, M. Rodriguez-Frias, M. Turner, A. Lanzon *et al.*, "An engineering development of a novel hexrotor vehicle for 3d applications," 2011.

[25] S. Salazar, H. Romero, R. Lozano, and P. Castillo, "Modeling and real-time stabilization of an aircraft having eight rotors," in *Unmanned Aircraft Systems*. Springer, 2008, pp. 455–470.

[26] S. Park, J. Her, J. Kim, and D. Lee, "Design, modeling and control of omni-directional aerial robot," in *2016 IEEE/RSJ International Conference on Intelligent Robots and Systems (IROS)*. IEEE, 2016, pp. 1570–1575.

[27] F. von Frankenberg, "Development of an autonomous omnicopter aerial vehicle," Ph.D. dissertation, 2016.

[28] M. Ryll, D. Bicego, and A. Franchi, "Modeling and control of fast-hex: a fully-actuated by synchronized-tilting hexarotor," in *2016 IEEE/RSJ International Conference on Intelligent Robots and Systems (IROS)*. IEEE, 2016, pp. 1689–1694.

[29] S. Rajappa, M. Ryll, H. H. Bülthoff, and A. Franchi, "Modeling, control and design optimization for a fully-actuated hexarotor aerial vehicle with tilted propellers," in *2015 IEEE International Conference on Robotics and Automation (ICRA)*. IEEE, 2015, pp. 4006–4013.

[30] M. Ryll, H. H. Bülthoff, and P. R. Giordano, "First flight tests for a quadrotor uav with tilting propellers," in *2013 IEEE International Conference on Robotics and Automation*. IEEE, 2013, pp. 295–302.

[31] M. Ryll, H. H. Bulthoff, and P. R. Giordano, "Modeling and control of a quadrotor uav with tilting propellers," in *2012 IEEE International Conference on Robotics and Automation*. IEEE, 2012, pp. 4606–4613.

[32] ——, "A novel overactuated quadrotor unmanned aerial vehicle: Modeling, control, and experimental validation," *IEEE Transactions on Control Systems Technology*, vol. 23, no. 2, pp. 540–556, 2014.

[33] D. Kastelan, M. Konz, and J. Rudolph, "Fully actuated tricopter with pilot-supporting control," *IFAC-PapersOnLine*, vol. 48, no. 9, pp. 79–84, 2015.

[34] M. K. Mohamed and A. Lanzon, "Design and control of novel tri-rotor uav," in *Proceedings of 2012 UKACC International Conference on Control.* IEEE, 2012, pp. 304–309.

[35] M. Elfeky, M. Elshafei, A.-W. A. Saif, and M. F. Al-Malki, "Quadrotor helicopter with tilting rotors: Modeling and simulation," in *2013 World Congress on Computer and Information Technology (WCCIT).* IEEE, 2013, pp. 1–5.

[36] H. Lee and H. J. Kim, "Trajectory tracking control of multirotors from modelling to experiments: A survey," *International Journal of Control, Automation and Systems*, vol. 15, no. 1, pp. 281–292, 2017.

[37] J.-H. She, M. Fang, Y. Ohyama, H. Hashimoto, and M. Wu, "Improving disturbance-rejection performance based on an equivalent-input-disturbance approach," *IEEE Transactions on Industrial Electronics*, vol. 55, no. 1, pp. 380–389, 2008.

[38] C. J. Kempf and S. Kobayashi, "Disturbance observer and feedforward design for a high-speed direct-drive positioning table," *IEEE Transactions on control systems Technology*, vol. 7, no. 5, pp. 513–526, 1999.

[39] C. Fielding, A. Varga, S. Bennani, and M. Selier, *Advanced techniques for clearance of flight control laws.* Springer Science & Business Media, 2002, vol. 283.

[40] E. Sariyildiz and K. Ohnishi, "Analysis the robustness of control systems based on disturbance observer," *International Journal of Control*, vol. 86, no. 10, pp. 1733–1743, 2013.

[41] S. Kim, J. Park, S. Kang, P. Y. Kim, and H. J. Kim, "A robust control approach for hydraulic excavators using μ-synthesis," *International Journal of Control, Automation and Systems*, vol. 16, no. 4, pp. 1615–1628, 2018.

[42] J. Doyle, "Analysis of feedback systems with structured uncertainties," in *IEE Proceedings D-Control Theory and Applications*, vol. 129, no. 6. IET, 1982, pp. 242–250.

[43] K. Zhou and J. C. Doyle, *Essentials of robust control.* Prentice hall Upper Saddle River, NJ, 1998, vol. 104.

[44] S. Skogestad and I. Postlethwaite, *Multivariable feedback control: analysis and design.* Wiley New York, 2007, vol. 2.

[45] X. Liang, Y. Fang, and N. Sun, "A hierarchical controller for quadrotor unmanned aerial vehicle transportation systems," in *2016 35th Chinese Control Conference (CCC).* IEEE, 2016, pp. 6148–6153.

[46] M. Tognon, A. Testa, E. Rossi, and A. Franchi, "Takeoff and landing on slopes via inclined hovering with a tethered aerial robot," in *2016 IEEE/RSJ International Conference on Intelligent Robots and Systems (IROS).* IEEE, 2016, pp. 1702–1707.

[47] R. Beard, "Quadrotor dynamics and control rev 0.1," 2008.

[48] H. Lee and H. J. Kim, "Trajectory tracking control of multirotors from modelling to experiments: A survey," *International Journal of Control, Automation and Systems*, vol. 15, no. 1, pp. 281–292, 2017.

[49] K. Ohnishi, M. Shibata, and T. Murakami, "Motion control for advanced mechatronics," *IEEE/ASME transactions on mechatronics*, vol. 1, no. 1, pp. 56–67, 1996.

[50] S. Kim, S. Choi, H. Kim, J. Shin, H. Shim, and H. J. Kim, "Robust control of an equipment-added multirotor using disturbance observer," *IEEE Transactions on Control Systems Technology*, vol. 26, no. 4, pp. 1524–1531, 2017.

[51] T. Tomić, "Evaluation of acceleration-based disturbance observation for multicopter control," in *2014 European Control Conference (ECC).* IEEE, 2014, pp. 2937–2944.

[52] K. Lee, J. Back, and I. Choy, "Nonlinear disturbance observer based robust attitude tracking controller for quadrotor uavs," *International Journal of Control, Automation and Systems*, vol. 12, no. 6, pp. 1266–1275, 2014.

[53] S. J. Lee, S. H. Kim, and H. J. Kim, "Robust translational force control of multi-rotor uav for precise acceleration tracking," *IEEE Transactions on Automation Science and Engineering*, 2019.

[54] A. Bacchini and E. Cestino, "Electric vtol configurations comparison," *Aerospace*, vol. 6, no. 3, p. 26, 2019.

[55] A. Freddi, A. Lanzon, and S. Longhi, "A feedback linearization approach to fault tolerance in quadrotor vehicles," *IFAC proceedings volumes*, vol. 44, no. 1, pp. 5413–5418, 2011.

[56] G. P. Falconí, J. Angelov, and F. Holzapfel, "Hexacopter outdoor flight test results using adaptive control allocation subject to an unknown complete loss of one propeller," in *2016 3rd Conference on Control and Fault-Tolerant Systems (SysTol)*. IEEE, 2016, pp. 373–380.

[57] G. Michieletto, M. Ryll, and A. Franchi, "Control of statically hoverable multi-rotor aerial vehicles and application to rotor-failure robustness for hexarotors," in *2017 IEEE International Conference on Robotics and Automation (ICRA)*. IEEE, 2017, pp. 2747–2752.

[58] A.-R. Merheb, H. Noura, and F. Bateman, "Emergency control of ar drone quadrotor uav suffering a total loss of one rotor," *IEEE/ASME Transactions on Mechatronics*, vol. 22, no. 2, pp. 961–971, 2017.

[59] A. Nemati, R. Kumar, and M. Kumar, "Stability and control of tilting-rotor quadcopter in case of a propeller failure," in *Proceedings of the ASME Dynamic Systems and Control Division*, 2016.

[60] S. J. Lee, J. Yoo, and H. J. Kim, "Design, modeling and control of t3-multirotor: A tilting thruster type multirotor," in *2018 IEEE International Conference on Robotics and Automation (ICRA)*. IEEE, 2018, pp. 1214–1219.

[61] W. Dong, G.-Y. Gu, X. Zhu, and H. Ding, "High-performance trajectory tracking control of a quadrotor with disturbance observer," *Sensors and Actuators A: Physical*, vol. 211, pp. 67–77, 2014.

[62] S. J. Lee, S. H. Kim, and H. J. Kim, "Robust translational force control of multi-rotor uav for precise acceleration tracking," *IEEE Transactions on Automation Science and Engineering*, 2019.

국 문 초 록

오늘날 멀티로터 무인항공기는 단순한 비행 및 공중 영상 촬영용 장비의 개념을 넘어 비행 매니퓰레이션, 공중 화물 운송 및 공중 센싱 등의 다양한 임무에 활용되고 있다. 이러한 추세에 맞추어 로보틱스 분야에서 멀티로터 무인항공기는 부과된 임무에 맞추어 원하는 장비 및 센서를 자유로이 탑재하고 비행할 수 있는 다목적 공중 로봇 플랫폼으로 인식되고 있다.

그러나 현재의 멀티로터 플랫폼은 돌풍 등의 외란에 다소 강건하지 못한 제어성능을 보인다. 또한, 병진운동의 제어를 위해 비행 중 지속적으로 동체의 자세를 변경해야 해 센서 등 동체에 부착된 탑재물의 자세 또한 지속적으로 변화한다는 단점을 가지고 있다. 위의 두 가지 문제들을 해결하고자 본 연구에서는 외란에 강건한 멀티로터 제어기법과, 병진운동과 자세운동을 독립적으로 제어할 수 있는 새로운 형태의 완전구동 멀티로터 비행 매커니즘을 소개한다.

강건 제어기법의 경우, 먼저 정확한 병진운동 제어를 위한 병진 힘 생성 기법을 소개하고 뒤이어 병진 힘 외란에 강건한 제어를 위한 외란관측기 기반 강건 제어 알고리즘의 설계 방안을 논의한다. 제어기의 피드백 루프 안정성은 μ 안정성 분석 기법을 통해 검증되며, μ 안정성 분석이 가지는 엄밀한 안정성 분석의 결과를 검증하기 위해 스몰게인 이론 (Small Gain Theorem) 기반의 안정성 분석 결과가 동시에 제시 및 비교된다. 최종적으로, 개발된 제어기를 도입한 멀티로터의 3차원 병진 가속도 제어 성능 및 힘 벡터의 형태로 인가되는 병진 운동 외란에 대한 극복 성능을 실험을 통해 검증하여, 제안된 제어기법의 효과적인 비행 지점 및 궤적 추종 능력을 확인한다.

완전 구동 멀티로터의 경우, 기존의 완전구동 멀티로터가 가진 과도한 중량 증가 및 저조한 에너지 효율을 극복하기 위한 새로운 매커니즘을 소개한다. 새로운 매커니즘은 기존 멀티로터와 최대한 유사한 형태를 가지되 완전구동을 위해 오직 두 개의 서보모터만을 포함하며, 이로 인해 기존 멀티로터와 비교해 최소한의 형태의 변형만을 가지도록 설계된다. 새로운 플랫폼의 동적 특성에 대한 분석과 함께 유도된 운동방정식을 기반으로 한 6자유도 비행 제어기법이 소개되며, 최종적으로 다양한 실험과 그 결과들을 통해 플랫폼의 완전구동

비행 능력을 검증한다.

추가적으로 본 논문에서는 완전구동 멀티로터가 가지는 여분의 제어입력(redundancy)를 활용한 쿼드콥터의 단일모터 고장 대비 비상 비행 기법을 소개한다. 비상 비행 전략에 대한 자세한 소개 및 실현 방법, 비상 비행 시의 동역학적 특성에 대한 분석 결과가 소개되며, 실험결과를 통해 제안된 기법의 타당성을 검증한다.